Alma Mater Studiorum - Università di Bologna

DOTTORATO DI RICERCA IN

INGEGNERIA BIOMEDICA, ELETTRICA E DEI SISTEMI

Ciclo 33

Settore Concorsuale: 09/G2 - BIOINGEGNERIA

Settore Scientifico Disciplinare: ING-INF/06 - BIOINGEGNERIA ELETTRONICA E INFORMATICA

DEVELOPMENT OF A PATIENT-SPECIFIC MODEL FOR STROKE RISK ASSESSMENT IN ATRIAL FIBRILLATION PATIENTS

Presentata da: Alessandro Masci

Coordinatore Dottorato

Michele Monaci

Supervisore

Cristiana Corsi

Co-supervisore

Stefano Severi

Esame finale anno 2021

Ai miei Genitori

Contents

List of Figures

List of Tables

Abstract

Atrial fibrillation is associated with a five-fold increase in the risk of cerebrovascular events, being responsible of 15-18% of all strokes. The morphological and functional remodelling of the left atrium caused by atrial fibrillation favours blood stasis and, consequently, stroke risk. In this context, several clinical studies suggest that stroke risk stratification could be improved by using haemodynamic information on the left atrium (LA) and the left atrial appendage (LAA). The goal of this study was to develop a personalized computational fluid dynamics (CFD) model of the left atrium which could clarify the haemodynamic implications of atrial fibrillation on a patient-specific basis. The developed CFD model was first applied to better understand the role of LAA in stroke risk. In fact, the interplay of the LAA geometric parameters such as LAA length, tortuosity, surface area and volume with the fluid dynamics parameters and the effects of the LAA closure have not been investigated. This analysis might highlight new insights into the effects of atrial fibrillation on the LAA haemodynamics, thus providing a better understanding of the thrombi formation risk.
The developed CFD model was then applied in several clinical scenarios with the aim to predict the stroke risk stratification for a patient affected by AF in order to potentially provide a complete tool for helping the physicians in the clinical practice.
Results demonstrated the capabilities of the CFD model to reproduce the real physiological behaviour of the blood flow dynamics inside the LA and the LAA. In fact, as expected, the velocities within the LA and LAA showed higher values in the control group patients with respect to the paroxysmal and persistent AF patients. Moreover, the lowest values within the LA and LAA were observed in the persistent AF group that could imply a higher probability of blood stasis and consequently an increase of the stroke risk. In the paroxysmal AF group we observed values that represented an average situation between the control and persistent AF group. Finally, we determined that the fluid-dynamics parameters enhanced in this research project could be used as new quantitative indexes to describe the different types of

AF and open new scenarios for the patient-specific stroke risk stratification.

Keywords: atrial fibrillation, left atrial appendage, stroke, risk stratification, patient specific, computational fluid dynamics.

Introduction

Atrial Fibrillation (AF) is the most common form of arrhythmia worldwide. It has been estimated that the prevalence of AF in US is about 2.2 million including paroxysmal or persistent AF [5]. AF is a supraventricular arrhythmia characterized by chaotic and uncoordinated atrial activation and contraction [6]. This arrhythmia remains one of the major causes of stroke, heart failure, sudden death, and cardiovascular morbidity in the world. AF represents a major clinical, social and economical burden; moreover, the number of patients affected by this pathology will increase even more in the future [7]. Indeed by 2030, 14–17 million AF patients are anticipated in the European Union, with 120000–215000 newly diagnosed patients per year [8, 9]. A recent prospective study from the Netherlands, based on a cohort of subjects older than 55 years of age, has highlighted a total prevalence of AF of 5.5 %, increasing from 0.7 % in subjects from 55-59 years to 17.8 % in 85 year old patients (see Figure 1) [1].

Regarding the consequences of AF it is known that this pathology is an independent risk factor for stroke. It is associated with a fivefold increased

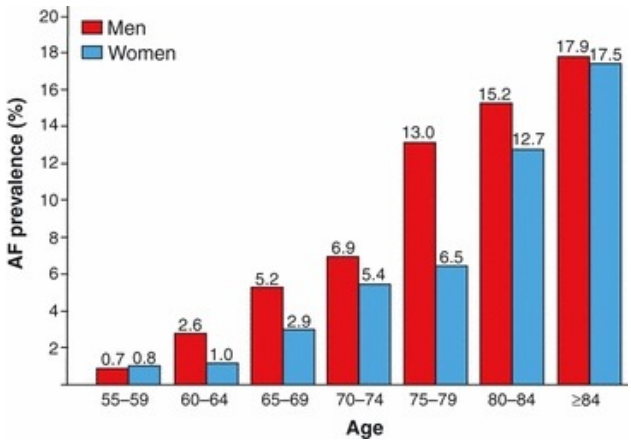

Figure 1: Prevalence of atrial fibrillation in the Rotterdam Study [1].

risk of cerebrovascular events [10, 11], being responsible of 15-18 % of all strokes. Indexes routinely used in clinical practice to stratisfy stroke risk, such us the CHA_2DS_2-VASc score [7], are based on empirical information without considering specific hemodynamic implications of AF which might improve the predictive power of such scores [12]. AF leads to left atrium (LA) structural remodeling, which consists in a progressive LA enlargement [13] and in left atrium appendage (LAA) elongation [3] and, consequently, to an alteration of the mechanical function, which causes a chaotic and strongly reduced contractile activity of LA cells. These changes could modify the physiological haemodynamics within the LA fostering blood stasis, clot formation and embolism. Moreover, because of its hooked morphology, the LAA is the left atrial site of the highest blood stasis risk, increasing the incidence of thrombus formation and stroke. In fact, 90 % of the intracardiac thrombi in patients with cardioembolic stroke/transient ischemic attack (TIA) are considered as originating in the LAA [14]. Oral anticoagulation therapy was the only option available until recently. However, it increases bleeding risk and interpheres with other drugs and multiorgan functioning, and its risk can overtake the otherwise remakable benefits on thromboembolic events [15].
For these reasons, different strategies have been developed such as the use of interventional treatments, i.e. LAA percutaneous closure, which seems to better reduce the risk of thromboembolism compared to warfarin anticoagulation therapy [16]. These treatments are restricted to small subgroups of patients, due to the procedural risks and costs which may overcome the preventive antiembolic efficacy.
Computational fluid dynamics (CFD) represents a valuable non-invasive approach to determine and assess physically meaningful parameters and indicators in a complex fluid dynamics system, such as the cardiac blood flowrates, vorticity, turbulent kinetic energy, etc. CFD modeling of the LA and LAA in AF has not been faced exaustively considering the relevance of the potential clinical impact. Most of the modeling studies are focused on ventricular fluid-dynamics [17, 18]. The first model developed for the LA, was proposed by Zhang and coll. [19]. No patient-specific information related to chamber morphology and motion was included in the model. Koizumi et al. [20] used a real LA geometry from a healthy volunteer; the LA motion model was defined considering the location of the mitral valve (MV) annulus in the magnetic resonnace images and some reference anatomical points manually extracted on the left side of the mitral annulus. This approach implies a simplification when the motion of the LA wall is considered. In addition, boundary conditions were defined considering fixed pressure values taken from literature. In [21], Garcia and coll. evaluated stroke risk associated to four different LA/LAA morphologies by the CFD simulations and derived

haemodynamics parameters. Yet, the simulations considered a fixed geometry and therefore could not account for the effect of wall motion on blood dynamics. Otani and coll. [22] presented the first framework for personalized blood flow analysis in the LA based on computed tomography (CT) imaging. The proposed model also included the left ventricle during ventricular diastole and the pulmonary veins (PVs) were modeled as cylinders. Moreover, morphological and quantitative features of LAA have been increasingly studied in the past few years [3, 23]. Despite these attempts, the association between the aforementioned LAA anatomical features and stroke risk does not seem straightforward, and conflicting results have been published. Moreover, it is still uncertain what is the best strategy for stroke prevention in AF.
To the best of our knowledge, the interplay of the geometric parameters such as LAA length, tortuosity, surface area and volume with the fluid dynamics parameters have not been investigated.
Therefore, the aim of the study presented in this thesis was the development of a patient-specific CFD model of the left atrium in AF which elucidated the role of the key anatomical and functional features of AF. The provided tool might be used for enabling personalized stroke risk stratification and therapy planning. The blood flow model developed in this thesis consisted of a fluid governed by the incompressible Navier-Stokes equations. A crucial aspect was the choice of the reference frame where we define the PDEs, as the left atrium (whose volume stands for the computational domain) deforms along the heartbeat. To take into account the motion of the fluid domain, we adopted the so-called Arbitrary Lagrangian Eulerian (ALE) reference frame. In this thesis we show how the patient-specific CFD model can be used in several applications with the aim to try to predict the stroke risk stratification for a patient affected by AF in order to potentially provide a complete tool for helping the physicians in the clinical practice. Indeed, we employed the developed CFD model in real clinical scenarios in order to enhance the differences in the haemodynamics pattern between the simulated conditions. Moreover, we focused on the LAA, given its criticity in the stroke risk assessment in order to provide significant results and new insights into the effects of the AF on the LAA fluid-dynamics, thus providing a better understanding of the thrombi formation risk.
This thesis is organized as follows:

- **Chapter 1**: we introduce the main theoretical concepts that help to contextualize the aim of the thesis. In particular, we discuss the anatomy of the left atrium and the left atrial appendage. Then, we focus on the description of atrial fibrillation. Finally, we present the

workflow of the study we designed and implemented.

- **Chapter 2**: we describe in detail the computational fluid dynamics model developed for the CFD simulation of AF patients. Moreover, we also focus on the comparison between different LA motion models to simulate the AF condition with the CFD model.

- **Chapter 3**: in this chapter we focus on the design and development of a workflow to quantify the influence of LAA morphology on the LA hemodynamics. This analysis can highlight new insights into the effects of atrial fibrillation on the LAA haemodynamics, thus providing a better understanding of the thrombi formation risk. Moreover, we discuss also the LA haemodynamics changes caused by the simulation of the two different LAA occlusor devices implantations with the use of the CFD model.

- **Chapter 4**: we test and validate the CFD model designed and developed in this thesis on different clinical scenarios. Indeed, we computed the haemodynamics parameters in patients with and without the AF and in patients with different pathophysiological conditions in order to enhance the differences in the fluid-dynamics indexes evaluated from the simulations. Moreover, we tried to find the most important parameters from the CFD model that can potentially stratify the stroke risk on a patient-specific basis.

- Conclusions and future developments follow.

Chapter 1

Anatomy of the Left Atrium and Atrial Fibrillation

In this Chapter, we briefly introduce the main concepts required to understand the scenario in which this thesis was developed. We start from the anatomy of the left atrium and in particular of the left atrial appendage (Section 1.1 and 1.1.1, respectively). Then, we describe one of the most important alterations of the electrical activity of the heart: the atrial fibrillation (Section 1.2). Finally, in Section 1.3 we describe the scope of the study presented in this work.

1.1 Anatomy of the left atrium

In this section, we describe in details the anatomy of the left atrium (LA), focusing also on the left atrial appendage (LAA).

The left atrium has a distinctive appendage that is a finger-like pouch extending from the main body of the atrium (see Figure 1.1). The main body comprises the pulmonary venous (PV) portion (the PVs are usually four), the septal portion, and the vestibule, which is the outlet part of the atrial chamber that surrounds the mitral orifice. The left atrial appendage has a fairly-well defined opening (the ostium of appendage), however the other components do not have anatomic demarcations.

Viewed from the frontal aspects of the chest, we notice that the left atrium is the most posteriorly situated of the four cardiac chambers and it is supe-

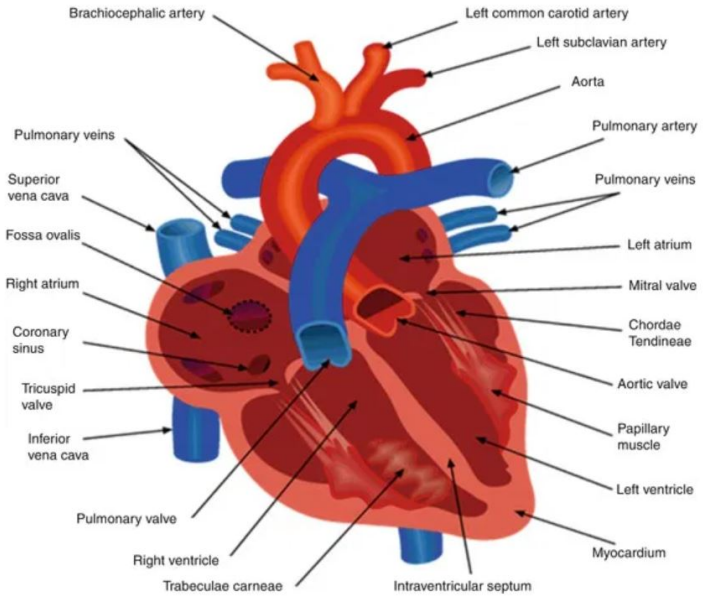

Figure 1.1: Basic anatomy of the heart. In particular the anatomical details of the Left Atrium are shown [2].

riorly situated with respect to the right atrial chamber. The four pulmonary veins enter the posterior part of the left atrium and the left veins are located more superior than the right ones. Moreover, the tracheal bifurcation, the esophagus and descending thoracic aorta are located immediately behind the pericardium overlying the posterior wall of the left atrium. If we follow the blood direction, we observe that the LA starts at the pulmonary veno-atrial junctions and terminates at the fibro-fatty tissue plane that marks the atrioventricular junction at the mitral orifice. The left atrium is relatively smooth-walled on its internal part (see Figure 1.2), however its wall thickness is not uniform. For example, it is possible to evaluate that the thickness of its muscle component measured transmurally is in mean 4.5 mm and the thickness of the lateral wall is about 4 mm. However, the anterior wall thickness, related to the aortic root, is about 3.2 mm and become very thin at the area near the vestibule of the mitral annulus (see Figure 1.2). The posterior wall of the LA is closed to the esophagus and its nerves, the thoracic aorta and the coronary sinus. In this part, the thickness is about 4.1 mm and it becomes thinner in proximity of the orifices of the left and right pulmonary veins [2].
Regarding the pulmonary veins, Yen Ho et al. [24] presented an anatomical study on a series of 35 heart specimens and found that the 74 % had the classical arrangement of four orifices, 17 % with five orifices and the remaining

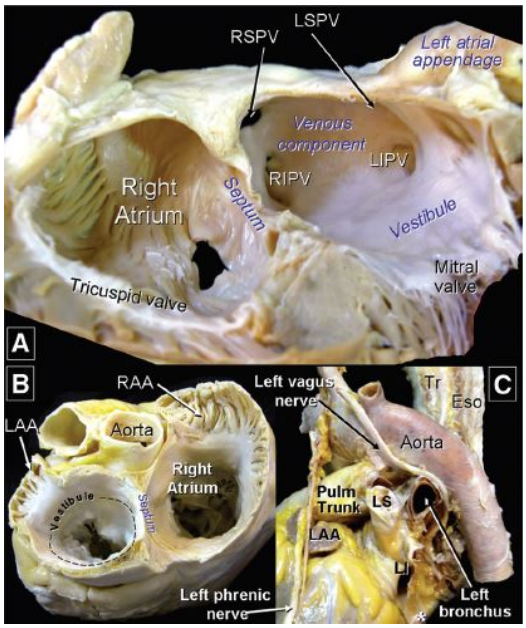

Figure 1.2: Anatomy of the left atrium. In picture, we find a dissection of the LA from a left-anterior perspective to show its components and the endocardial surface. Picture B is a view from back and enhances the relationship of the aortic root with the LA, including the atrial septum. Finally, picture C is the left atrial view in order to show the posterior location of the left atrium and its relationship with cardiac and extracardiac structures. Notice that RAA is the right left atrial appendage, Tr is the trachea, LS and LI indicates the left superior and the left inferior pulmonary veins, respectively [2].

9 % had a common vein on the left or right side. This study demonstrates the high variability of the number of pulmonary veins between patients.
Describing the classical pattern, we observe that the right superior PV passes behind the junction between the superior cava vein and the right atrium, whereas the inferior PV passes behind the intercaval area (see Figure 1.2).
The orifices of the right pulmonary veins are directly adjacent to the plane of the atrial septum. In addition, there is a ridge-like structure between the entrance of the left superior pulmonary vein and the ostium of the left atrial appendage (see Figure 1.2). Moreover, muscle sleeves extend from the left atrium to surround the external aspects of the venous walls.
Altough the electric activity in this region is well known, today this is matter of discussion between cardiac electro-physiologists, because they could be associated with focal activity initiating cardiac arrhythmias [25].
The muscle sleeves are thickest at the veno-atrial junction and then fade away towards the lungs. Regarding the veno-atrial junction, the structural

border between veins and atrium is indistinct. The endocardium of the left atrium continues into the endothelium of the vein: the media of PV contains smooth muscle cells in a matrix of fibrous and elastic tissues and the transition from the venous media to the subendocardial region of the left atrium is represented by a gradual decline of smooth muscle cells.
Other structures of interest in the left atrium are represented by the presence of direct connections between superior and inferior venous sleeves. Moreover, it is interesting to notice that there are multiple muscular bridges between the atrial chambers. These bridges have varying widths and thicknesses. However, muscular bridges between veins and atrial walls are not common. One of the most important bridge, that represents the prevalent interatrial conduction pathway for the propagation of the sinus impulse to the anterior left atrial wall, is the Bachmann bundle, known also as the interauricular band.

1.1.1 The left atrial appendage

The left atrial appendage (LAA) is a long, hook-like true diverticulum of the left atrium [26]. The LAA lies anteriorly in the atrioventricular sulcus in close proximity to the left phrenic nerve and the left pulmonary veins. While the body of the LA is a smooth-walled structure, parallel-running pectinate muscles are contained within the tubular LAA. The LAA lies within the pericardium, next to the superior lateral side of the main pulmonary artery, and superior to the left ventricular free wall. It is often multilobed.
The LAA shape is variable and it is possible to classify it, based on its morphology, as follows:

1. **cactus** LAA (first row Figure 1.3): it is characterized by the presence of a dominant central lobe with secondary lobes extending from the central one in both the superior and inferior directions;

2. **chicken wing** LAA (second row Figure 1.3): it shows an obvious bend in proximal or middle part of the dominant lobe, or folding back on itself at a certain distance from the LAA ostium;

3. **windsock** LAA, (third row Figure 1.3): it has one dominant lobe of sufficient length and this constitutes the primary structure. Moreover, this type of LAA shows variation in the location and number of secondary or also tertiary lobes arising from the dominant lobe;

4. **cauliflower** LAA (fourth row Figure 1.3): it presents the most complex internal characteristics. This LAA type shows variations that consist

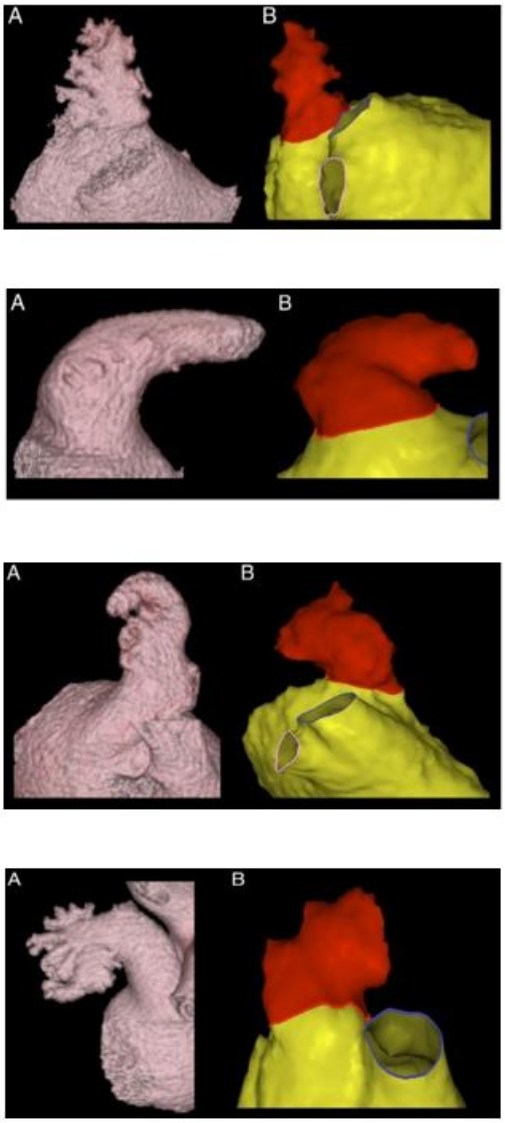

Figure 1.3: LAA morphology types: first row refers to the LAA cactus type, second row to the LAA chicken type, third row to the LAA windsock type, fourth row to the LAA cauliflower type. CT (A) and magnetic resonance (B) image reconstruction [3].

in a more irregular shape of the LAA ostium (oval instead of round) and a variable number of lobes with lack of a dominant lobe.

In the study of Di Biase et al. [3], 932 patients were analyzed and the prevalence of cactus, chicken wing, windsock and cauliflower types was 30 %,

48 %, 19 % and 3 % respectively: this data indicates that the most typical LAA type is the chicken wing one.

Due to its particular anatomy, the left atrial appendage represents one of the major sources of cardiac thrombus formation responsible for transient ischemic attack (TIA)/stroke in patients in atrial fibrillation (see Section 1.2). For this reason, the characteristics of the LAA are very important because it is possible to correlate them to the risk of thrombus formation. To this aim, it seems that patients with non-chicken wing LAA morphology are significantly more likely to have an embolic event [3]. If these results are confirmed, they may be determinant for the choice of the anticoagulant therapy in patients with atrial fibrillation. To sum up, the state-of-the-art knowledge states the morphology of the LAA should be taken into account in order to study its correlation with the risk of stroke in patients with AF.

1.2 Atrial fibrillation

Atrial fibrillation (AF) is a supraventricular arrhythmia characterized by chaotic and uncoordinated atrial activation and contraction [6]. This arrhythmia remains one of the major causes of stroke, heart failure, sudden death, and cardiovascular morbidity in the world. AF represents a major clinical, social and economical burden; moreover, the number of patients affected by this pathology will increase even more in the future [7]. Indeed by 2030, 14–17 million AF patients are anticipated in the European Union, with 120000–215000 newly diagnosed patients per year [8, 9]. Estimates suggest an AF prevalence of approximately 3% in adults aged 20 years or older [8, 9], with greater prevalence in older persons and in patients with conditions such as hypertension, heart failure, coronary artery disease (CAD), valvular heart disease, obesity, diabetes mellitus, or chronic kidney disease (CKD). The direct costs of AF already amount to approximately 1 % of total healthcare spending in the UK, and between 6.0–26.0 billion US dollars in the US for 2008 [27], driven by AF-related complications (e.g. stroke) and treatment costs (e.g. hospitalizations). These costs will increase dramatically unless AF is prevented and treated in a timely and effective manner.
Atrial fibrillation has several heterogeneous clinical presentations and this heterogeneity of its pathophysiology, its different symptomatic impact on each patient and the possibility of different therapeutical options represent a challenge between physicians and for the national health system. In fact, atrial fibrillation has a complex and not completely understood pathophysi-

ology. The presence of genetic predisposition, structural changes and fibrosis, inflammation, dysfunction coupled with electrophysiological abnormalities of the atria, and PV sleeves may contribute to initiation and maintenance of the fibrillatory process. With the help of the experimental studies and the computational models, it seems that AF drivers are identified in stable or unstable reentrant circuits with short cycle length in or near the PVs, while the other atrial parts follow passively these impulses with fibrillatory conduction. The average size of reentry pathway during AF is dependent on atrial wavelength. To this aim, this quantity is defined by the product of conduction velocity and refractory period, that is the time span at which the atrial tissue is not excitable [28]. Short wavelengths implicate larger number of smaller circuits which could have implications for arrhythmia susceptibility and stability, while long wavelengths are associated with larger and fewer wavefronts. Several human studies, accompanied by AF models, are developed in order to assess structural, functional and electrophysiological requirements for AF induction and sustenance [29]. It was found a significant effective refractory period (ERP) shortening (up to 20 %) in pacing induced AF after 2 minutes. This ERP shortening was an essential feature in AF and it is further supported by several studies [30, 31]. Moreover, the atrial size increase, due to AF, is likely to promote the generation of multiple reentrant wavelets, by decreasing the atrial wavelength of reentry.
In addition, the study of Jeong et al. [23] analyzes LAA volume in patients with and without AF. The results show a larger LAA volume in patients with AF compared to patients without AF. Also, the LAA orifice diameter is increased in AF patients with respect to patients without AF. Moreover, these results suggest that a larger LAA orifice is closely related with blood stasis in LAA as well as with stroke risk. It is observed that atrial fibrillation may enlarge the LAA size that leads to slower LAA flow velocity/ blood stasis. The results obtained by Jeong et al. are also confirmed by a study in postmortem explanted hearts [32]. It is noticed that the left atrial appendage volume from patients with atrial fibrillation is 3 times the volume of those in sinus rhythm. This study also reported that the endocardial surface is smoother and related with more extensive endocardial fibroelastosis and these characteristics might favorite the thrombus formation [24].

Several theories have been formulated to explain AF perpetuation, and imply the existence of:

1. **Multiple-circuit reentry**: this hypothesis affirms that AF is maintained by multiple wavelets varying continuously in location and time within the atria (Figure 1.4): they can clash with each other and then disappear, or they can split into smaller wavelets which re-excite the

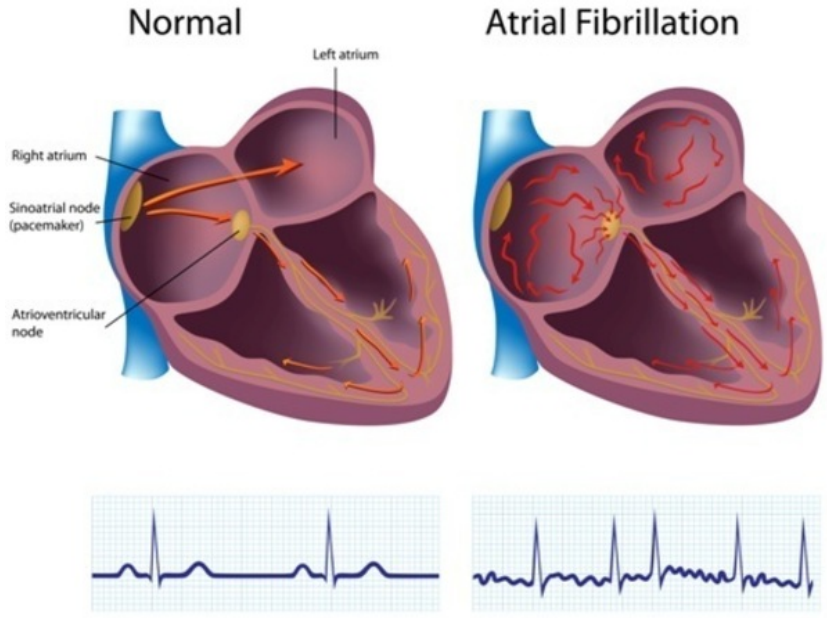

Figure 1.4: Mechanism of atrial fibrillation based on the theory of multiple-circuit reentry [4].

atria again. This reentry persistence could be possible if the heads of propagating wavefronts encounter excitable tissue. For this reason, an increased atrial size, the shortening of refractory period, the presence of anatomical obstacles allow for smaller and more atrial reentry circuits to coexist and develop. At this point, it is intuitive to affirm that the heterogeneity of the action potential promotes multiple wavelets generation. If the number of wavelets in the heart is higher at any moment, the arrhythmia will persist: if atria cannot work as a functional syncytium, the obvious consequence is a fibrillatory response. Moe proposed this theory for the first time in 1962 [4]. Later, AF activation mapping has reinforced the knowledge about the initiation and maintenance of the arrhythmia.

2. **Single circuit reentry**: To integrate the theory proposed by Moe, thanks to further AF activation mapping studies, it was shown that even a single re-entrant wavefront can produce AF [33]. The single-circuit reentry model was based on the existence of a single stable source (mother circuit), acting as a periodic background focus. A perfect substrate for auto-sustained circuits movement reentry, breaking the wavefront into multiple wavelets, is provided by the complex three-

dimensional structure of the atrium, with its network of pectinate muscles.

3. **Rapid ectopic activity**: A further study performed by Haissaguerre and colleagues [25] has demonstrated that AF is often triggered by ectopic activity arising from the pulmonary vein region. When an ectopic beat encounters a refractory zone, it can propagate through the faster recovering tissue in another direction, causing the generation of abnormal "re-entrant rotors". It is important to remember that when electrical impulses spread rapidly, atrial tissue responds producing, as expected, a regular tachycardia, up to a certain threshold rate. Beyond this critical point, a fibrillatory response will occur.

At this point, it is important to classify the different types of atrial fibrillation: today, there is no common agreement on AF classification, altough several schemes have been proposed. The most common classifications are based on the electrocardiographic onset or on endocardial electrograms obtained with different mapping systems. Gallagher and Camn [34] divided AF into:

1. paroxysmal AF: atrial fibrillation with spontaneous interruption generally within 7 days or in 24-48 h,

2. persistent AF: atrial fibrillation that, independently of its duration, does not interrupt spontaneously but with therapeutical interventions (pharmacological or electrical),

3. permanent AF: atrial fibrillation in which interruption attempts have not been made or they were not successful. This leads to failed restoration of sinus rhythm. For example, the cardioversion attempts were not effective.

About the multiple consequences of atrial fibrillation, the most threatening one is the increase of the stroke risk. In fact, several AF features concomitate to increase this serious condition. The first one is **anatomical remodeling**, which consists in the progressive enlargement of the left atrium (LA) and in the elongation of the left atrial appendage (LAA), due to the lack of contractility and increased compliance caused by this condition. Moreover, it is observed that the area between the superior pulmonary veins is the thinnest, 2.3 mm, with no great difference between patients with and without atrial fibrillation, whereas the wall is thinner in the middle and between the inferior venous orifices in those with atrial fibrillation [35]. In fact, a second factor is the **loss of mechanical function**, not only during the

AF episodes, but also in sinus rhythm. This effect determines a progressive decrease in ejection fraction [13]. All these factors favor blood stagnation in the LA and the LAA thereby increasing the risk of thromboembolism. The thrombotic material associated with AF arises most frequently in the LAA: in particular, thrombi are often encountered in AF patients with ischemic stroke than in those without stroke [36]. Moreover, it seems that LAA flow velocity is lower in AF and it is probably related to the loss of mechanical contraction. Finally, a further consequence of the atrial fibrillation is its influence on the coronary blood flow. This is lower during AF than during regular atrial pacing in patients with angiographically normal condition arteries. This reduced coronary flow reserve may be particularly important in patients with coronary heart diseases, in which compensatory coronary vasodilation is limited [37].
In summary, we see that complex consequences occur in atrial fibrillation. Finally, focusing on the clinical practice, the risk stratification scheme most commonly used is the Cardiac failure, Hypertension, Age, Diabetes, Stroke [Doubled] (CHADS2) score, in which 2 points are assigned for a history of stroke or transient ischemic attack and 1 point each is assigned for age more than 75 years, a history of hypertension, diabetes, or recent clinical heart failure or impaired left ventricular systolic function (generally interpreted as an ejection fraction 35%). The CHADS2 score was derived from amalgamation of the (now historical) Atrial Fibrillation Investigators and Stroke Prevention in Atrial Fibrillation Investigators schema initially validated in a retrospective cohort of hospitalized patients with atrial fibrillation, in which a score of 0 identified patients at low stroke risk, a score of 1 to 2 identified patients at moderate stroke risk, and a score greater than 2 identified patients at high stroke risk [38]. After validation in other cohorts, the CHADS2 scoring method gained popularity because of its simplicity and endorsement in several widely promulgated practice guidelines, including those developed by the European Society of Cardiology [6]. However, some of the risk factors fundamental to the CHADS2 score are difficult to evaluate in individual patients. The criteria for a diagnosis of heart failure, for example, are not clearly defined, and clinical assessment of this condition may be inaccurate. Indeed, this score is based on generic empirical factors and as a result, its predictive power remains low [12].

1.3 Aim of the project

The aim of the study presented in this thesis is the development of a patient-specific Computational Fluid Dynamics (CFD) model of the left atrium in atrial fibrillation as a tool to help elucidating the role of the key anatomical and functional features of AF in the LA blood flow. CFD represents a valuable non-invasive approach to determine and assess physically meaningful parameters and indicators in a complex fluid dynamics system, such as the cardiac blood flowrates, vorticity, turbulent kinetic energy, etc. CFD modeling of the LA in AF has not been faced exaustively considering the relevance of the potential clinical impact. Most of the modeling studies are focused on ventricular fluid-dynamics [17, 18]. The first model developed for the LA, was proposed by Zhang and coll. [19]. No patient-specific information related to chamber morphology and motion was included in the model. Koizumi et al. [20] used a real LA geometry from a healthy volunteer; the LA motion model was defined considering the location of the mitral valve (MV) annulus in the magnetic resonnace images and some reference anatomical points manually extracted on the left side of the mitral annulus. This approach implies a simplification when the motion of the LA wall is considered. More in detail, LA movement of the lower part of the LA wall was computed with the assumption of a simple compression/extension in one direction and linearly increasing the compression rate towards the MV on the other direction; the movement of the upper part of the LA was fixed. In addition, boundary conditions were defined considering fixed pressure values taken from literature. In [21], Garcia and coll. evaluated stroke risk associated to four different LA/LAA morphologies by the CFD simulations and derived haemodynamics parameters. Yet, the simulations considered a fixed geometry and therefore could not account for the effect of wall motion on blood dynamics. Otani and coll. [22] presented the first framework for personalized blood flow analysis in the LA based on computed tomography (CT) imaging. The proposed model also included the left ventricle during ventricular diastole and the pulmonary veins (PVs) were modeled as cylinders. With respect to the studies found in literature, the project presented in this thesis presents several elements of the originality:

- LA anatomy is obtained from AF patients. In particular, they were affected by paroxysmal or persistent atrial fibrillation and it was already planned for them a procedure of Radio Frequency Ablation (RFA), in which parts of the electrical conduction system of the heart are ablated, using the heat generated from medium frequency alternating current (in the range of 350-500 kHz);

- the displacement field of the LA is extracted from real clinical data, in order to define its deformation history along the heartbeat (motion model);

- realistic inflow boundary conditions are obtained by real Doppler measurements in AF patient, if available.

The importance of a 3D model of the left atrium for each specific patient is related to the following reasons:

1. LA anatomy differs in several parts for each patient: for example one of the most interesting features of the LA is the number of the pulmonary veins: as seen in Section 1.2, usually the PVs are four, however there is a high variability between patients. Moreover, the position of their orifices is different;

2. LAA anatomical characteristics vary between patients; we discussed in Section 1.2, the key-role of the left atrial appendage morphology in the cardiac thrombus formation responsible for stroke in patients in atrial fibrillation;

3. it is important the study of the LA diameter in order to determine the accuracy for LA enlargement assessment. Therefore, an accurate evaluation of LA volume using a three-dimensional imaging modality could be essential for improvement of AF patient selection for RFA. To this aim, a study of Abecasis et al. [39] demonstrated that LA volume was related to the outcome of radiofrequency ablation;

4. anatomical differences may cause also relevant changes in the blood fluid-dynamics within the left atrium.

Therefore, this high variability of the LA features just mentioned justifies the need of a patient-specific anatomical model of the left atrium. In the next chapters, the design and implementation of the developed patient-specific CFD model is described and applied in several projects to better understand the patho-physiology of AF and predict stroke risk. Based on the results, this tool holds promise to support the physicians in clinical practice. The CFD model has been developed through the use of the LifeV (see Section 1.3.1), a state of the art library for CFD simulations and studies. This software has been validated extensively and optimized for cardiac studies [40].

1.3.1 LifeV

LifeV is a open-source Finite Element (FE) library [41]. This software is written in C++ language, characterized by a flexible hierarchical design. LifeV provides the implementation of the most advanced mathematical and numerical methods. This library has been used to solve several engineering fields, from medical contest to the industrial one. For example, in the medical contest, LifeV enables to solve system of differential equations which describe the fluid-dynamics within the blood vessels and also in the four chambers of the heart, first of all the Navier-Stokes equations. Moreover, LifeV is developed with a parallel architecture in order to provide high computing performance for multi-core architectures.
LifeV is developed by the collaboration of three institutions: École Polytecnique Fédérale de Lausanne, Chair of Modelling and Scientific Computing (CMCS), in Switzerland, Politecnico di Milano (MOX) in Italy, Emory University, in the United States of America. The development of the library started in 2002 and actually LifeV continues to be maintained and evolved by the aforementioned research groups. It is a open source library and available from the following site:

https://https://redmine.mate.polimi.it/projects/lifev

Chapter 2

Design and Development of the computational fluid dynamics model of the left atrium

In this Chapter we focus on the description of the procedure developed to design and implement the patient-specific computational fluid dynamics model of the LA. The patient-specific CFD model was tested employing different boundary conditions and applying several motion models throughout the cardiac cycle. Part of the content of this chapter is published in:
"A proof of concept for computational fluid dynamic analysis of the left atrium in atrial fibrillation on a patient specific basis" [42]
Authors: Alessandro Masci, Martino Alessandrini, Davide Forti, Filippo Menghini, Luca Dede, Corrado Tomasi, Alfio Quarteroni, Cristiana Corsi.
Journal: ASME, Journal of Biomechanical Engineering, January 2020, 142 (1):011002.

2.1 Workflow of the study

A schematic depiction of the workflow designed and developed in this study is shown in Fig. 2.1. Briefly, our personalization pipeline involved dynamic CT imaging to reconstruct the moving patient-specific 3D atrial anatomy

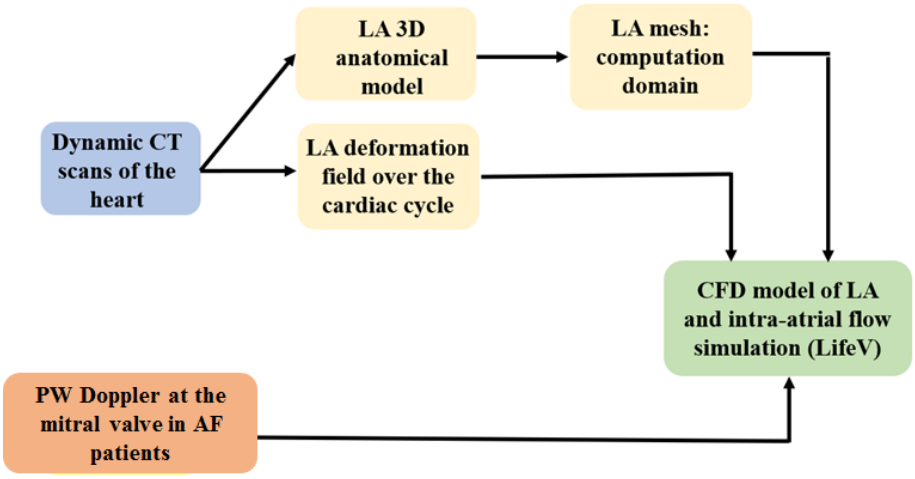

Figure 2.1: Flowchart of the steps developed in this study to derive the CFD model (green box): patient-specific data (light blue boxes) processed to derive the LA anatomical and deformation model (yellow boxes) are the inputs for the final personalized CFD model. The orange box indicates input to the model using values from the literature that are not patient-specific.

over the cardiac cycle (Fig. 2.1, light blue boxes). Processed patient data was then provided as input to the CFD solver (Fig. 2.1, light yellow boxes). A representative MV flow rate from intracardiac pulsed wave (PW) Doppler in AF patients was used to set boundary conditions for the CFD simulations (Fig. 2.1, orange box) [20]. In this preliminary study, the workflow was tested in two persistent AF patients.

2.1.1 Clinical data

Clinical data were provided by the Radiology Unit of the Santa Maria delle Croci Hospital in Ravenna. These data were processed in order to obtain the left atrium anatomical models. These images were acquired using a CT scan technique. CT produces volumes of data that can be manipulated in order to visualize bodily structures based on their ability to absorb the X-ray beam. Although, historically, the images were generated in the axial or transverse plane, perpendicular to the long axis of the body, modern scanners allow this volume of data to be acquired and reformatted along various planes or even as volumetric (3D) representation of structures. With the advances of technology through the multi-slice CT (up to 320-slices), high resolution and

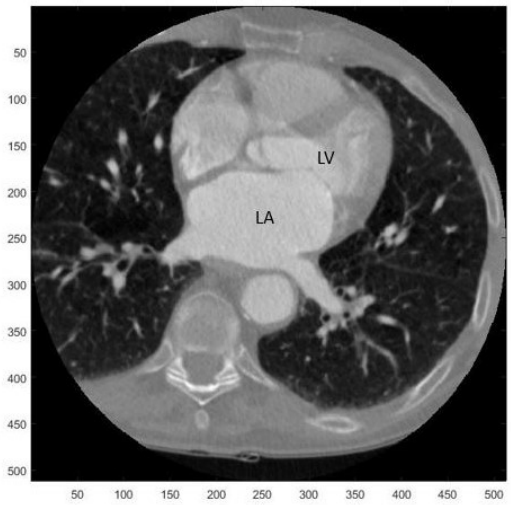

Figure 2.2: A mid slice of the 3D CT data on the axial plane that corresponds to the 10 % of the cardiac cycle (LA: left atrium; LV: left ventricle).

high speed acquisitions can be obtained at the same time, allowing excellent imaging of the heart and of the coronary arteries.

The LA model was derived from a CT dynamic acquisition after the injection of contrast medium. For optimal heart phase selection retrospective ECG gating was used. The study was approved by the Ethics IRST, IRCCS AVR Committee (CEIIAV n. 1456 prot. 6076/2015 I.5/220). Informed consent was obtained from the subjects. Volumetric CT images were reconstructed for a total of 10 phases from ventricular end-diastole (from 0 %RR to 90%RR, where RR indicates the interval between two consecutive electrocardiographic R wave peaks). Each recontructed CT volume was 512x512x180 pixels. In this way, we were able to acquire ten CT volumes representing the heart at ten different phases of the cardiac cycle. The voxel resolution was not isotropic: in-plane resolution was 0,39 mm, and through-plane resolution was 1 mm, resulting in a voxel size of 0,39x0,39x1 mm^3. As an example, in Figure 2.2, we show one slice of the 3D volume that corresponds to the 10 % of the cardiac cycle, that is the phase of the late diastole.

In the next Section, we describe how to process these images in order to obtain the anatomical model of the LA.

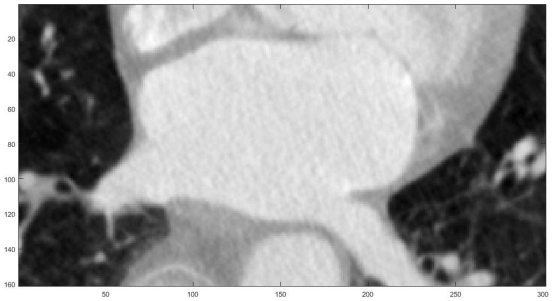

Figure 2.3: Example of the application of the cropping step in a mid slice of the CT volume.

2.2 Definition of the left atrial anatomical model

In this section, we discuss the most important features of the algorithm for LA segmentation. This algorithm was implemented in Matlab R2018b [43]. The LA was detected by processing the first volume of the CT dynamic acquisition. A volume of interest (VOI) including the LA was manually selected. The LA was detected in each image of the VOI and the 3D LA was then reconstructed. An example of this step is shown in Figure 2.3. With respect to Figure 2.2 we see that the left atrium is completely within the selected region of interest (ROI). To perform segmentation we adopted the strategy of segmenting each slice of the volume and then reconstruct the 3D left atrial structure. 2D segmentation was automatically performed applying an adaptive thresholding approach considering the histogram of each CT image. Based on the acquisition protocol, we hypothesized that the peak of the histogram corresponded to the gray level intensity of the LA chamber (int_{max}). This peak was automatically detected and, based on this value, we fixed two thresholds defined as in the following:

$$th_{down} = int_{max} - q * int_{max}, \tag{2.1}$$

$$th_{up} = int_{max} + q * int_{max}, \tag{2.2}$$

where the constant q is a percentage value: in particular, if int_{max} was in the higher tertile of intensity values, q was defined as 5%; otherwise q was set to 3%. In Figure 2.4 the result of the ROI histogram calculation is shown. In this way, we defined a particular adaptive threshold method based on the patient-specific gray level intensity corresponding to the left atrium. Thanks to this criteria, we selected only the gray levels of the image between the

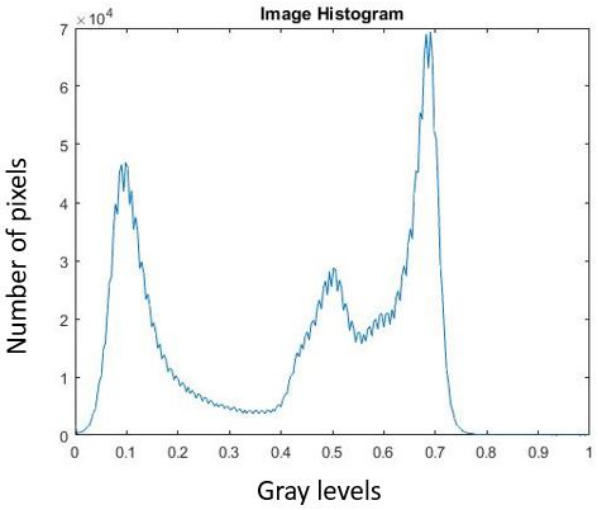

Figure 2.4: Histogram of the CT image: in x axis we find the gray levels of the image, normalized from 0 to 1; in y axis we find the number of pixels that corresponds at each gray level.

thresholds th_{down} and th_{up}. A rough detection of the LA was obtained. Further processing was designed to improve LA segmentation accuracy. We first applied some morphological operators to disconnect regions and regularize the contours. Then, for each slice, the region with the biggest area is selected. Since in the top slices of the axial acquisition the LAA might be disconnected from the LA chamber, we automatically detected these slices in which the two biggest connected regions corresponding to the LA and the LAA were selected (see Figure 2.5).

Finally, to refine the segmentation obtained in the previous steps, we applied a curvature motion to regularize the LA contour in each slice [44]. Figure 2.6 shows the result of the LA segmentation in one patient, in three of the most challenging axial slices in which the LA and the LAA (top and mid rows) and the left ventricle (bottom row) are visible.
Once applied all the steps described previously, the 3D anatomy was then obtained by stacking the 2D segmentations.
In order to comply with the requirement of providing a smooth geometrical representation of the computational domain for the CFD simulation, our 3D anatomical model was i) further filtered by applying a Laplacian smoothing using Meshlab software [45]; and ii) five cut planes were applied to the four PVs and the MV to define inflows and outflow boundary subsets of the anatomical model for the CFD simulation. This final anatomical model was

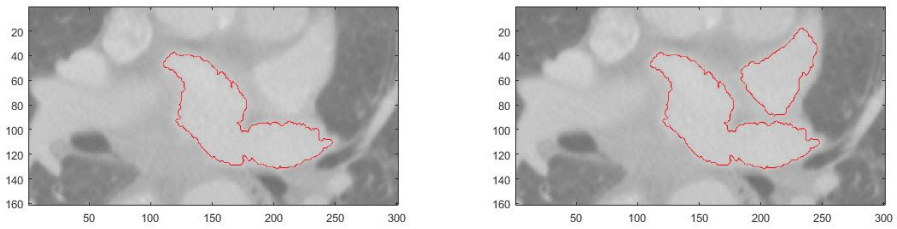

Figure 2.5: Effect of the selection of the two biggest areas in order to include the LAA. On the left panel we see the output of the previous algorithm step referring to the biggest area selection and on the right panel the effect of the selection of the second region (LAA) with the biggest area.

used as the input for the labeling and volume mesh generation algorithm: for this step the VMTK library was employed [46]. An example of the final result of the LA mesh in one patient is shown in Fig. 2.7.

2.3 Data registration for the evaluation of the LA motion

The deformation of the LA throughout the time istants of the cardiac cycle was computed by applying a 3D non-rigid image registration step of the CT volumes. For each CT volume, we computed the displacement $\mathbf{s}_{i \to i+1}(\mathbf{x})$ between two successive CT volumes $Im_i(\mathbf{x})$ and $Im_{i+1}(\mathbf{x})$. This step was preceded by the application of an affine transformation. Afterwards, the result of the affine registration was combined with the non rigid trasformation based on *B-spline* [47] model. The latter was defined as:

$$\mathbf{T}(\mathbf{x}) = \mathbf{x} + \sum_{\mathbf{x}_k \in \mathcal{N}_x} \mathbf{p}_k \boldsymbol{\beta}^3 \left(\frac{\mathbf{x} - \mathbf{x}_k}{\boldsymbol{\sigma}} \right) \tag{2.3}$$

with $\mathbf{x}_k$ the control points, $\boldsymbol{\beta}^3(\mathbf{x})$ the cubic multidimensional B-spline polynomial [47], $\mathbf{p}_k$ the B-spline coefficient vectors (the control point displacements), $\boldsymbol{\sigma}$ represents the spacing of thr B-spline control points, and $\mathcal{N}_x$ the set of all control points within the compact support of the B-spline at $\mathbf{x}$. The

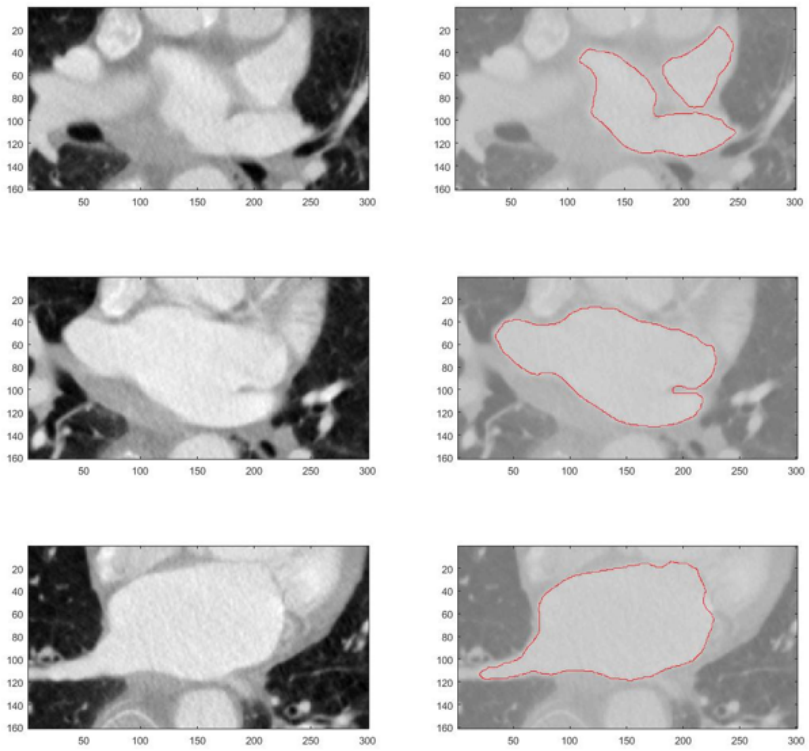

Figure 2.6: Result of the LA segmentation in three axial slices at different levels of the LA chamber: CT images are shown in the left column and the corresponding segmentation is shown in the right column. Note that in the first row the segmentation of the LAA is also visible.

control points $\mathbf{x}_k$ were defined on a regular grid, overlayed on the fixed image. The control point grid was defined by the amount of space between the control points $\boldsymbol{\sigma} = (\sigma_1, ..., \sigma_{d_{imm}})$, which could be different for each direction. The parameters in Eq. (2.3) were chosen for optimizing tracking quality as assessed visually. Moreover, we employed the mean square difference (MSD) as the image registration measure similarity. The MSD is defined as:

$$\mathrm{MSD}(I_F; I_M) = \frac{1}{|\Omega_{IF}|} \sum_{\mathbf{x}_i \in \Omega_{IF}} (I_F(\mathbf{x}_i) - I_M(\mathbf{T}(\mathbf{x}_i)))^2, \tag{2.4}$$

with Ω_{IF} the domain of the fixed image I_F, and $|\Omega_{IF}|$ the number of voxels. I_M is the moving image. Given a transformation $\mathbf{T}$, this measure can easily be implemented by looping over the voxels in the fixed image, taking $I_F(\mathbf{x}_i)$,

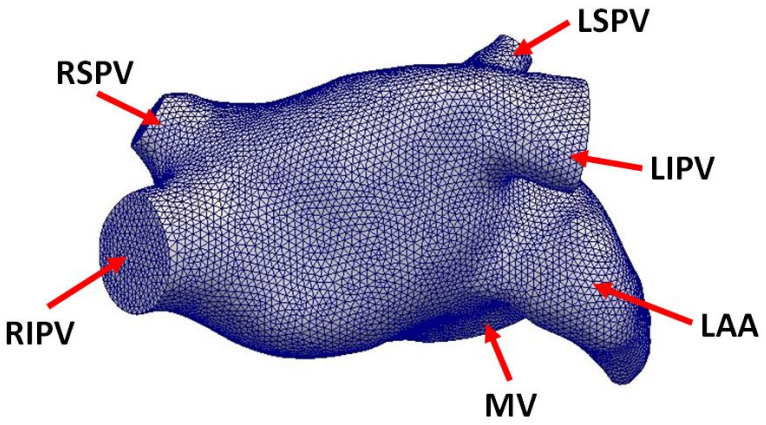

Figure 2.7: Representation of the LA mesh in one patient (RIPV: right inferior pulmonary vein; RSPV: right superior pulmonary vein; LSPV: left superior pulmonary vein; LIPV: left inferior pulmonary vein; LAA: left atrial appendage; MV: mitral valve).

calculating $I_M(\mathbf{T}(\mathbf{x}_i))$ by interpolation, and adding the squared difference to the sum.
Following this step, the global displacement of a general CT volume at time i with respect to the reference volume (time 0) was computed by increasing the successive inter-frame displacements: $\mathbf{s}_{i\to 0}(\mathbf{x}) = \mathbf{s}_{i\to n-1}(\mathbf{x}) \circ \mathbf{s}_{i-1\to 0}(\mathbf{x})$, with $\mathbf{s}_{0\to 0}(\mathbf{x}) = \mathbf{0}$. Therefore, considering $\mathbf{x}_0$ the position of a mesh vertex at time 0, the new position $\mathbf{x}_i$ at time of the position i was calculated in this way: $\mathbf{x}_i = \mathbf{x}_0 + \mathbf{s}_{n\to 0}(\mathbf{x}_0)$.
The motion field was then used to propagate the LA computational domain on the entire cardiac cycle and to simulate LA motion in sinus rhythm (SR) condition.
Unfortunately, the CT scanners available at the hospital that were involved in this study, do not allow time-resolved images during AF episodes. LA motion in AF is qualitatively defined as an irregular, disorganized, very rapid and strongly reduced contraction. In previous studies [21, 48] LA walls in AF were simulated rigid replicating the extreme condition of chronic AF when atrial contraction is not possible anymore. In our study, to simulate conditions preceding chronic AF, (paroxysmal and persistent AF conditions) we modeled atrial contraction by employing a random displacement applied independently to each vertex of the anatomical LA model and consisting in a sinusoidal function at a frequency of 4 Hz multiplied by a random factor from an uniform probability density function from 0 to 1. The contraction frequency was defined considering the typical frequency of atrial fibrillatory

episodes. Moreover, the sinusoidal wave was modulated by a small amplitude (0.1 mm) to mimic reduced contraction. This also allowed to avoid numerical issues arising from an excessive worsening of the mesh quality.
Considering this contraction model, in our two patients in persistent AF, LA volume variation throughout the cardiac cycle was very low (1-2 %). However, we believe that the adopted model could be more realistic instead of keeping the anatomical model rigid. To improve the temporal resolution, we applied the Fourier interpolation to the displacement field. Therefore, we were able to recover a continuous and periodic function from the discrete data available (10 frames for cardiac cycle). The reconstruction of a continuous displacement function was necessary to ensure the stability of the CFD numerical model. Moreover, considering the assumed periodicity of the heartbeat, we simulated and analyzed an arbitrary number of cardiac cycles, which was necessary to avoid the unphysiological initial condition on the blood flow velocity.

2.4 The computational model

In this section, we describe the computational model used to simulate the fluid dynamics in a human left atrium. The blood was assumed to be a Newtonian fluid [49] whose dynamics was governed by the unsteady Navier-Stokes equations. A crucial aspect was the choice of the reference frame where we define the PDEs, as the left atrium (whose volume stands for the computational domain) deforms along the heartbeat. To take into account the motion of the fluid domain, in this thesis we adopted the so-called Arbitrary Lagrangian Eulerian (ALE) reference frame [50], introduced in [51].

2.4.1 The frame of reference

In the framework of continuum mechanics, two reference frames are commonly used: the Lagrangian [52] and Eulerian [50] ones. The Lagrangian framework consists of following the material particles of the continuum along their motion. With this aim, when a computational mesh is introduced, it follows the continuum along its motion, in particular the mesh nodes are permanently connected to the same material points. More specifically, the material coordinates $\mathbf{X}$ allow to find out the reference configuration, $\mathbf{R}_{\mathbf{X}}$. We are able to define a map $\boldsymbol{\varphi}$, that relates the material coordinates, $\mathbf{X}$, to the

spatial ones, $\mathbf{x}$, such that

$$\boldsymbol{\varphi} : \mathbf{R}_{\mathbf{X}} \times [t_0, t_{final}) \longrightarrow \mathbf{R}_{\mathbf{x}} \times [t_0, t_{final}) \tag{2.5}$$

$$(\mathbf{X}, t) \mapsto \varphi(\mathbf{X}, t) = (\mathbf{x}, t) \tag{2.6}$$

where we link the material cordinate $\mathbf{X}$ and the spatial one $\mathbf{x}$, for each time, by this law of motion:

$$\mathbf{x} = \mathbf{x}(\mathbf{X}, t). \tag{2.7}$$

Equation (2.6) highlights the particular nature of $\boldsymbol{\varphi}$: in fact, the spatial coordinates $\mathbf{x}$ depend both on the material particles, $\mathbf{X}$, and time t. Moreover, time is measured by the same variable t in both the material and the spatial domains.

In the context of the finite element approximation and within the chosen Lagrangian framework, the material points coincide with the same mesh points during the motion and each mesh element contains the same material particles. This feature represents a significant advantage from the computational viewpoint especially in problems involving materials with history-dependent behavior. However, when the material particles are characterized by large and complex displacements, for example with vortices in the fluid, the Lagrangian approach may loose accuracy and yield severe mesh distortions. The aforementioned difficulties associated to the Lagrangian approach are overcome by the Eulerian approach [50]. This formulation consists in controlling, as time evolves, the physical quantities associated with the fluid particles passing through a fixed region of the space. To sum up, still in the finite element context, the Eulerian description consists in fixing the mesh while the continuum moves and deforms with respect to the computational grid. Through this approach we are able to even handle large distortions; however, a critical point of this method is represented by a lack of precision in the definition of the mesh boundaries.

At this stage, we integrated the positive aspects of both formulations: such a generalized description is called *Arbitrary Lagrangian – Eulerian* (ALE) description [50, 53], which is obtained by modifying the Eulerian formulation in such a manner that the fixed control volume is no longer constant but it follows the material particles of the moving boundaries. For this reason, it is necessary introduce the so-called ALE map:

$$\mathcal{A} : \hat{\Omega} \times \mathbb{R}^+ \longrightarrow \Omega_t \times \mathbb{R}^+$$

where $\hat{\Omega}$ is a reference control volume, while Ω_t is the arbitrary domain in

the deformed configuration.

2.4.2 Navier-Stokes equations in ALE formulation

The blood flow model used in this thesis consisted of a fluid governed by the incompressible Navier-Stokes equations written in the ALE frame of reference [54, 55]. This conveniently split the problem into two coupled subproblems, namely (1) the fluid problem, describing the fluid dynamics, and the geometry problem (2), which attains to the motion of the computational domain. The latter determined the displacement of the fluid domain $\hat{\mathbf{d}}_f$ which in turn defines the ALE map. To take into account the motion of the fluid domain $\Omega \subset \mathbb{R}^3$ we consider $\hat{\mathbf{d}}_f$ as an harmonic extension to the fluid reference domain of the displacement $\hat{\mathbf{d}}_{wall}$ registered at the boundary of the left atrium Ω (lateral wall, PVs and MV):

$$\begin{cases} -\Delta \hat{\mathbf{d}}_f = \mathbf{0} & \text{in} \quad \hat{\Omega} \\ \hat{\mathbf{d}}_f = \hat{\mathbf{d}}_{wall} & \text{on} \quad \partial\hat{\Omega} \end{cases} \tag{2.8}$$

We notice that $\hat{\Omega}$ is the reference domain while Ω_t is understood as the current domain.

The solution of the geometry problem defines the ALE map $\mathcal{A}_t(\hat{\mathbf{x}}) = \hat{\mathbf{x}} + \hat{\mathbf{d}}_f(\hat{\mathbf{x}}, t)$ for all $\hat{\mathbf{x}} \in \Omega$ and the current fluid domain. The Navier-Stokes equations for an incompressible fluid written in ALE coordinates read:

$$\begin{cases} \rho_f \left.\dfrac{\partial \mathbf{u}_f}{\partial t}\right|_{\hat{\mathbf{x}}} + \rho_f((\mathbf{u}_f - \mathbf{w}) \cdot \nabla)\mathbf{u}_f - \nabla \cdot \boldsymbol{\sigma}_f(\mathbf{u}_f, p_f) = 0 & \text{in} \quad \Omega_t \\ \nabla \cdot \mathbf{u}_f = 0 & \text{in} \quad \Omega_t \\ \mathbf{u}_f = \mathbf{z}_f & \text{on} \quad \Gamma_D \\ \boldsymbol{\sigma}_f \mathbf{n}_f = \mathbf{g}_f & \text{on} \quad \Gamma_N \end{cases} \tag{2.9}$$

where $\left.\frac{\partial}{\partial t}\right|_{\hat{\mathbf{x}}} = \frac{\partial}{\partial t} + \mathbf{w} \cdot \nabla$ is the ALE derivative [50], $\mathbf{w}(\mathbf{x}) = \frac{\partial \mathcal{A}_t(\mathbf{x})}{\partial t}$ is fluid domain velocity, $\mathbf{u}_f$ and p_f are the velocity and pressure of the fluid, respectively. We denoted by ρ_f the density of the fluid and by $\boldsymbol{\sigma}_f$ the Cauchy stress tensor

$$\boldsymbol{\sigma}_f(\mathbf{u}_f, p_f) = \mu(\nabla \mathbf{u}_f + (\nabla \mathbf{u}_f)^T) - p_f \mathbf{I},$$

with $\mathbf{I}$ the identity tensor, μ the dynamic viscosity of the fluid, and $\mathbf{n}_f$ the

outward directed unit vector normal to $\partial\Omega_t$. The functions $\mathbf{z}_f$ and $\mathbf{g}_f$ indicate the Dirichlet and Neumann conditions applied at the Dirichlet and Neumann boundaries Γ_D and Γ_N of Ω_t, respectively.

2.4.3 Weak formulation

We recall here from [56, 57], the weak formulation of the problem written in nonconservative form. Let us introduce the following functional spaces:

$$\begin{aligned}
U_0^f &= \{\mathbf{v} = \hat{\mathbf{v}} \circ \mathcal{A}_t^{-1} |\, \hat{\mathbf{v}} \in [H^1(\hat{\Omega})]^3, \hat{\mathbf{v}} = \mathbf{0} \text{ on } \Gamma_D\}, \\
U_z^f &= \{\mathbf{v} = \hat{\mathbf{v}} \circ \mathcal{A}_t^{-1} |\, \hat{\mathbf{v}} \in [H^1(\hat{\Omega})]^3, \hat{\mathbf{v}} = \mathbf{z}_f \text{ on } \Gamma_D\}, \\
Q^f &= \{q = \hat{q} \circ \mathcal{A}_t^{-1} |\, \hat{q} \in [L^2(\hat{\Omega})]\}, \\
U_0^d &= \{\hat{\mathbf{v}} \in [H^1(\hat{\Omega})]^3 \,|\, \mathbf{v} = \mathbf{0} \text{ on } \partial\Omega\} \\
U_{wall}^d &= \{\hat{\mathbf{v}} \in [H^1(\hat{\Omega})]^3 \,|\, \mathbf{v} = \hat{\mathbf{d}}_{wall} \text{ on } \partial\Omega\}.
\end{aligned}$$

We recall the notation for the Dirichlet boundary data for the fluid: $\mathbf{z}_f : \Gamma_D \to \mathbb{R}^3, \hat{\mathbf{d}}_{wall} : \partial\hat{\Omega} \to \mathbb{R}^3$, respectively.

The weak formulation of the problem reads: for all $t \in (0, T]$, find $\mathbf{u}_f \in U_z^f$, $p_f \in Q^f$, $\hat{\mathbf{d}}_f \in U_{wall}^d$ satisfying:

$$\begin{aligned}
&\int_{\Omega_t} \left(\rho_f \frac{\partial \mathbf{u}_f}{\partial t}\bigg|_{\hat{\mathbf{x}}} \cdot \mathbf{v} + \rho_f((\mathbf{u}_f - \mathbf{w}) \cdot \nabla)\mathbf{u}_f \cdot \mathbf{v} + \boldsymbol{\sigma}_f(\mathbf{u}_f, p_f) : \nabla \mathbf{v} \right) \mathrm{d}\Omega_t \\
&= \int_{\Gamma_N} \mathbf{g}_f \cdot \mathbf{v} \mathrm{d}\gamma \qquad \forall \mathbf{v} \in U_0^f, \\
&\int_{\Omega_t} q \nabla \cdot \mathbf{u}_f d\Omega_t = 0 \qquad \forall q \in Q^f, \\
&\int_{\Omega_t} \nabla_{\hat{\mathbf{x}}} \hat{\mathbf{d}}_f \,:\, \nabla_{\hat{\mathbf{x}}} \hat{\mathbf{v}}_g d\hat{\Omega} = 0 \qquad \forall \mathbf{v}_g \in U_0^d.
\end{aligned}$$

where $\mathbf{w}$ can also be written as $\frac{\partial \hat{\mathbf{d}}_f}{\partial t}$, the rate of deformation of the fluid domain. The initial condition of the problem is $\mathbf{u}_f = \mathbf{0}$ in Ω.

2.4.4 Space and time discretizations

For the spatial discretization, we introduced the Finite Element (FE) space $X_h^r(\Omega)$ of scalar Lagrangian basis functions of polynomial degree $r \geq 1$ over the mesh elements $K \in \mathcal{T}_h$, with $\mathcal{T}_h$ the mesh of Ω. In order to obtain the FE discretization of the problem, we consider its variational formulation and approximate, by means of finite dimensional spaces, the functional spaces introduced in Section 2.4.3. In this way, with the label $(.)_h$ we indicate the finite element spaces $U_{z_h}^f = U_z^f \cap (X_h^r(\Omega))^3$, $U_{0_h}^f = U_0^f \cap (X_h^r(\Omega))^3$, $Q_h^f = Q^f \cap (X_h^r(\Omega))^3$, $U_{0_h}^d = U_0^d \cap (X_h^r(\Omega))^3$, $U_{wall_h}^d = U_{wall}^d \cap (X_h^r(\Omega))^3$, spanned by a basis of a shape function defined in the reference domain, $\{\phi_i\}_{i=1}^{N_z}$, being $N_z = \dim(U_{z_h}^f)$. Therefore, the fluid velocity $\mathbf{u}_f$ was approximated in Ω_t as:

$$\mathbf{u}_f(x,t) \approx \mathbf{u}_{f_h}(x,t) = \sum_{i=1}^{N_z} \mathbf{u}_{f_i}(t)\phi_i.$$

The fluid pressure p_f was approximated in Ω_t as:

$$p_f(x,t) \approx p_{f_h}(x,t) = \sum_{i=1}^{N_p} p_{f_i}(t)\phi_i.$$

In this way, with notation being understood, we defined the variables $\mathbf{u}_{f_h}$ and p_{f_h} as the spatial approximations by finite element of $\mathbf{u}_f$ and p_f of degree $r = 1$. We also considered finite elements of degree $r = 1$ ($\mathbb{P}1$) for the spatial discretization of displacement field $\hat{\mathbf{d}}_{f_h}$ ($r = 1$). For this reason, the displacement field $\hat{\mathbf{d}}_f$ was approximated in Ω_t as following:

$$\hat{\mathbf{d}}_f(x,t) \approx \hat{\mathbf{d}}_{f_h}(x,t) = \sum_{i=1}^{N_d} \hat{\mathbf{d}}_{f_i}(t)\phi_i.$$

Regarding the time discretization, by using a backward difference forward (BDF) approach [58], the time derivative of the fluid problem reads:

$$\left.\frac{\partial \mathbf{u}_{f_h}}{\partial t}\right|_{t^{n+1}} \approx \frac{\alpha_o \mathbf{u}_{f_h}^{n+1} - \mathbf{u}_{f_h}^{n,BDF_\sigma}}{\Delta t}, \tag{2.10}$$

where:

$$\mathbf{u}_{f_h}^{n,BDF_\sigma} = \begin{cases} \mathbf{u}_{f_h}^{n} & \text{if} \quad n \geq 0, \qquad \text{for} \quad \sigma = 1 \quad \text{(BDF1)}, \\ 2\mathbf{u}_{f_h}^{n} - \frac{1}{2}\mathbf{u}_{f_h}^{n-1} & \text{if} \quad n \geq 1, \qquad \text{for} \quad \sigma = 2 \quad \text{(BDF2)}, \\ 3\mathbf{u}_{f_h}^{n} - \frac{3}{2}\mathbf{u}_{f_h}^{n-1} + \frac{1}{3}\mathbf{u}_{f_h}^{n-2} & \text{if} \quad n \geq 2, \qquad \text{for} \quad \sigma = 3 \quad \text{(BDF3)}. \end{cases} \tag{2.11}$$

where σ defines in this case the order of the BDF scheme. To contain the computational burden associated with the use of a fully implicit approach, we considered a semi-implicit scheme, for which the nonlinear terms are extrapolated by means of the Newton-Gregory backward polynomials [59]. Without entering into the details of the derivation, for which we refer the reader to [60], we considered the following extrapolations of orders σ = 1,2,3 for the velocity at the discrete time t_{n+1} :

$$\mathbf{u}_{f_h}^{n+1,\sigma} = \begin{cases} \mathbf{u}_{f_h}^{n} & \text{if} \quad n \geq 0, \qquad \text{for} \quad \sigma = 1 \quad \text{(BDF1)}, \\ 2\mathbf{u}_{f_h}^{n} - \mathbf{u}_{f_h}^{n-1} & \text{if} \quad n \geq 1, \qquad \text{for} \quad \sigma = 2 \quad \text{(BDF2)}, \\ 3\mathbf{u}_{f_h}^{n} - 3\mathbf{u}_{f_h}^{n-1} + \mathbf{u}_{f_h}^{n-2} & \text{if} \quad n \geq 2, \qquad \text{for} \quad \sigma = 3 \quad \text{(BDF3)}, \end{cases} \tag{2.12}$$

where we defined $\mathbf{u}_f^{n+1}$ as the numerical approximation of the velocity $\mathbf{u}_f$ at time t_{n+1} : $\mathbf{u}_f(t_{n+1})$.
In this way, for a given BDF scheme of order σ, the fully discrete linearized semi-implicit formulation of the problem reads:
find $\mathbf{u}_{f_h}^{n+1} \in U_{z_h}^f$ and $p_{f_h}^{n+1} \in \mathcal{Q}_h^f$ such that:

$$\mathcal{R}^\sigma(\mathbf{u}_{f_h}^{n+1}, p_{f_h}^{n+1}) = 0 \quad \text{for all} \quad \mathbf{v} \in U_{0_h}^f \quad \text{and} \quad q_h \in \mathcal{Q}_h^f, \ \forall n \geq \sigma - 1, \tag{2.13}$$

and

$$\begin{aligned} &\mathcal{R}^\sigma(\mathbf{u}_{f_h}^{n+1}, p_{f_h}^{n+1}) = \\ &\left(\mathbf{v}, \rho_f \frac{\alpha_0 \mathbf{u}_{f_h}^{n+1} - \mathbf{u}_{f_h}^{n,BDF_\sigma}}{\Delta t}\right) + \left(\mathbf{v}, \rho_f (\mathbf{u}_{f_h}^{n+1,\sigma} - \mathbf{w}_{f_h}^{n+1}) \cdot \nabla \mathbf{u}_{f_h}^{n+1}\right) \\ &+ \left(\nabla \mathbf{v}, \mu_f (\nabla \mathbf{u}_{f_h}^{n+1} + (\nabla \mathbf{u}_{f_h}^{n+1})^T)\right) - \left(\nabla \cdot \mathbf{v}, p_{f_h}^{n+1}\right) + \left(q_h, \nabla \cdot \mathbf{u}_{f_h}^{n+1}\right) \\ &+ \left(\rho_f (\mathbf{u}_{f_h}^{n+1,\sigma} - \mathbf{w}_{f_h}^{n+1}) \cdot \nabla \mathbf{v} + \nabla q_h, \tau_M^{n+1,\sigma} \mathbf{r}_M^{n+1,\sigma}(\mathbf{u}_{f_h}^{n+1}, p_{f_h}^{n+1})\right) \\ &+ \left(\nabla \cdot \mathbf{v}, \tau_C^{n+1,\sigma} \mathbf{r}_C(\mathbf{u}_{f_h}^{n+1})\right) - (\mathbf{v}, \mathbf{h}^{n+1})_{\Gamma_N}, \end{aligned}$$

given $\mathbf{u}_{f_h}^n, ..., \mathbf{u}_{f_h}^{n+1-\sigma}$. We find also the term $\mathbf{w}_{f_h}^{n+1}$, which is approximated

by a BDF scheme of the same order used for the time derivative of the fluid problem:

$$\mathbf{w}_{f_h}^{n+1} = \frac{\alpha_o \hat{\mathbf{d}}_{f_h}^{n+1} - \hat{\mathbf{d}}_{f_h}^{n,BDF_\sigma}}{\Delta t}. \tag{2.14}$$

In every $K \in \mathcal{T}_h$, being K a generic element of the mesh $\mathcal{T}_h$, the extrapolated stabilization parameters are defined as follows:

$$\tau_M^{n+1,\sigma} := \left(\frac{4\rho_f^2}{\Delta t^2} + \rho_f^2 (\mathbf{u}_{f_h}^{n+1,\sigma} - \mathbf{w}_{f_h}^{n+1}) \circ \mathbf{G} (\mathbf{u}_{f_h}^{n+1,\sigma} - \mathbf{w}_{f_h}^{n+1}) + \mu_f^2 C_r \mathbf{G} : \mathbf{G} \right)^{-\frac{1}{2}} \tag{2.15}$$

$$\tau_C^{n+1,\sigma} := (\tau_M^{n+1,\sigma} \mathbf{g} \cdot \mathbf{g})^{-1}; \tag{2.16}$$

and the extrapolated residuals read:

$$\begin{aligned}
\mathbf{r}_M^{n+1,\sigma}\left(\mathbf{u}_{f_h}^{n+1}, p_{f_h}^{n+1}\right) := \rho_f \left(\frac{\alpha_0 \mathbf{u}_{f_h}^{n+1} - \mathbf{u}_{f_h}^{n,BDF_\sigma}}{\Delta t} \right) + \rho_f (\mathbf{u}_{f_h}^{n+1} - \mathbf{w}_{f_h}^{n+1}) \cdot \nabla \mathbf{u}_{f_h}^{n+1} \\
+ \nabla p_{f_h}^{n+1} - \mu_f \Delta \mathbf{u}_{f_h}^{n+1}, \\
\hat{\mathbf{r}}_M^{n+1,\sigma} := \mathbf{r}_M^{n+1,\sigma}(\mathbf{u}_{f_h}^{n+1,\sigma}, p_{f_h}^{n+1,\sigma}), \\
\tilde{\mathbf{r}}_M^{n+1,\sigma}(\mathbf{u}_{f_h}^{n+1}, p_{f_h}^{n+1}) := \rho_f (\mathbf{u}_{f_h}^{n+1,\sigma} - \mathbf{w}_{f_h}^{n+1}) \cdot \nabla \mathbf{u}_{f_h}^{n+1} + \nabla p_{f_h}^{n+1} - \mu_f \Delta \mathbf{u}_{f_h}^{n+1}, \\
\mathbf{r}_C(\mathbf{u}_{f_h}^{n+1}) := \nabla \mathbf{u}_{f_h}^{n+1}.
\end{aligned}$$

In (2.16) and (2.17) the covariant metric tensor $\mathbf{G}$ was defined using a component-wise approach as $G_{i,j} = \sum_{k=1}^{3} \frac{\partial \eta_k}{\partial \mathbf{x}_i} \frac{\partial \eta_k}{\partial \mathbf{x}_i}$ and it was related to the geometrical mapping with $\eta = (\eta_1, \eta_2, \eta_3)$ of the mesh element K in the reference domain into the mesh element in Ω, while the vector $\mathbf{g}$ has components $g_i = \sum_{i=1}^{3} \frac{\partial \eta_k}{\partial \mathbf{x}_i}$. The constant $C_r > 0$ depends on the degree r of the basis function and we set it, as an element-wise inverse estimate, $C_r = 60 \cdot 2^{r-2}$ [60].
We see that, following our choice of the finite element spaces of the same degree $r = 1$, the SUPG formulation [61, 62] for the Navier-Stokes equations was employed, in order to yield a well posed problem and to control numerical instabilities arising in the advection dominated regime of the flow. Specifically, in this thesis we set $r = 1$, i.e. we considered the pair of finite elements spaces $\mathbb{P}1 - \mathbb{P}1$.
Thanks to this BDF discretization, the fully discrete semi-implicit formulation (2.13) yielded a linear problem in the variables $\mathbf{u}_{f_h}^{n+1}$ and $p_{f_h}^{n+1}$ to be

solved only once at time t_n. We discretized the time derivative of the fluid problem by a second order semi-implicit BDF scheme ($\sigma = 2$).

2.4.5 Application to the left atrium

Critical issues for the CFD simulation

Once defined the model equations, we focus our attention on the specific application of the left atrium fluid dynamics. In fact, as we were considering a moving domain, we needed to take into account a possible deterioration of the initial mesh quality. Furthermore, we defined the boundary conditions at the four pulmonary veins and at the mitral valve, considering that:

1. the inflow velocity profile can be modeled by a parabolic shape [63],
2. the inflow and outflow sections were not fixed in time and deform during the cardiac cycle.

In the following sections, we discuss in detail how to handle these critical aspects.

The domain deformation

As described in Section 2.3, thanks to an image registration procedure we were able to compute the displacement of each mesh vertex at different time steps of the cardiac cycle. However, we remark that the application of the displacement field acquired in the registration phase does not prevent from possible degeneration of the tetrahedral elements of the computational mesh. Therefore, we needed to identify a suitable procedure to avoid mesh degeneration. In particular, we imposed the displacement registered only at the boundary of the left atrium and we harmonically extended it to the interior part of the domain. Precisely, by defining $\hat{\mathbf{d}}_f \in \mathbb{R}^{3N_d}$, we can build $\hat{\mathbf{D}}_{wall} \in \mathbb{R}^{3N_d}$ obtained by extracting from $\hat{\mathbf{D}}_f$ those entries lying on its boundary Γ_{wall}.
In particular, as shown in Figure 2.8, we notice that Γ_{wall} is the union of Γ_1, Γ_2, Γ_3, Γ_4 ,Γ_5 and Γ_{lat}. We can define also Γ_D the union of Γ_1, Γ_2, Γ_3, Γ_4 and $\Gamma_N = \Gamma_5$.

Based on the displacement field acquired at the boundary of the left atrium during the registration step, we harmonically extended it to the interior of the computational domain by solving Eq.(2.9) with $\hat{\mathbf{d}}_f(\mathbf{x}_i) = \hat{\mathbf{D}}_{wall}$

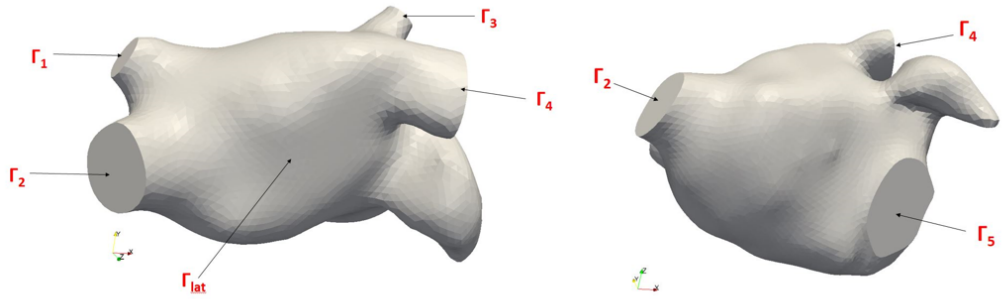

Figure 2.8: Boundary regions of the anatomical model.

at the nodes of the mesh $\mathbf{x}_i \in \partial\Omega_t$.
As an example, in Figure 2.9, we show the displacement field obtained on a slice of the domain by solving Eq.(2.9): it is clear that the left atrium walls displacement is extended harmonically within the computational domain.

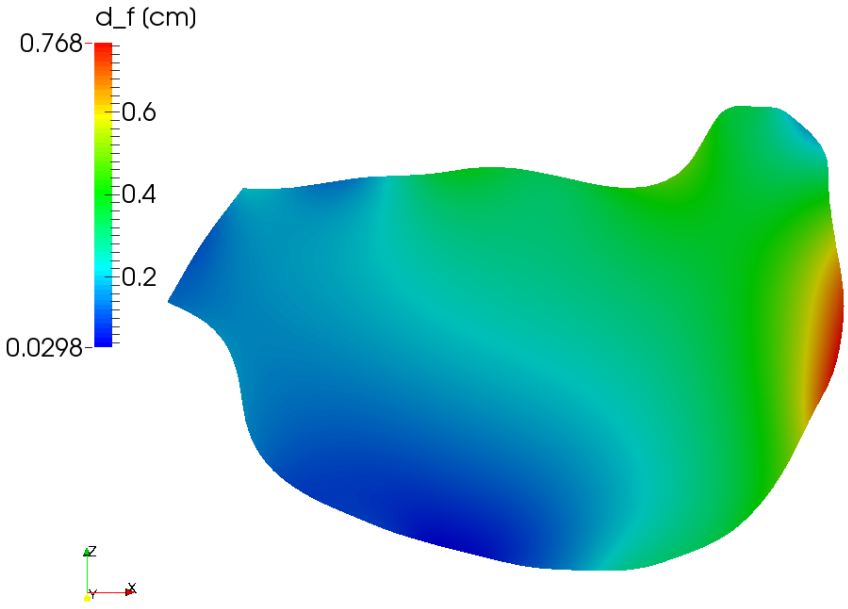

Figure 2.9: Harmonic extension of the displacement of the lateral walls within the left atrium. The computed displacement is color coded on a slice of the computational domain.

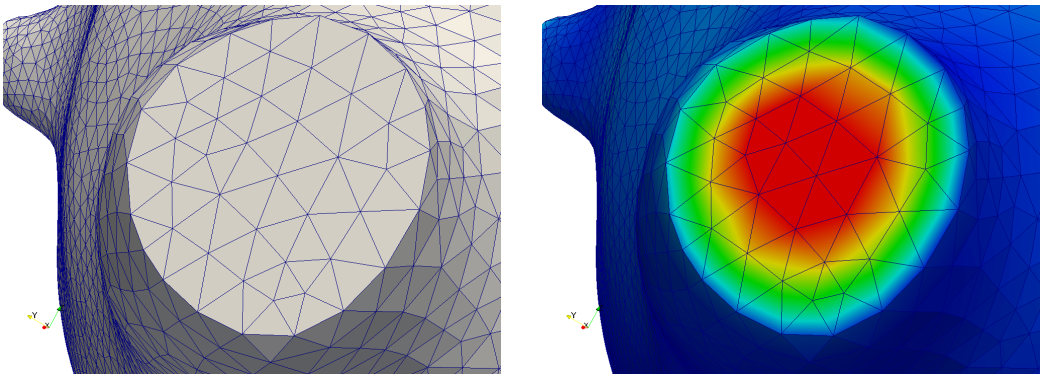

Figure 2.10: (left) Geometry and (right) the application of the pseudo-parabolic velocity profile at one Pulmonary Vein.

Boundary conditions

In this section, we discuss the imposition of the velocity profiles at the pulmonary veins. The shape of the inflow velocity was modeled by a pseudo-parabolic profile: this because the inflow sections moved and their sectional areas were not circular. To impose such a profile, we solved a Laplacian problem at each pulmonary vein to obtain such a pseudo-parabolic velocity profile:

$$\begin{cases} -\Delta \mathbf{u}_{BC} = \mathbf{1} & \text{in} \quad \Gamma_D \\ \mathbf{u}_{BC} = \mathbf{0} & \text{on} \quad \Gamma_{lat} \end{cases} \tag{2.17}$$

where $\mathbf{u}_{BC}$ is the solution of (2.17) and $\Gamma_{lat} = \partial\Gamma_D$ is the wall boundary region, as shown in Figure 2.8. Through this procedure we imposed a pseudo-parabolic flow profile at each pulmonary vein (see Figure 2.10) to be suitably rescaled by the flowrate. Indeed, at this stage we still needed to compute the amplitude of the pseudo-parabolic profile at each pulmonary veins. Once solved the laplacian problem, the solution of the problem (2.17) was weighted with the flowrate that we wanted to impose at each pulmonary veins.
Regarding the choice of the flowrate to assign at each PV, first we considered a representative mitral valve Doppler velocity profile from [20]. For the MV flowrate computation, we multiplied the MV Doppler velocity by the MV cross sectional area in order to obtain Q_O. Afterwards, it was suitable adapted to our application. We carried out this choice because, for the two patients analyzed, the PW Doppler velocity measurements at the MV were not available. In Figure 2.11, we see the MV flow rate used. The mitral valve flow shows typical characteristic: in the first phase the MV flow is null and this is related to the ventricular systole phase, where the MV must be

closed in order to allow the left ventricle to push all the blood only in the aorta. During this phase of the cardiac cycle, the blood flow comes from the pulmonary veins causing the LA filling (i.e. atrial diastole). Once the ventricular systole is ended, the aortic valve closes and we observe the ventricular relaxation (diastolic phase). Indeed in this phase, there is a pressure cross-over between left atrial and left ventricular pressures, which causes the MV to open and LV rapid filling to occur (E wave). In this part of the cardiac cycle LV relaxation is still ongoing causing a continuing drop in LV pressure. After this rapid filling, the residual part of the blood flow inside the left atrium is pushed towards the MV through the contraction of the LA. Therefore, we observe another peak after the E wave, named the A wave. The A wave is associated to the atrial contraction and is an important index of diastolic function. The area under the A wave reflects the contribution of atrial contraction to LV diastolic filling. In patients affected by atrial fibrillation, the contribution of the A wave is not significative: this is due to the fact that the atrium cells contraction is no longer syncronized. Moreover, cells morphology suffers from changes during the years, causing a reduced contraction activity of the left atrium, which affects the amplitude of the A wave.

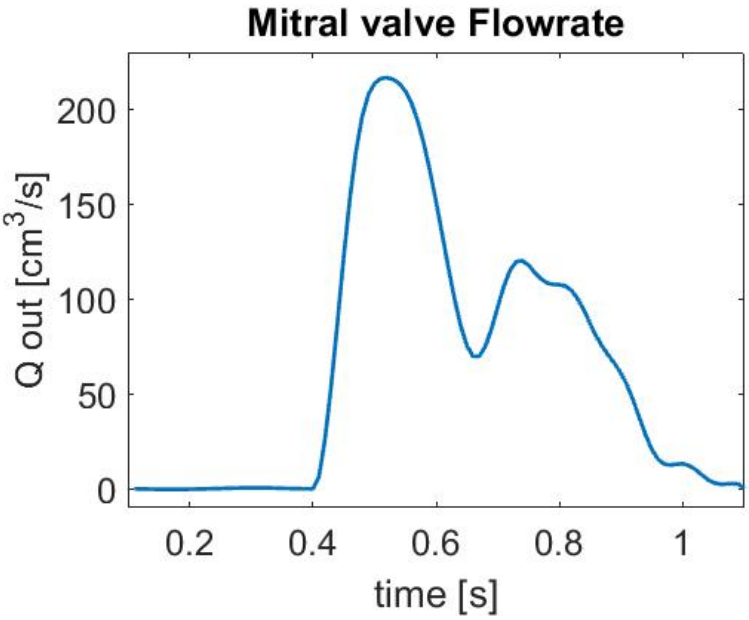

Figure 2.11: Mitral valve flow-rate in one cardiac cycle, used in order to compute the four PVs flow rate.

To assign the flow rate at each PV, having available the mitral valve flow

rate, we wrote the mass balance with the help of the Figure 2.12:

$$Q_1^{pv} + Q_2^{pv} + Q_3^{pv} + Q_4^{pv} + Q^O + Q_{wall} = 0 \tag{2.18}$$

$$Q_{wall} = \frac{dV}{dt} \tag{2.19}$$

where $Q_i^{pv}, (i = 1, 2, 3, 4)$ are the flow rates of each pulmonary veins, Q_O is the flow rate of mitral valve (Figure 2.11) and Q_{wall} stands for the flux associated to the volume variation. This can be easily computed: once we know the displacement of the computational domain, we can compute the domain deformation velocity. From this data, we easily obtain the volume variation $\frac{dV}{dt}$.

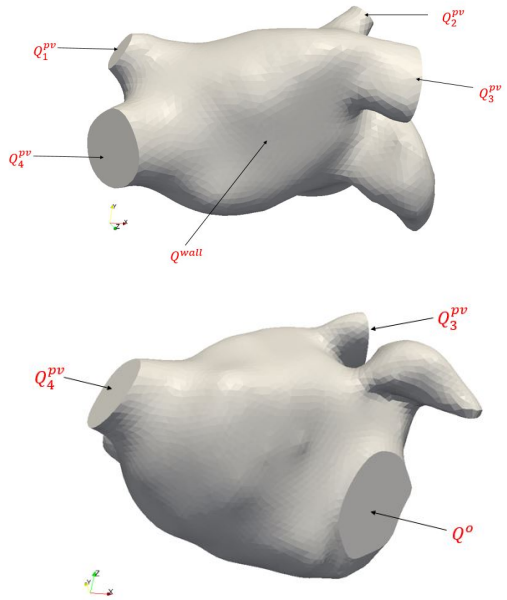

Figure 2.12: Fluxes at the boundaries.

From Eq.(2.19), we defined Q_{tot}^{pv}, the total flux at the PVs, in this way:

$$Q_{tot}^{pv} = Q_1^{pv} + Q_2^{pv} + Q_3^{pv} + Q_4^{pv} \tag{2.20}$$

Afterwards, we assigned the total flux Q_{tot}^{pv} through the four pulmonary veins with a criteria based on their sectional area. To this aim, we solved the

following equation:

$$Q_l^{pv} = \frac{A_l}{A_t} Q_{tot}^{pv}; \qquad l = 1, 2, 3, 4. \tag{2.21}$$

where A_l is the sectional area of each PV and A_t is the sum of PVs sectional areas. In this way, at each timestep, we were able to evaluate the flow rate at each PV to be applied at the computational model.

Eq.(2.21) was then modified by considering the PVs sections move and their area change during the cardiac cycle:

$$Q_l^{pv} = \frac{A_l}{A_t} Q_{tot}^{pv} - Q_l^{w}; \qquad l = 1, 2, 3, 4, \tag{2.22}$$

where the new term Q_l^w, which is not present in Eq.(2.21), represents the flow due to the mesh velocity for each PV. Finally, for AF condition simulation, we redefined the inflow boundary conditions by removing the A-wave from the representative MV flowrate signal Q^0 and each PV flowrate was recomputed as described before.

Penalization of the reverse flow at the mitral valve

To limit the presence of backflows as they may give rise to numerical instabilities, at the outflow (mitral valve) boundary $\Gamma_5 = \Gamma_{out}$, we considered the following natural boundary condition [64]

$$-p_f \mathbf{n} + \mu(\nabla \mathbf{u}_f + (\nabla \mathbf{u}_f)^T) \cdot \mathbf{n} - \rho_f(\{\mathbf{u}_f \cdot \mathbf{n}\}_-)\mathbf{u}_f = \mathbf{0} \quad \text{on} \quad \Gamma_{out}, \tag{2.23}$$

where $\mathbf{n}$ is the outward directed unit vector normal to Γ_{out} and $\{\mathbf{u}_f \cdot \mathbf{n}\}_-$ denotes the negative part of $\mathbf{u}_f \cdot \mathbf{n}$:

$$\{\mathbf{u}_f \cdot \mathbf{n}\}_- = \begin{cases} \mathbf{u}_f \cdot \mathbf{n} & \text{if} \quad \mathbf{u}_f \cdot \mathbf{n} < \mathbf{0}, \\ \mathbf{0} & \text{if} \quad \mathbf{u}_f \cdot \mathbf{n} \geq \mathbf{0}. \end{cases} \tag{2.24}$$

The above boundary condition was introduced to weakly penalize the reverse flow eventually induced by the backflows at Γ_{out}, which may render unstable the discrete formulation of the problem. Indeed, we observe that only if $\mathbf{u}_f \cdot \mathbf{n} < \mathbf{0}$ on Γ_{out}, the last term in the left hand side of Eq.2.23 is active; if $\mathbf{u}_f \cdot \mathbf{n} \geq \mathbf{0}$ on Γ_{out}, the outflow boundary condition reduces to the well known stress-free condition.

2.4.6 Numerical simulations

For each patient, we performed two numerical simulations: one corresponding to sinus rhythm (SR) and one corresponding to AF condition. As underlined in the previous sections, SR and AF differ in the motion model employed: SR employed the patient-specific motion model extracted from the CT volumes. AF was instead simulated by applying independently to each mesh vertex a random displacement. The mitral valve flowrate employed in SR was the one in Figure 2.11, while in AF we removed the A-wave due to the atrial contraction.

The SR and AF simulations were run for seven cardiac cycles. The results of the first three cycles were disregarded to avoid the influence of the unphysiological initial condition on the blood flow. Then, the results of the remaining cycles were phase-averaged: for example, the velocity field in every point of the domain and at a given time of the first useful heartbeat was averaged with that of the field at the corresponding point, but at times of the following heartbeats. In this manner, an average heartbeat was obtained, to account for the variability in the solution due to the nonlinearity in the Navier-Stokes equations. Steady states were not reached, as it is intrinsic in the nature of the problem, but a phase-average solution was obtained provided that a sufficiently large number of heartbeats was involved in the averaging process. In practice, for this kind of simulation, 6-7 heartbeats suffice as shown in [18]. Moreover, this kind of phase-averaging allowed a statistical study of the blood flow, in terms of cycle-to-cycle variations.

In the Results and Discussion section we report the results of the averaged simulated cardiac cycle in both conditions.

2.5 Results and Discussion

In Table 2.1, we reported the information on the LA computational meshes of both patients and the respective number of degrees of freedom (DOFs) of the fluid dynamics problem. Regarding the criteria adopted for the choice of the number of DOFs, we employed the same orders of magnitude with respect to the other works in literature on this type of simulations [17,19–22]. Moreover, a preliminary sensitivity study on the LA CFD simulations was performed in [65].

Concerning the parameters of the fluid dynamics model, the time step was set to 0.001 seconds, dynamic viscosity was 0.035 *poise* and the density was set to 1.06 g/cm^3. For each simulated condition, we evaluated and reported the most significant parameters able to describe LA fluid dynamics including

Table 2.1: Number of vertices, tetrahedra of computational mesh, and associated number of DOFs of the fluid problem for both the patients geometries.

	Vertices	Tetrahedra	DOFs
Mesh 1	170,428	1,042,766	681,712
Mesh 2	131,158	798,838	524,632

velocity and vortex structures within the LA in both patients. For a better visualization of the vortex structures the use of the Q-criterion was preferred:

$$Q = \frac{1}{2}(\mathbf{W}_{ij}\mathbf{W}_{ij} - \mathbf{S}_{ij}\mathbf{S}_{ij}); \tag{2.25}$$

being $\mathbf{S}_{ij} = \left(\frac{\partial \mathbf{u}_{f_i}}{\partial \mathbf{x}_j} + \frac{\partial \mathbf{u}_{f_j}}{\partial \mathbf{x}_i}\right)$ and $\mathbf{W}_{ij} = \left(\frac{\partial \mathbf{u}_{f_i}}{\partial \mathbf{x}_j} - \frac{\partial \mathbf{u}_{f_j}}{\partial \mathbf{x}_i}\right)$ the symmetric and anti-symmetric parts of the velocity-gradient tensor $\frac{\partial \mathbf{u}_{f_i}}{\partial \mathbf{x}_j}$. Through this quantity, we identified the connected regions where $Q > 0$ and the pressure was lower than the ambient value as the vortexes core.
Lastly, we focused on the fluid dynamics of the LAA: the analysis of LAA behaviour is not trivial, however it could represent an important aspect in the evaluation of the stroke risk in atrial fibrillation.

2.5.1 Velocity and vorticity analysis

An example of the computed PVs flowrates for the SR and AF simulations are shown in Fig. 2.13. Focusing on the PV flowrate profile in SR condition, the S- and D-waves are clearly recognizable in the figure. The first antegrade wave occurs during the LA reservoir phase (atrial diastole) where the blood flow comes from the PVs and the LA is filling and expanding. This wave is named S-wave. Then, in a PV flowrate we clearly recognize a second antegrade wave, named D-wave. When the MV opens and the LV rapid filling starts, the flow continues to enter in the LA through the PVs, thus implying a second peak in each PV flowrate.
Moreover, immediately after the atrial contraction, a third wave occurs. This wave is retrograde occurring during the final part of the ventricular systole and it is a consequence of the atrial contraction that pushes back a small amount of the blood flow from the LA to the PVs. This wave is named A_r. The amplitude of the S- wave is strongly reduced with respect to the

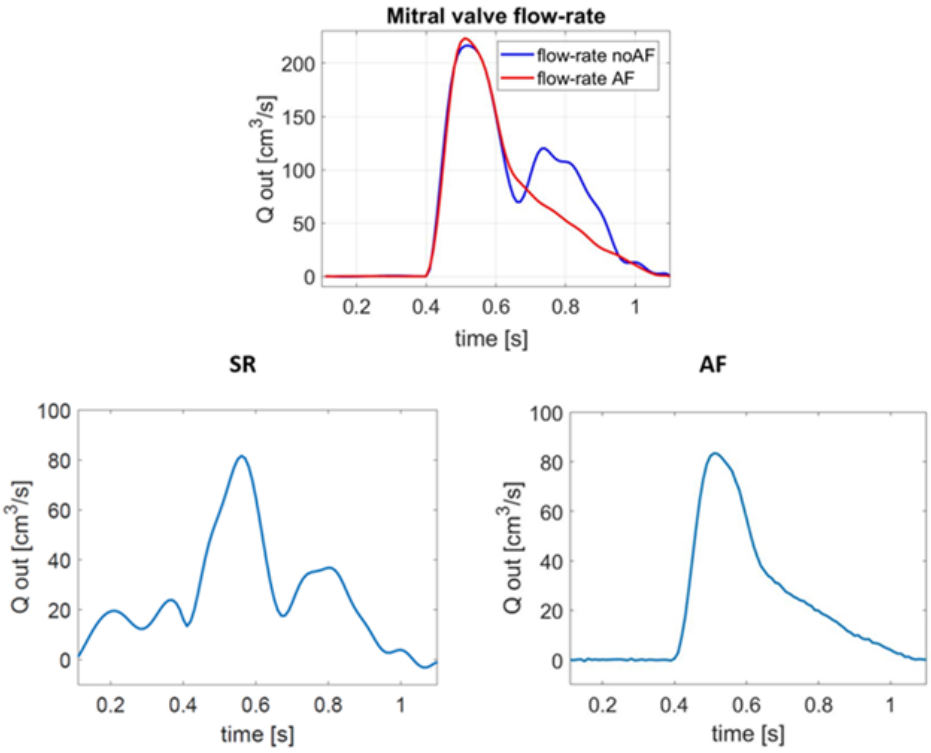

Figure 2.13: Fist row: MV flowrate allows to recongnize the different phases of the cardiac cycle; Second row: examples of the computed PV flowrate for the SR simulation (left panel) and for the AF simulation (right panel) in one cardiac cycle.

physiological condition [66], which is probably due to changes in the LA cell contractile activity caused by persistent AF, implying a scarse expansion of the LA during ventricular systole. Moreover, a very small retrogade flow in correspondence of the late diastole phase, immediately after atrial contraction, can be easily recognized.
In Fig. 2.14 the LA volume variation in SR condition throughout the heartbeat is depicted. We can see that the value of the LA volume was higher (mean value throughout the cardiac cycle: $110\,cm^3$) than physiological values ($20 \div 40\,cm^3$) and also the maximum volume variation over the cardiac cycle was reduced the 10 % whereas in healthy LA the volume variation could be more than 40 %. These findings confirmed the anatomical and functional changes of the LA chamber due to the persistence of AF.
The simulated LA blood velocity in the two patients is displayed in Fig. 2.15. In patient 1, in the first row of Fig. 2.15, representing blood flow velocity during the ventricular systole, we observed that flow velocity in the pulmonary

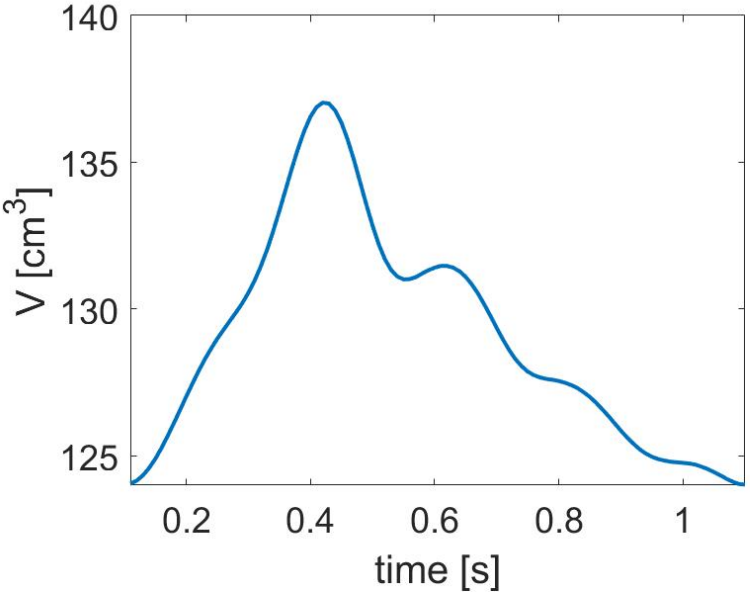

Figure 2.14: LA chamber volume variation throughout the cardiac cycle in SR condition.

veins showed an increment in the SR condition (mean value $15 \div 20$ cm/s) with respect to the AF one (mean value $5 \div 10$ cm/s). This increment was due to the atrial diastole: according to the principle of mass conservation, volume variation must be compensated by the entrance of blood flow from the PVs. The magnitude of the velocity field was still relatively small, in particular we noticed the highest velocity close to PVs was $15 \div 20$ cm/s. We also appreciated an increase of the velocity in the left-bottom part of the LA, which was probably caused by a significant expansion of this area, which retrieved blood and consequently resulted in an increase of the local fluid velocity. In AF condition we did not appreciate an increment of velocity at PVs with respect to the SR condition: the enhanced difference was probably an effect of the random motion model that characterizes this condition. In fact, during AF, LA expansion was not evident and PV velocities remained mostly null.
During the LV filling phase, namely in the first part of LV diastole (second row of Fig. 2.15) we found an appreciable increase of the velocity in proximity of the MV. In this phase, the mitral valve was open and blood rapidly flowed from the LA to the LV. Velocity at the MV reached the peak value of $65 \div 70$ cm/s. An expected increase of PV velocity was confirmed by the simulation results (mean value 30 cm/s). In this phase we did not notice

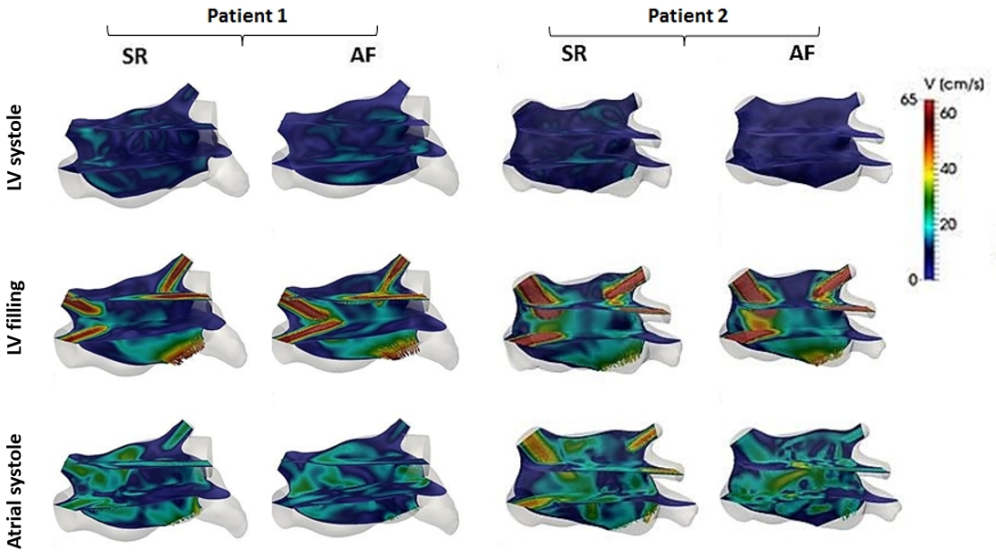

Figure 2.15: Blood flow velocity distributions within the LA shown in the two patients in SR (first/third column) and in AF (second/fourth column) at different times during the cardiac cycle: LV sistole; LV filling (E-wave); atrial systole (A-wave) in the first, second and third row respectively. To allow better visualization, blood flow distribution is shown in 3 orthogonal planes.

relevant differences between the two simulated conditions.
During atrial systole (third row of Fig. 2.15), we appreciated an important difference between the SR and AF conditions. In fact, we observed an expected increment of the blood flow velocity in proximity of the MV only in SR simulation (peak value $35 \div 40$ cm/s): this difference was due to the A wave peak of the MV flowrate, which corresponded to the atrial contraction. For the AF condition, the A wave was instead missing and for this reason we did not observe an increment of velocity at the MV. In fact, the velocity value remained about $20 \div 25$ cm/s.

For patient 2 (see Fig. 2.15), as expected, we found that the velocity distribution within the LA was very similar to the ones obtained in patient 1. Since both patients suffered from persistent AF, it was not unexpected that the LA volume variation throughout the cardiac cycle in SR condition were very similar between them. We noticed that, in patient 2, velocity in proximity of the MV during the first phase of ventricular diastole reached the value of 55 cm/s, which was a lower value compared to patient 1 ($65 \div 70$ cm/s), and it was probably due to the difference of the MV annulus area, larger in the second analysed patient, thus implying a lower velocity through the outflow. Moreover, just like in patient 1, the complexity of the flow

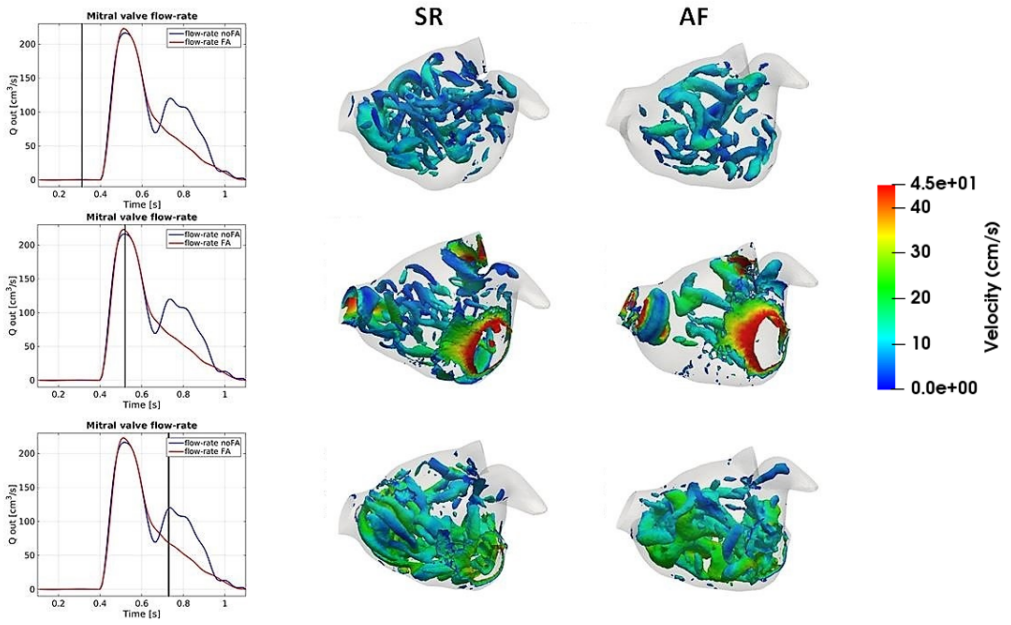

Figure 2.16: Visualization of the vortexes structures within the LA in patient 1, at three instants of the cardiac cycle.

pattern within the LA was enhanced by the tridimensional representation of the velocity field.

Regarding the representation of the vortex structures within the left atrium, results are shown in Fig. 2.16 and 2.17.
Vortex dynamics was very complex during the ventricular systole (first row, Fig. 2.16) and the number of vortex structures was higher in SR condition than in AF. We hypothesize that the velocity distribution in the atrial vortices may favor a better “washout" effect and avoid intra-atrial blood flow stasis. For this reason, a smaller number of vortexes of the same intensity in AF condition may promote blood stasis within LA.
In correspondence with the first part of the ventricular diastole (second row, Fig. 2.16), vortex structures increased and were associated to high velocity values. In particular, four vortex rings were ejected from the PVs and propagated towards the center of the atrial cavity. Moreover, vortexes around the MV caused by the exit of the blood flow in this phase, were visible.
During the second part of the ventricular diastole (third row, Fig. 2.16), the propagation of these vortex rings from the PVs brought them into direct interaction with each other and lead to a vortex breakup and consequently to a decrease of the vortex structures or dissociation into a number of small-scale vortex structures: this was due to collisions between vortexes at various

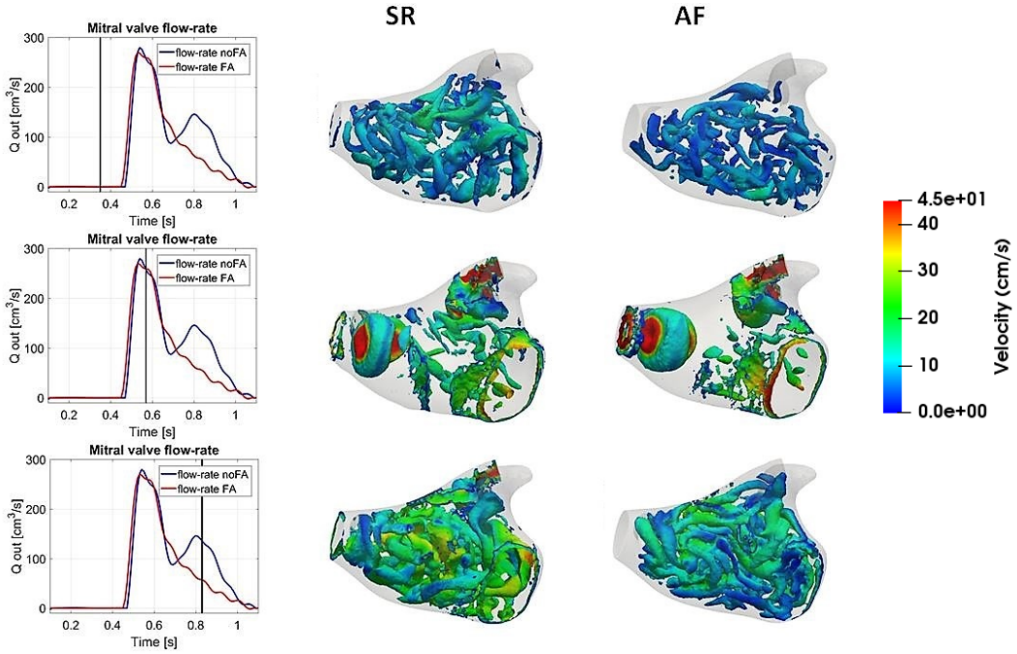

Figure 2.17: Visualization of the vortexes structures within the LA for patient 2, at three instants of the cardiac cycle.

inclination angles and their subsequent breakdown was due to non-uniform stretching and enhanced viscous dissipation. Moreover, vorticity annihilation between the vortex patches was another key mechanism for the rapid dissipation of these vortexes. We also observed that most of these vortex structures passed through the MV in the left ventricle. We did not notice appreciable differences between the two simulated conditions, however it was clear that throughout the cardiac cycle, large vortex structures were generated more frequently in the SR condition than the AF one. Our interpretation was that an AF episode could promote a worse blood flow "washout" effect in the LA, increasing the risk of the intra-atrial blood flow stasis.
Vorticity and the vortex structures simulated in the patient 2 are reported in Fig. 2.17. We noticed many similarities in the formation of vortex structures between the two patients including the number of vortex structures which was higher in SR condition than in AF also in this patient. However, it seemed that these structures were more numerous and showed higher velocity values compared to the patient 1.

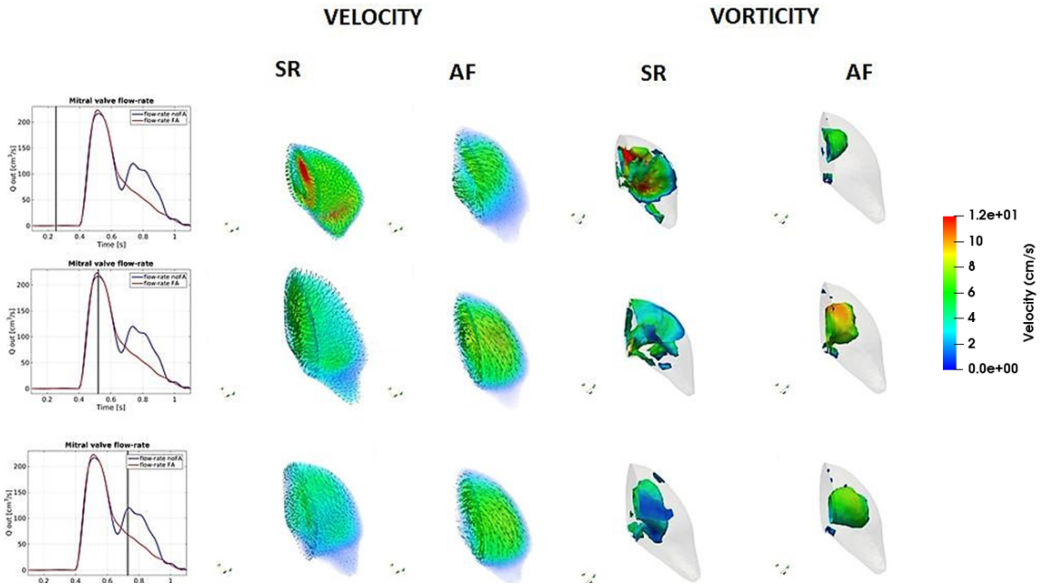

Figure 2.18: Visualization of the velocity and of the vortexes structures within the patient 1 LAA at three instants of the cardiac cycle.

2.5.2 Analysis of the LAA fluid dynamics

In Fig. 2.18 we represented the velocity and the vortex structures within the LAA for one patient in three time instants of the cardiac cycle.
During ventricular systole in SR, the mean velocity increased (peak value 12 cm/s) and a significant blood flow passed through the left atrial appendage. During AF we did not appreciate this increase of blood flow within the LAA and velocity remained lower, about 7 cm/s.
In ventricular diastole we noticed that fluid started to exit from the LAA. In fact, in this phase the MV opened and the blood flow passed rapidly from the LA to the LV. The mean velocity in the LAA seemed to be slightly higher in AF condition than in the SR one. Moreover, in this phase the LAA contraction in the SR condition was clearly evident, which promoted an increased release of blood flow rate, compared to the AF condition.
Then, during the atrial contraction, blood continued to exit from the LAA in the SR condition while it seemed that in AF simulation the blood remained within the LAA and the differences in the blood flow patterns were due to the lack of motion of the left atrial appendage owing to the presence of the pathology that may cause blood stasis in the LAA. At these three time instants of the cardiac cycle, we observed that velocity in the distal part of the LAA remained almost null for the AF condition with respect to the SR one: this could imply an increment of the thrombi formation probability in this

part of the LAA.
To sum up, we observed that the LAA motion throughout the cardiac cycle in the SR condition promoted the release of the blood from the LAA, while in the AF condition the lack of contractile activity of the LAA may promote the blood stasis. Moreover, the mean velocity of the blood flow within the LAA throughout the cardiac cycle seemed slightly larger in the SR condition than in the AF one. Concerning the analysis of the vorticity within the LAA, we noticed from Fig. 2.18, as in the LA, that the number of vortex structures occurred more frequently in the SR condition than in AF. As explained before in the analysis of the vortex structures in the LA, this phenomenon could promote a worse blood flow "washout" effect also within the LAA during an AF episode.
Finally, to quantify a measure of the blood flow stasis in the LAA, we simulated seven cardiac cycles for both conditions. We populated the LAA with 500 fluid particles at the beginning of the fourth heartbeat and we counted how many particles remained inside the LAA after three cardiac cycles (e.g. end of the simulation). The fluid particles were distributed as a sphere around the center c, which represents the midpoint of the LAA centerline.
For patient 1, we found that, after three cardiac cycles, 26% of the particles remained in the LAA in SR condition, while 45.6% remained in the LAA, in AF condition.
For patient 2 we found that, after three cardiac cycles, 39% of the particles remained in the LAA in SR, while 50.2% remained in the LAA in AF condition. Fig. 2.19 shows the distribution of the fluid particles in the LAA after three cardiac cycles for the AF simulation in the two analyzed patients.
These results confirm AF may promote blood stasis in LAA. In fact the reduction of atrial contraction in AF could imply an expected reduced "washout" of the LA, as explained before, and mainly of the LAA, although more acutely for the first patient which, in the long term, might be indicative of the generation of blood clots.

2.5.3 Summary of the study

In this study we developed, to the best of our knowledge, the most advanced effort towards a fully personalized CFD model of atrial blood flow in AF. Hereto, dynamic imaging data were used to extract patient specific detailed anatomy and motion model during SR. Moreover, a realistic MV flowrate profile was used to set inflow and outflow boundary conditions. The designed workflow was tested in two different conditions, SR and AF. Differently from previous works in which LA walls in AF were considered rigid [21, 48], in our

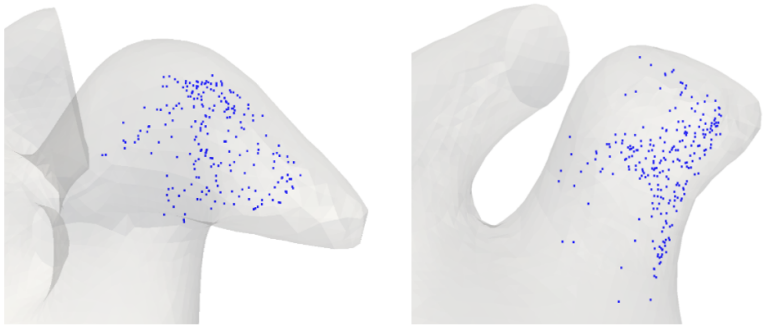

Figure 2.19: Fluid particles distribution in the LAA after three cardiac cycles for the AF simulation in the first and second analyzed patients (left and right panels, respectively).

study LA motion in AF was modeled by applying a random displacement to reproduce a disorganized and unsyncronized contraction. In this preliminary testings, the model highlighted expected differences in velocity and vortex formation in the two conditions and confirmed that AF episodes resulted in a reduced "washout" of the LAA compared to the SR condition, which may lead to the formation of thrombi.
Our study has several limitations that we will better address in the next chapters of the thesis. First of all the results of the model in the two analyzed patients were not benchmarked against experimental clinical measurements, which were not available. In the next chapters of the thesis we will show the model application on patients in which personalized intra-cardiac Doppler flow measurements are available. Indeed, the developed approach could be easily extended to patient specific boundary conditions: in particular, having available the PW Doppler measurements from intracardiac echocardiography at the MV and PVs, the flowrates for the CFD model boundary conditions imposition can be directly computed for each patient.
Blood flow dynamics obtained in a healthy LA is missing and a comparison with respect to the simulated blood dynamics in SR/AF in a persistent AF LA may provide a better understanding of the haemodynamic implications of AF. In the next chapters of the thesis, we will show the application of the developed pipeline to a larger number of AF subjects, presenting a different range of atrial morphology and function. Moreover, we will focus on the different anatomic types of the LAA in order to understand their impact on blood flow stasis.

Moreover, the motion field used for AF simulation was based on a modelling approach. New strategies for AF wall motion simulations could be more realistic than using a random displacement function as the one employed in this study. Indeed in the next Section of this Chapter, we will focus on this aspect in order to study and test different contraction models in AF.

2.6 Development of different cardiac contraction models in AF

The necessity of a realistic motion model of the atrial cavity during an AF episode is a crucial point for a creation of a complete patient-specific atrial fluid dynamics model. Therefore, the aim of this study was the design and development and testing of different contraction model of the LA. These motion models are used as input for the computational fluid dynamics model of the left atrium in order to enhance the differences in haemodynamics parameters for each LA motion model used for the simulations. The developed model was tested in patients in both sinus rhythm (SR) and AF for a comprehensive evaluation of hemodynamic implications of AF episodes in both LA and left atrial appendage (LAA). For this study, we considered the first AF patient LA anatomical model that we analyzed in the previous Sections. Having available the motion model throughout the cardiac cycle for the simulation of the SR condition, we developed three different motion models in order to simulate the AF condition.

2.6.1 Random Motion Model

To simulate conditions preceding chronic AF (paroxysmal and persistent AF conditions) we chose first to model atrial contraction by employing a random displacement applied independently to each vertex of the anatomical LA model and consisting in a sinusoidal function at a frequency of 4 Hz multiplied by a random factor from an uniform probability density function from 0 to 1. The contraction frequency was defined considering the typical frequency of atrial fibrillatory episodes [67]. Moreover, the sinusoidal wave was modulated by a small amplitude (0.1 mm) in order to avoid numerical issues arising from an excessive worsening of the mesh quality. This type of approach was used to simulate the AF condition in the previous Sections in order to compare it to the SR simulation. In figure 2.20(a), we show a schematic description of

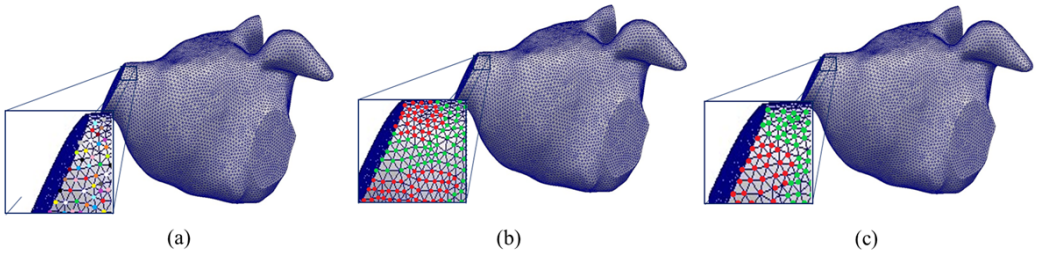

Figure 2.20: Graphical representation of the contraction models of the LA: (a) random motion model; (b) discrete motion model; (c) sinusoidal motion model.

this first motion model chosen for simulating contraction during AF episodes.

2.6.2 Discrete Motion Model

In this model the idea was to divide the LA mesh in neighbouring regions and apply on each one of them a different displacement field. More specifically, LA mesh was divided in 16 regions and we imposed to each region a random contraction/expansion motion model following the radial direction with respect to the midpoint of the region. In figure 2.20(b), we observe the application of this method on a specific part of the LA mesh. Moreover, to comply with the contraints of the CFD model, we applied a smoothing function that allowed to keep the mesh elements transitions at the boundary between two adiacent regions smooth, in order to avoid the mesh quality degeneration.

2.6.3 Sinusoidal Motion Model

The most critical point of the previous model was to manage the mesh points at the boundary between two adjacent regions that could create great degeneration of the mesh quality. For this reason, to simulate the simultaneous contraction/expansion of LA adjacent anatomical regions in a continuous way, we applied this particular sinusoidal function:

$$\mathbf{d}(\mathbf{\Theta}) = r(\mathbf{\Theta}) \cdot \sin(\frac{2\pi\mathbf{\Theta}}{L}) \cdot \sin(\omega t); \tag{2.26}$$

where r represents the maximum displacement amplitude, $\mathbf{\Theta}$ the position referred to the center of mass of the atrial cavity, and L the spatial period. Amplitude and frequency of the sinusoidal wave were chosen by following the

work of [20]. L was set to 8 mm, representing the number of periodic repetitions of the sinusoidal wave through the spatial mesh domain. Amplitude and frequency were setted to 1 mm and 4 Hz respectively. Figure 2.20(c) shows the description of the aforementioned displacement model applied to the LA mesh nodes.

2.6.4 Results and Discussion

The CFD model described in Section 2.4 was used to apply the developed three motion models in order to simulate the LA motion in AF. Moreover, the motion field of the LA extracted by the dynamic CT sequence was employed in order to perform the CFD simulation of the LA in SR. Seven cardiac cycles were simulated for each motion model. We discarded the first two in order to avoid the influence of the unphysiological initial condition on the blood flow. Therefore, the last 5 cardiac cycles were considered for the analysis.
Blood velocity, kinetic energy, vortex structures and blood stasis in the LA were analyzed in both SR and AF conditions.
From the analysis of the CFD simulation results, we found that the most important differences in the four motion models were during the atrial diastole phase. Indeed, we found an increment of the velocity up to 15-20 cm/s in proximity of the pulmonary veins (PVs) only for the SR simulation. For the three motion models of AF we found a slightly increment of the PVs velocity only for the sinusoidal model and not for the other two motion fields, as shown in Figure 2.21. The sinusoidal model leads to a higher expansion of the atrial chamber and consequently to an higher flowrate through the PVs with respect to the discrete and random models. During the MV opening, i.e. beginning of the ventricular diastole, we observed a strong increment of the velocity (more than 45 cm/s) at the MV for all the models, as shown in Figure 2.22. No relevant differences were detected in this phase between the SR simulation and the three AF motion models simulations. Another relevant difference in the cardiac cycle between the four simulated conditions is during the atrial systole: despite its reduction caused by the persistence of the AF, we found an increase of the velocity at the mitral valve (MV) for the SR simulation with respect to the other three. This was probably related to a contractile activity of the LA that pushes blood through the MV in the LV. However, in three motion models simulating AF this increment of the velocity at the MV was strongly reduced, as depicted in Figure 2.23.

The most important differences between the simulated conditions were observed in the LAA looking at the velocity and vorticity. Indeed, the three AF models resulted in different velocities both at the tip and at the ostium

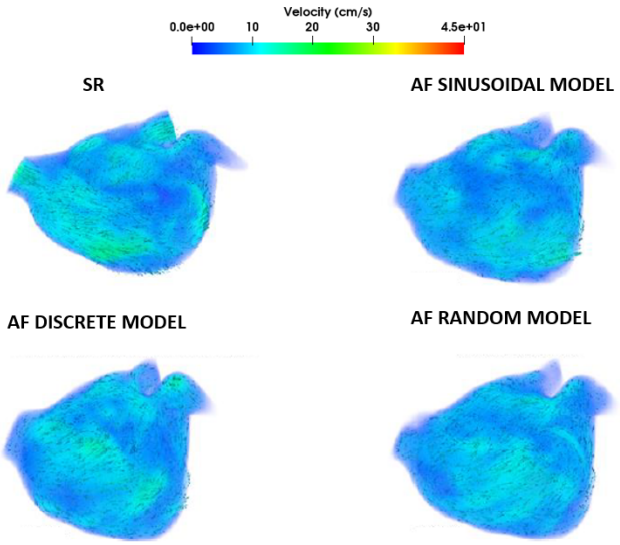

Figure 2.21: LA velocity field computed by the CFD model for SR condition and for the three motion models used for simulating AF in the atrial diastole phase. The image refers to the last cardiac cycle simulated.

of the LA appendage during the ventricular systole phase (see Figure 2.24). The SR condition, as expected, showed higher velocities inside the LAA (up to 11 cm/s) and consequently a better washout of the blood flow expecially in the LAA distal part. Regarding the three AF simulations, the one in which we applied the sinusoidal motion model showed higher velocities inside the LAA with respect to the other two displacement fields. Moreover the blood flow could reach also the LAA tip with this particular motion model, thus favouring a lower risk of blood stasis and thrombi formation. In the ventricular diastole (see Figure 2.25) we saw that the blood flow started to exit from the LAA and the velocity was slightly higher in the AF simulations with respect to the SR condition.
During the last phase of the atrial contraction (see Figure 2.26), we observed an increment of the velocity in the AF sinusoidal model simulation with respect to the others up to 10 cm/s that helped the washout of the blood flow expecially if compared to the other two AF motion models. We noticed that also during the ventricular diastole and the atrial systole the velocity in the distal part of the LAA was higher in the SR condition with respect to the AF simulations. However, also in these phases of the cardiac cycle it seems that AF sinusoidal motion models allowed the blood flow to reach also the tip of the LAA with respect to the discrete and random model.

In order to confirm these findings, we computed the vorticity and there-

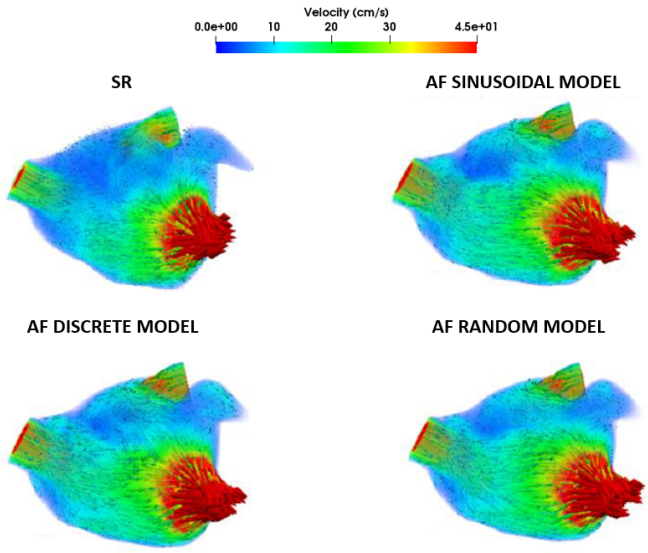

Figure 2.22: LA velocity field computed by the CFD model for SR condition and for the three motion models used for simulating AF at the beginning of ventricular diastole phase.The image refers to the last cardiac cycle simulated.

fore we represented the vortex structures in the LAA by using the Q-criterion. As we can observe from Figures 2.27 and 2.28, we noticed that most of the vortex structures were located near to the LAA ostium. In SR, we found a higher number of vortex structures overall the LAA throughout the cardiac cycle with respect to the AF simulations. The AF sinusoidal motion model allowed the vortex structures to reach with a higher probability the LAA tip expecially with respect to the random model simulation where the vortex structures were concentrated near the LAA ostium. In SR the vortex structures are bigger with respect to the AF simulations thus implying a better washout of the blood. However, comparing the different AF simulations, the one that showed, in these two time instants depicted in Figures 2.27,2.28 and also throughout the cardiac cycle, bigger and higher velocity vortex structures was the AF sinusoidal model condition. Moreover we observed in the last phase of the cardiac cycle (see Figure 2.28) that in AF sinusoidal model simulation the vortex structure near to the LAA had an higher value of the velocity (approximately 11-12 cm/s) compared to the other simulations.

From velocity and vortex structures analysis, as expected, blood washout was more effective in SR with respect to the three AF simulations. Considering the three contraction models, the sinusoidal model was the one showing an adequate blood washout, despite less than SR condition, thus implying a lower thrombi formation risk and consequently stroke risk.

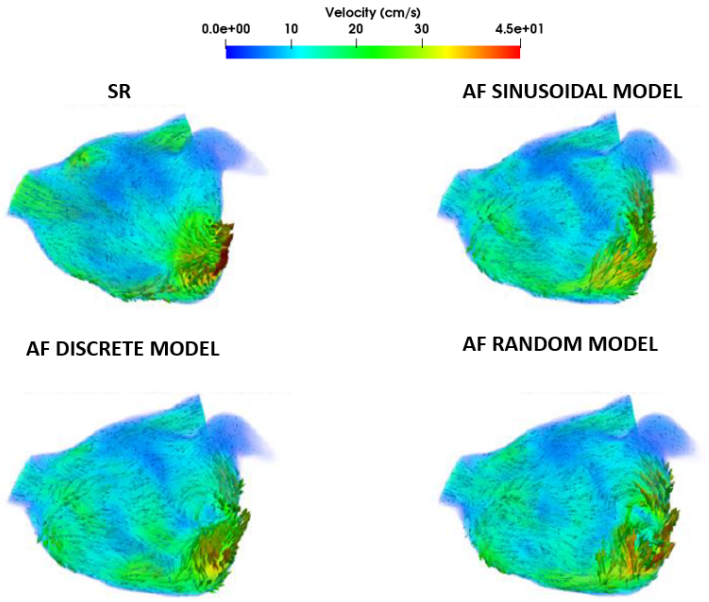

Figure 2.23: LA velocity field computed by the CFD model for SR condition and for the three motion models used for simulating AF in the atrial systole phase. The image refers to the last cardiac cycle simulated.

In order to confirm the aforementioned findings, we performed a specific study to try to quantify the LAA blood stasis. Indeed, we populated the LAA with 500 fluid particles at the beginning of the simulation and counted how many remained inside the LAA after each cardiac cycle. After 5 cycles, 6.6% of the particles remained in the LAA in SR, while 10.6% remained in AF with the sinusoidal motion model. 14.6% remained in AF with the discrete motion model and 17% in AF with the random model. These results confirmed our considerations based on the velocity and vorticity analysis. We found an expected reduced washout expecially for the AF random model and discrete model AF which in the long term might be indicative of the generation of blood clots.

In conclusion, we have seen that the choice of the motion model for simulating the AF condition affected the fluid-dynamics parameters. This aspect could strongly influence the results, expecially compared to keep fixed the LA during an AF episode, as employed in the studies focused on this topic in literature, and it could have a relevant impact in the clinical decisions.
Obviously, the results of this study could benefit from the application of a patient-specific motion field of the LA in AF. Unfortunately, up to date,

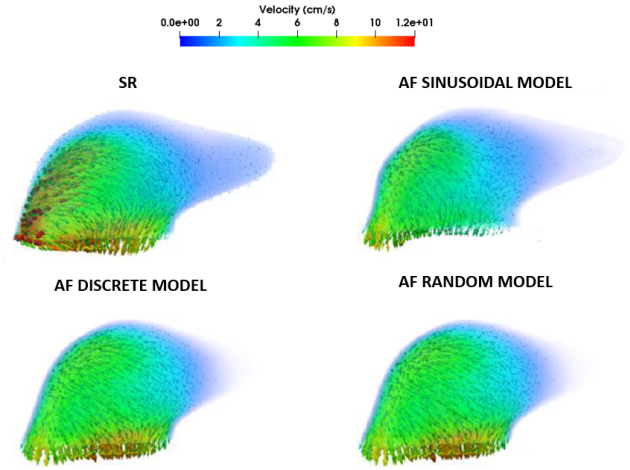

Figure 2.24: LAA velocity field computed by the CFD model for SR condition and for the three motion models used for simulating AF in the ventricular systole phase. The image refers to the last cardiac cycle simulated.

quantification of such a motion field is not possible using the standard 3D acquisition, MRI or CT.
Therefore, additional studies should be performed to develop a realistic contraction model to simulate AF episodes.

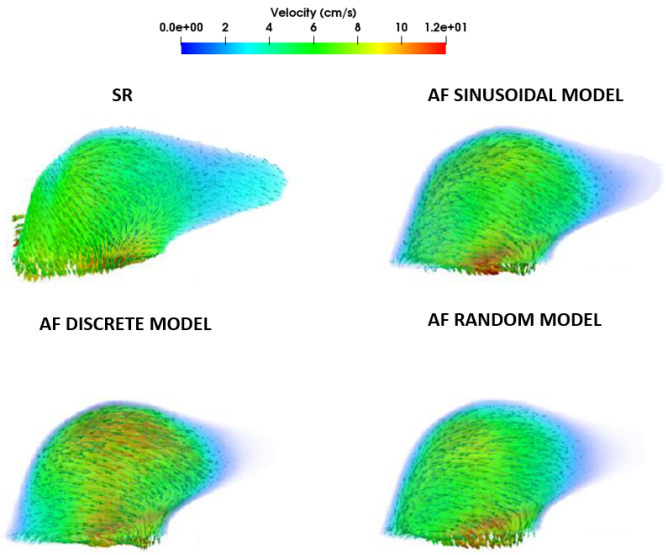

Figure 2.25: LAA velocity field computed by the CFD model for SR condition and for the three motion models used for simulating AF in the ventricular diastole phase. The image refers to the last cardiac cycle simulated.

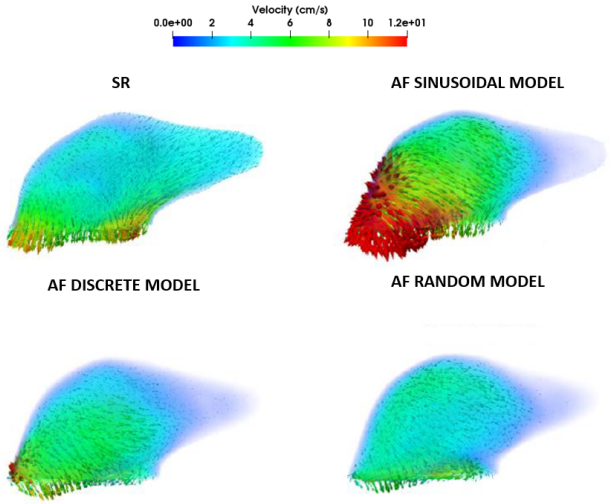

Figure 2.26: LAA velocity field computed by the CFD model for SR condition and for the three motion models used for simulating AF in the last phase of the atrial systole phase. The image refers to the last cardiac cycle simulated.

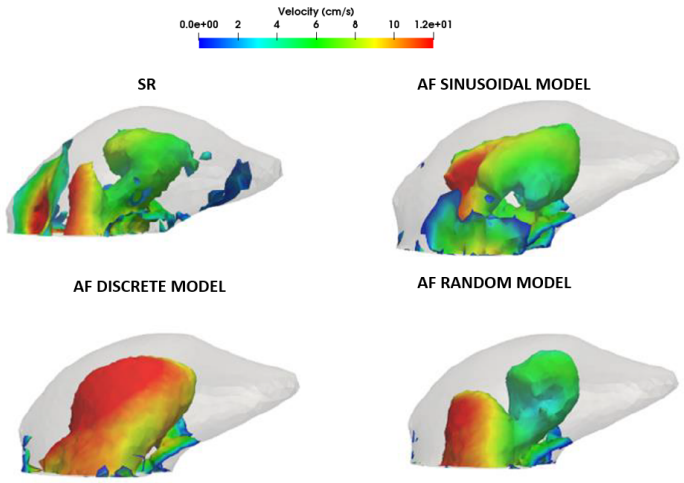

Figure 2.27: LAA velocity field computed by the CFD model for SR condition and for the three motion models used for simulating AF in the ventricular systole phase. The image refers to the last cardiac cycle simulated.

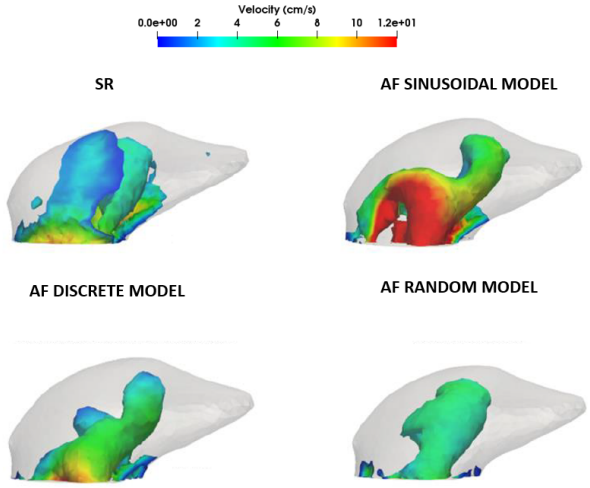

Figure 2.28: LAA velocity field computed by the CFD model for SR condition and for the three motion models used for simulating AF in the last phase of the atrial systole phase. The image refers to the last cardiac cycle simulated.

Chapter 3

The impact of LAA morphology on stroke risk assessment in AF

In this chapter we focus on the design and development of the workflow to quantify the influence of LAA morphology on the LA hemodynamics. Part of the content of this chapter is published in:
"The impact of left atrium appendage morphology on stroke risk assessment in atrial fibrillation: a computational fluid dynamics study" [68]
Authors: Alessandro Masci, Lorenzo Barone, Luca Dede, Marco Fedele, Corrado Tomasi, Alfio Quarteroni, Cristiana Corsi.
Journal: Frontiers in Physiology, January 2019, 22, 9:1938

3.1 Background

As described in detail in Section 1.1.1, LAA is the remnant of the embryonic left atrium where the smooth-walled LA originates from the primordial pulmonary vein and its branches [69]. Because of its hooked morphology, the LAA is the left atrial site of the highest blood stasis risk, increasing the incidence of thrombus formation and stroke. In fact, 90 % of the intracardiac thrombi in patients with cardioembolic stroke/TIA are considered as originating in the LAA [14]. Oral anticoagulation therapy was the only option available until recently. However, it increases bleeding risk and interpheres with other drugs and multiorgan functioning, and its risk can overtake the

otherwise remakable benefits on thromboembolic events. [15].
For these reasons, different strategies have been developed such as the use of interventional treatments, i.e. LAA percutaneous closure, which seems to better reduce the risk of thromboembolism compared to warfarin anti-coagulation therapy [16]. Unfortunately, these treatments are restricted to small subgroups of patients, due to the procedural risks and costs which may overcome the preventive antiembolic efficacy. As highlighted in Section 1.1.1, in the studies of Di Biase et al. and Jeong et al. [3, 23], morphological and quantitative features of LAA have been increasingly studied in the past few years. Despite these attempts, the association between the aforementioned LAA anatomical features and stroke risk does not seem straightforward, and conflicting results have been published. Moreover, it is still uncertain what is the best strategy for stroke prevention in AF. To this purpose, several clinical studies suggested that stroke risk stratification could be improved by using hemodynamic information on the left atrium (LA) and mainly on the left atrial appendage (LAA) [13, 70]. To the best of our knowledge, the interplay of the geometric parameters such as LAA length, tortuosity, surface area and volume with the fluid dynamics parameters have not been investigated. This analysis might highlight new insights into the effects of atrial fibrillation on the LAA haemodynamics, thus providing a better understanding of the thrombi formation risk. Moreover, previous studies considered not only different LAA morphologies for the CFD simulation but also different LA shapes which varied for each patient analyzed. Therefore, considerations regarding the LAA fluid dynamics and mainly its thrombogenicity could be affected also by the variation of the other LA anatomical structures. Therefore, the aim of this study was the design and development of a workflow to quantify the influence of LAA morphology alone on the LA hemodynamics.

3.2 Workflow of the analysis

A schematic workflow of the project is shown in Fig. 3.1.

3.3 Patients data

The data-set consisted of five LA 3D anatomical models. These models were extracted from CT (one) and MRI (four) data, in patients affected by AF. The study was approved by the Ethics IRST, IRCCS AVR Committee (CEI-IAV n. 1456 prot. 6076/2015 I.5/220). All subjects gave written informed

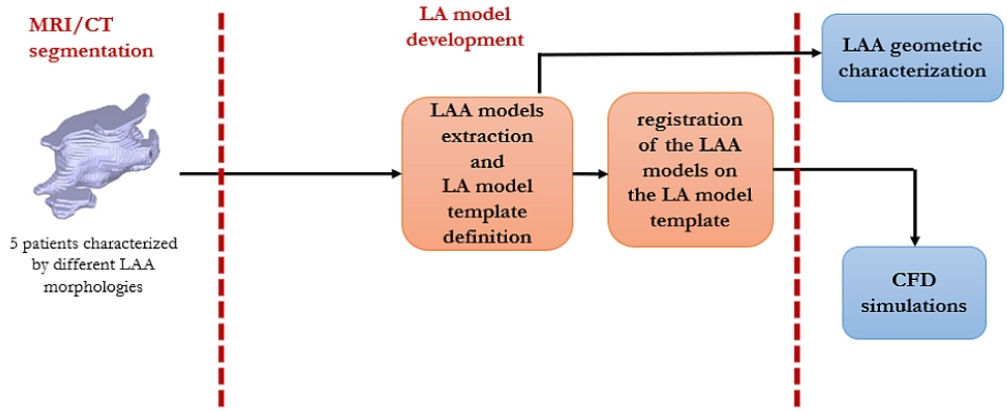

Figure 3.1: A schematic description of the workflow of this study

consent in accordance with the Declaration of Helsinki.
Data were processed with specifically designed in-house image segmentation algorithms, described in Section 2.2 and in [71, 72]. From the 3D LA binary masks, we generated the surface meshes by using the MATLAB iso2mesh toolbox [73].

3.4 LAA extraction

The next step was focused on the implementation of an algorithm which automatically recognized and isolated the LAA from the data-set of left atrial anatomical models. To this purpose, the shape diameter function (SDF) proposed by Shapira et al. [74] was employed. Most of previous segmentation approaches were based on local surface properties, such as curvature or geodesic distance, that often depend on the topology and on the pose of the object. SDF overcame this problems and provided a link between the surface mesh and the object's volume. SDF defines a scalar function on the mesh surface M ($f_s \colon M \to \mathbb{R}$) that measures the local object diameter. From a point s, a cone of rays was sent towards the interior of the mesh in the opposite direction to the normal at s and the distance between s and the intersection of each ray with the mesh was computed. Furthermore, only the rays whose length fell within one standard deviation from the median of all lengths were considered. The final SDF value at the point s was defined as the weighted average of the remaining lengths, where the weight values were the inverse of the angle between each ray and the center of the cone. In this study, the SDF was calculated for each 3D surface using the CGAL software [75].

An example of the SDF values computation for one LA anatomical model is depicted in Fig. 3.2.

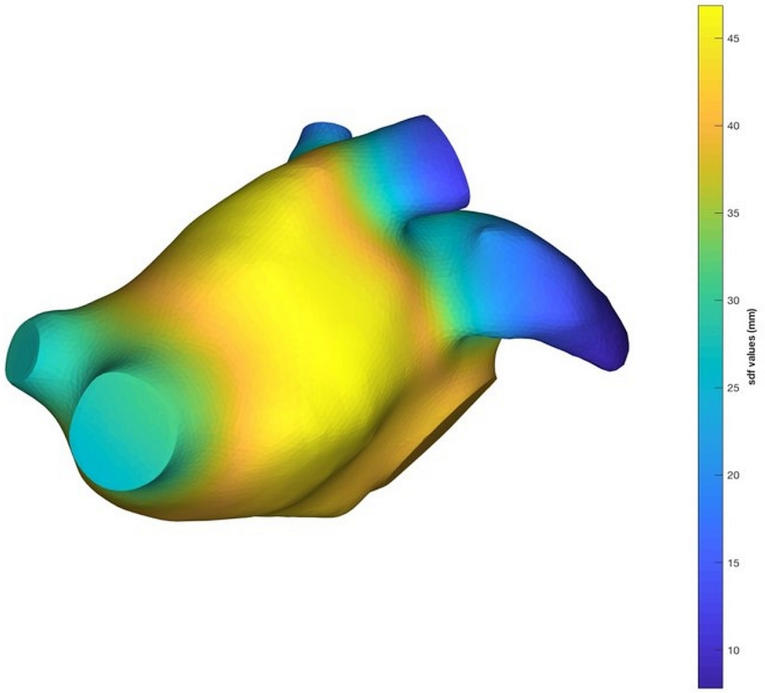

Figure 3.2: An example of the SDF result on a LA mesh.

The SDF values created iso-contours on the mesh which were used to separate regions with different SDF values. Based on this idea, we obtained a semantic clusterization of our 3D models where each cluster had a different id number. The output of this procedure was a vector that contained a label for each facet. This step allowed the identification of pulmonary veins (PVs), LA chamber and LAA for each mesh. In order to identify the LAA, we detected the atrial chamber identifier by calculating the mode (statistics) of the label vector; afterwards we assigned to the PVs the same identifier of the LA chamber. Based on the anatomical position of the LAA we were able to select this region of interest in order to automatically detect it and isolate from the LA surface mesh. An example of the result of this step is shown in Fig. 3.3.
Applying this approach, we were able to detach the LAAs from the original patient-specific models. Five LAA surface meshes were obtained. Once the LAA was removed, the LA mesh shown in Fig. 3.2 was used as template for the definition of the new LA anatomical models, each one characterized by a particular LAA morphology derived from the other four models.

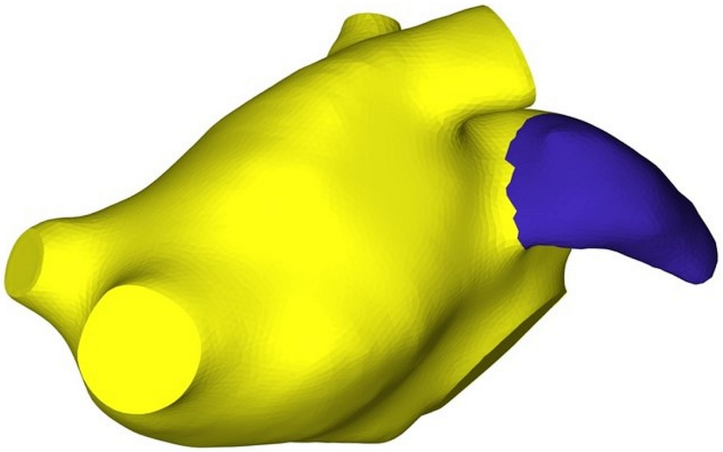

Figure 3.3: LAA vertices and faces detection.

3.5 LAA alignment and definition of the new LA models

Once the previous steps were performed, in order to accomplish the alignment between the LA template and the LAA meshes, we identified the vertices which belong to LAA ostia and the LA ostium template. The output was a vector that contained the detected vertex coordinates. The local correspondence between LAA and LA template ostium vertices was achieved by using the iterative closest point (ICP) algorithm [76]. The ICP algorithm matched closest points between two point data sets: one was used as a fixed data set and the other as a floating data set. In our case, the fixed one was composed by vertices of the LA ostium and the floating one by the LAA ostium vertices.

The ICP algorithm iteratively performed the following steps:

1. Matching: for each vertex of the floating data set, the nearest neighbor vertex of the fixed data set was found;

2. Minimization: the error metric was minimized between these two set of vertices;

3. Transformation: floating data points were then mapped in the new space using the computed transformation.

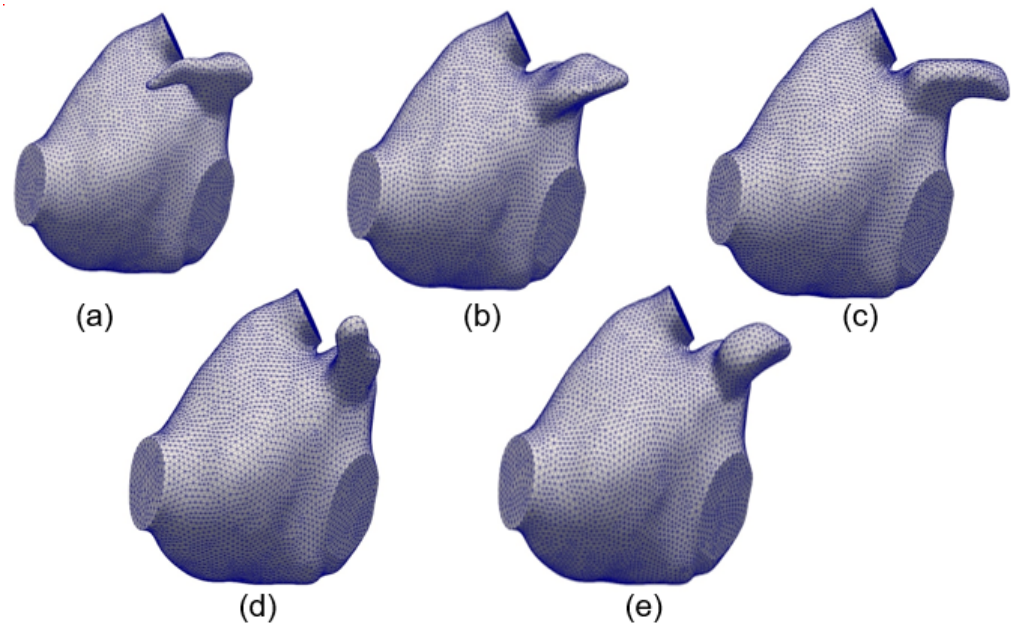

Figure 3.4: The five LA anatomical models obtained by the automatic framework described in sections 2.2 and 2.3. (a) refers to the LA model with the LAA1, (b) the one with the LAA2, (c) with the LAA3, (d) with the LAA4 and (e) with the LAA5.

Once this procedure was employed, a set of five LA anatomical models, presenting the same atrial chamber but different LAA geometries, was created.

Finally, in order to refine the anatomical models and to comply with the requirement of providing a smooth geometrical representation of the computational domain for the CFD simulation, a Laplacian smoothing filtering and Poisson surface reconstruction were applied by using MeshLab [45].

3.5.1 LAA geometrical parameters and CFD model

The five anatomical models created by the framework described above are illustrated in Fig. 3.4. The shape and the geometry of the LAAs were different and, in order to quantify the differences between the LAAs and their impact on the haemodynamic characteristics, we performed a specific analysis by quantifying LAA volume, LAA surface area, length, tortuosity and LAA orifice perimeter and area. Length was evaluated by the LAA

centerlines computation. Tortuosity was defined as [77]:

$$\mathcal{X} = \frac{L}{D} - 1; \tag{3.1}$$

where L is the centerline length and D is the Euclidean distance between the centerline endpoints. Tortuosity values much higher than 0 reflect the complexity of the LAA shapes, whereas values near to 0 describe more orderly LAA geometries.
In order to compute the LAA volumes and orifice (i.e. LAA ostium) areas, LAA volume meshes were generated. For this step, the VMTK library was employed [46]. The finite element count for each LA mesh is reported in Table 3.1. The LA volume meshes represented the computational domain of the CFD model.

	Mesh size (# of finite elements)
LA model with LAA1	1,878,564
LA model with LAA2	1,767,432
LA model with LAA3	1,923,543
LA model with LAA4	1,698,675
LA model with LAA5	1,716,897

Table 3.1: Mesh size of each analyzed model.

3.6 CFD model

The CFD model used for the simulation of the haemodynamics of each anatomical model was the one described in detail in Section 2.4. Regarding the imposition of the boundary conditions, we considered a mitral valve (MV) flowrate Q^0 from [20]. This flowrate was suitably modified for our application: indeed, we removed the atrial contraction wave (A wave) because this is strongly reduced during AF [78]. Afterwards, the flowrate at each pulmonary vein (PV) was computed by using the procedure described in Section 2.4.5. The numerical discretization of the CFD model was implemented in LifeV, a state-of-art library for the CFD simulations in the parallel setting

(see Section 1.3.1). Twenty cores (Intel Xeon processor E5, 2.5 GHz) were used for each LA CFD simulation.

3.6.1 Numerical simulation and fluid dynamics parameter computation

For each LA anatomical model, we performed a simulation in AF condition. We modeled atrial contraction motion by employing the random displacement approach (see Section 2.6.1). Simulations were run for five cardiac cycles to avoid the influence of the unphysiological initial condition on fluid velocity. We report the results of the fifth simulated cardiac cycle.
Regarding the parameters of the fluid dynamics model, the time step was set to 0.005 seconds, dynamic viscosity was 0.035 *poise* and the density was set to 1.06 g/cm^3.
The most significant parameters able to describe LAA fluid dynamics including velocity and vortex structures, LAA orifice velocity and mainly the residence time were computed. For the computation of the vortex structures the Q-criterion was employed. Through this quantity, we identified and visualized some connected regions where $Q > 0$ and the pressure was lower than the ambient value at the vortexes core.

3.7 Results

3.7.1 LAA shape descriptors

The values of the computed geometric parameters for each LAA are reported in Table 3.2.
Results showed a relevant variability in the LAA characteristics: for example, volume varied between 2.04 and 2.60 cm^3, length from 2.26 cm to 3.54 cm and tortuosity values are between 0.03 and 0.46. Comparing these quantities with a qualitative analysis of each LAA from Figure 3.4, we notice how the geometric indexes reflected the LAA morphological features.
Considering LAA4, we observed, from a purely qualitative point of view, that it presented a very simple geometry and a linear morphology. Indeed, looking at the computation of its geometric indexes, tortuosity was the lowest (0.03) with respect to the other LAAs. As expected, LAA3 showed the highest volume and surface area, as we can see from Figure 3.4. Moreover, LAA2 had

LAA	V (cm^3)	A_s (cm^2)	A_o (cm^2)	P_o (cm)	L (cm)	χ
1	2.04	8.94	1.86	4.98	3.54	0.46
2	2.57	9.25	2.13	5.65	2.26	0.05
3	2.60	10.10	1.87	5.06	2.80	0.08
4	2.21	9.11	1.62	4.90	2.52	0.03
5	2.12	8.31	1.15	3.88	2.36	0.26

Table 3.2: LAA geometrical parameters: V-volume; A_s-surface area; A_o-orifice area; P_o-orifice perimeter; L-length; χ-tortuosity

the lowest length despite the major values of LAA orifice perimeter and area. Finally, LAA1 presented the highest tortuosity and length even though its volume was small. Therefore, these results confirmed the high variability of the geometric characteristics of the LAA and it could be relevant quantifying their implications in the appendage fluid dynamics mainly during AF in order to evaluate their impact on the probability of thrombi formation.

3.7.2 Velocity analysis

The computed velocity from the CFD simulations for the five LAAs is depicted in Figure 3.5. Looking at the LAA1, we noticed that the blood flow started to enter into the auricle during the ventricular systole (first row) with velocity values between 7 and 9 cm/s. After the end of the ventricular systole the mitral valve opened (second row) and the blood flow exited from the LAA. Velocity was very low in this phase (2-3 cm/s) and these values could be associated with the morphology of the LAA1. Finally, looking at the end diastole phase (third row), blood flow continued to exit from the LAA1, reaching the maximum velocity (10 cm/s).
Regarding the LAA2, the shape of this auricle was different with respect to the LAA1 and these differences were reflected by the velocity analysis. These two LAAs had comparable surface areas, orifice perimeters and areas; however volume (V), length (L) and tortuosity (χ) were very different (26 %, 56.6 % and one order of magnitude variations, respectively) and their values helped to elucidate the differences in the hemodynamic parameters. Blood flow entered and came out with a higher velocity than LAA1 (range:15-20 cm/s) and a more copious quantity of the blood flow within the LAA2 was

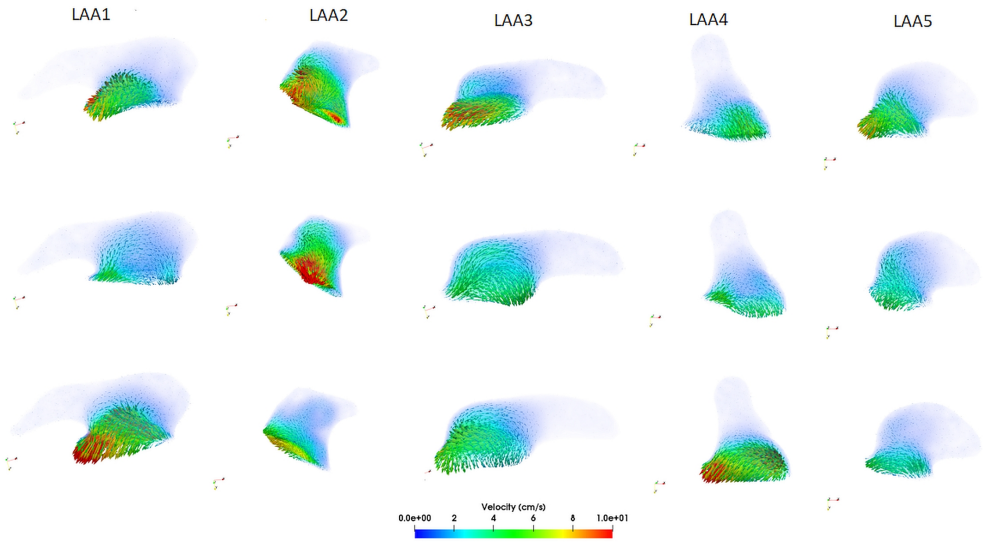

Figure 3.5: Computed velocity within each LAA during the ventricular systole (first row), at the beginning of the ventricular diastole (second row) and at the end of diastole (third row)

noticed. Having a volume higher than LAA1 and a less compexity and length, LAA2 held a great quantity of blood flow which reached also its distal part. Regarding the LAA3, we supposed that, giving its qualitative similarity with the LAA1, also the velocity characteristics should not expect great variability between these two auricles. However, changes in the velocity profile were observed and they could be related to the different geometric parameters with respect to the LAA1. LAA3 presented a higher length than LAA2 but less than LAA1 and χ was one order of magnitude less than LAA1 and double with respect to the LAA2. Therefore, blood flow entered (first row Figure 3.5) and exited (third row Figure 3.5) from this appendage with intermediate values between LAA1 and LAA2 (approximately 6-7 cm/s). Moreover, the different orientation with respect to LAA1 allowed the blood flow to get into the auricle more easily. These observations indicated that blood washout for LAAs geometries similar to the LAA3 was not strongly reduced; however it was limited by the complexity of this morphology and also by its non-linear geometry.
LAA4 was the most "linear" geometry. Indeed, looking at the Table 3.2, tortuosity was the smallest with respect to the other auricles. Therefore, we expected that this type of LAA would have a blood flow washout similar to the LAA2. However, even though its simple morphology, we noticed that blood flow, differently from the LAA2, did not reach, throughout the cardiac

cycle, the distal parts of this LAA. In order to better understand these findings, we studied the differences in the other geometric parameters. We found that LAA4 was characterized by a particular geometry: it presented a high orifice perimeter and, as we can see from Figure 3.4, shrinked towards its distal part. Indeed the volume was not very high (2.21 cm^3). This particular geometry allowed the blood to easily enter in the LAA, giving the large orifice, but it did not penetrate in the more shrinked part of the auricle and it was forced to exit with high velocities (approximately 10-12 cm/s, see third row of Figure 3.5).
LAA5 velocity values were much lower than the other appendages and they did not exceed 7 cm/s. LAA5 had the smallest values of A_o, V, A_s, P_o coupled with a high value of the tortuosity (0.26). These characteristics probably explain the difficulty of the blood flow to enter in this type of LAA because of its reduced orifice, despite its length was not very high (2.52 cm). Therefore, only a small quantity of the blood flow entered in LAA5 with low velocity, implying a reduced washout of this auricle comparable to LAA1 and LAA3 but much lower than LAA2.

3.7.3 Vortex structures analysis

Vortex structures in each LAA are reported in Figure 3.6. In general, the presence of vortex structures within the LAA may be indicative of a better blood flow washout, thus avoiding the risk of blood stasis. Our considerations focused on the velocity of each LAA were confirmed by the vorticity analysis.
LAA1 vortex structures in three different phases of the cardiac cycle are depicted in the first column of Figure 3.6. We noticed that most of the vortices were localized in proximity of the LAA orifice, where we found the highest velocity. After the MV opening (second row Figure 3.6), vortex structures were characterized by low velocities. Moreover, throughout the cardiac cycle, vortices did not reach the distal part of the LAA, thus implying a scarce blood washout in AF.
Different findings were observed on the LAA2. Indeed, given its simple morphology, vortex structures with higher velocity values than LAA1 occurred. Moreover, these vortices were not concentrated only in proximity to the LAA ostium and they reached all the anatomical parts of the LAA.
Results obtained on the LAA3 (third column, Figure 3.6) were similar to the LAA1. Indeed, vortex structures were localized near to the orifice. However, it seemed that these vortices got closer to the LAA tip, favouring a better blood flow washout with respect to the LAA1.

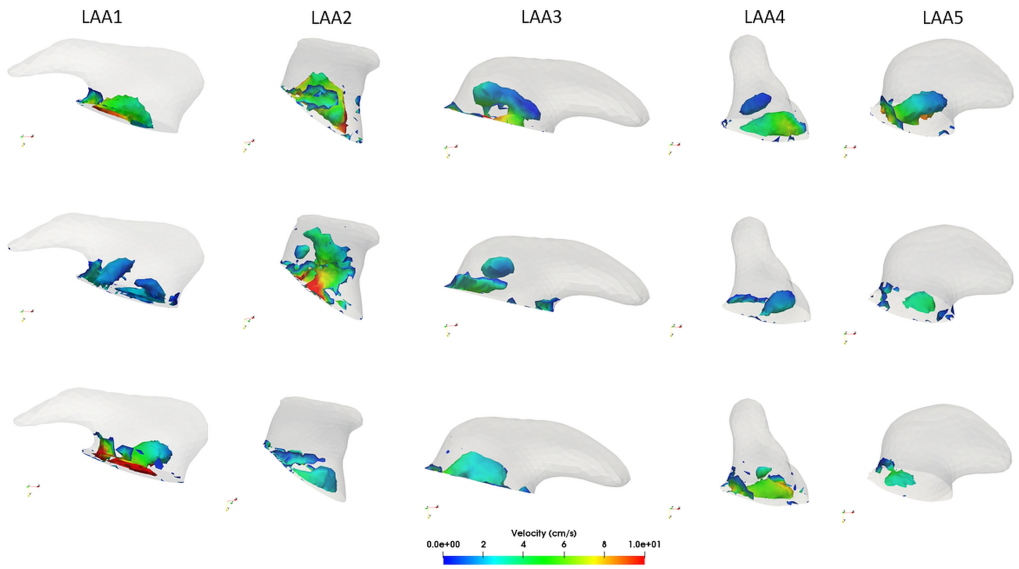

Figure 3.6: Computed vortex structures with the Q-criterion within each LAA during the ventricular systole (first row), at the beginning of the ventricular diastole (second row) and at the end of diastole (third row)

As discussed in the LAA4 velocity profile analysis, we expected that most of the vortex structures are localized in proximity of its orifice. Our hypothesis was confirmed, as shown in the fourth column of Figure 3.6. In all the phases of the cardiac cycle vortex structures remained near to the ostium with low velocities.
Looking at the LAA5, giving its low velocities throughout the cardiac cycle, also the number of vortex structures was scarce and characterized by small velocities. Moreover, as for the LAA4, they were localized most in proximity of the orifice.

3.7.4 Blood velocity at the LAA orifice

The profile of the LAA ostium velocity was evaluated and the results are reported in Figure 3.7. We considered the last cardiac cycle for each LAA and negative values of the velocity indicated a filling of the LAA, whereas positive values meant LAA emptying. As highlighted in Figure 3.7, all the auricles were characterized by low values of filling velocity (values between 0 and -5 cm/s). The most relevant result on this analysis was the evaluation of the emptying velocity since it could provide a measure of the washout.
We noticed an oscillatory trend in all the appendages and this was probably

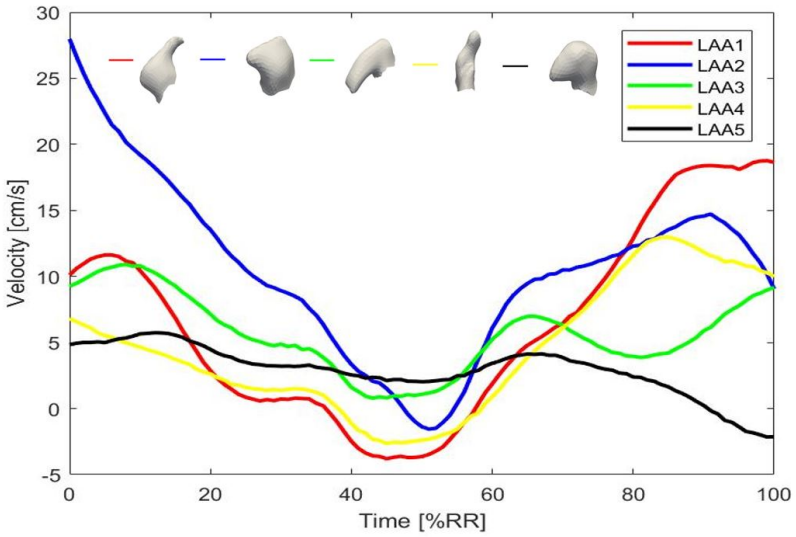

Figure 3.7: Computed velocity at the LAA ostia for the five LAAs.

due to the lack of the atrial contraction imposed in our simulation in order to represent AF condition, which implied a passive LAA emptying and filling. The lack of the contraction of the LA and of the LAA led the orifice velocity not to exceed, except for LAA2, the threshold of 20 cm/s. This data, in agreement with literature [79], implied a confined/circumscribed washout and consequently a possible increase of the thrombogenicity.
Looking at the LAA1, orifice velocity after an initial increase, decreased and reached the lowest value with respect to the other LAAs. This phase was followed by a new increase characterized by a velocity peak of 18.8 cm/s, which was closed to the threshold and could indicate a good washout. However, in the earlier stage the filling occurred with high velocity (absolute value approximately 5 cm/s) and this meant that part of blood flow could remain in part within the LAA.
LAA2 peak velocity was approximately 29 cm/s. Therefore, this evaluation confirmed that within the LAA2 geometry blood flow entered and exited with higher velocity and reached also the tip of the auricle, providing a significant washout.
Regarding LAA3 and LAA4, their peak orifice velocity were 10.9 cm/s and 13 cm/s, respectively.
LAA5 ostium velocity strengthened our previous findings, indeed it showed a peak value at the ostium of approximately 6 cm/s.

3.7.5 LAA blood stasis quantification

In order to quantify blood stasis in the LAA, we performed a specific study. Each LAA was populated by 500 fluid particles at the beginning of the CFD simulation. The fluid particles were distributed as a sphere around the center c, which represents the midpoint of the LAA centerline. As described in Section 2.5.2, the results of the first three cycles were disregarded to avoid the influence of the unphysiological initial condition on the blood flow. Therefore, we considered only the last five simulated cycles for each simulation.
Then, we evaluated how many fluid particles remained within the LAA at the end of the third, fourth and fifth cardiac cycle. The number of residual particles at different timesteps of the cardiac cycle could provide a direct measure of LAA blood stasis: more particles remain in the LAA, higher is the probability of the clot formation within the LAA. Results of this computation are reported in Table 3.3.

Cardiac Cycle	LAA1	LAA2	LAA3	LAA4	LAA5
0	500	500	500	500	500
3	204	186	266	437	310
4	182	124	133	379	178
5	168	58	103	312	126

Table 3.3: Number of fluid particles which remained in the LAA at the end of the third, fourth and last cardiac cycle for the five LAAs in AF. Cardiac cycle = 0 indicates the beginning of the simulation.

At the end of the fifth cardiac cycle, 33.6 % of fluid particles remained in the LAA1. LAA2 results showed important differences with respect to the LAA1: only the 11.6 % of the fluid particles remained within the auricle. LAA3, as expected, presented a better washout with respect to the LAA1. Indeed, 20.6 % of fluid particles did not exit from the LAA. Despite their similarity in shape, the difference between LAA1 and LAA3 could be caused by the opposite orientation and the different value of tortuosity. 62.4 % of fluid particles remained within the LAA4 because the blood flow pushed the particles to the tip and velocities in this part were very low. The blood washout of the LAA5 was not strongly reduced: 25.2 % of particles remained within the appendage.

3.8 Discussion

In this study, we assessed the influence of the LAA morphology on the LA hemodynamics. The framework developed and described in this study is fully automatic and fast. In our experience this procedure is very robust since it worked correctly for all our data; it requires less than 1 minute to generate one model and most of this time is required to import the mesh and compute the shape diameter function. Several geomeric parameters were computed and correlated with blood velocities, vorticity, LAA ostium velocity and residence time for each anatomical model.
We found that the LAA geometric characteristics impact on the hemodyamic pattern within the LAA highlighting that not only the appendage morphology types should be considered for the stroke risk assessment in patients affected by AF [3]. Our results on the velocity and vorticity within the LAA, LAA orifice velocity and on the residence time demonstrated and confirmed that not only complex LAA morphologies were characterized by low velocities, low vorticity and consequently a higher thrombogenic risk. Simple morphologies can have a thrombogenic risk equal, or even higher, than more complex auricles and their geometric features could play a key role in defining thromboembolic risk. Indeed, in our opinion, LAA geometric parameters should be considered, coupled with the morphological characteristics, for a comprehensive evaluation of the blood stasis and stroke risk. These geometric characteristics were not investigated in the previous works, neither correlated with hemodynamic parameters.
LAA1 presented the highest length (3.54 cm) and tortuosity (0.46), thus representing a complex shape. Indeed, the quantity of the blood flow which reached the distal part of the LAA1 throughout the cardiac cycle was strongly reduced due to the complex morphology of this LAA, as explained in Section 3.7.2. Moreover, vortex structures within this appendage were limited in number and did not reach its distal part.
Since Beigel et al. [79], observed that the stroke risk is 2.6 fold higher in AF patients in which the velocity at the ostium throughout the cardiac cycle is less than 20 cm/s and these findings were confirmed in the CFD studies on the LAA in AF by [19, 80], we also evaluated the LAA orifice velocity. LAA1 ostium velocity was lower than 20 cm/s, indicating a high thrombogenicity. LAA1 blood stasis quantification confirmed this result, showing 33.6 % of fluid particles remained within the LAA1. Fluid particles were pushed towards the appendage tip and the low blood flow velocity hampered an effective washout. Therefore, we expect that LAA geometries similar to LAA1 may have an high thromembolic risk.
Study of LAA2 fluid dynamics indicators proved that linear structures, cou-

pled with a small length, had a better washout, thus implying a reduction of the blood stasis and thrombi formation risk. Moreover, the positioning of the LAA2 could have a key role for the stroke risk assessment. As highlighted in Figure 3.4, LAA1 had an opposite positioning with respect to the others. This characteristic could explain the scarce washout, mainly in the distal part, thus increasing the probability of thrombi formation risk. The LAA2 blood stasis analysis confirmed this consideration: indeed the simple geometry allowed and helped the blood flow to reach the tip of the LAA and therefore to fill the appendage volume. We concluded that the probability of clot formation for the auricles which present a morphology similar to the LAA2 is low.
LAA3, despite its qualitative similarity with the LAA1, presented relevant differences in the hemodynamic parameters. Velocities were slightly higher than LAA1 and blood flow entered within this auricle more easily and consequently vortex structures were deeper. Moreover, looking at the number of fluid particles which remained in the LAA3 at the end of the fifth cardiac cycle, we found that LAA3 had a better washout than LAA1. Hemodynamic differences between these two auricles could be related to the different orientation and tortuosity, as explained in section 3.7.2. Therefore, the thrombogenicity risk of this type of LAA could be classified as medium.
LAA4 velocity profile highlighted that for the assessment of left atrial appendage thrombogenicity, geometric and morphological features should be taken into account. Indeed, as reported in the velocity field analysis, even qualitatively simple LAAs (i.e. LAA4) could show a high probability of blood stasis and therefore thrombi formation. LAA4 vortex structures were localized in proximity of its orifice implying that blood washout in the distal parts of this auricle was scarce, thus increasing the probability of clot formation with respect to the other LAAs. Yet, we found low velocity values at the ostium in the LAA3 and LAA4, thus indicating a moderate clot formation risk for this particular LAA shape. In order to confirm our previous findings, we quantified the LAA4 blood stasis. The fluid did not reach the auricle tip because of the shrinking towards the distal part. These characteristics led to a scarce washout of the LAA4 (see Table 3.3), moreover the vortex structures were absent, thus implying a blood stasis in proximity of the LAA4 tip. This result was very relevant because it proved that the LAA4 showed the highest probability of blood stasis and consequently of thrombi formation with respect to the other appendages, despite its simple and linear geometry, where a low thrombogenicity was expected.
Regarding the LAA5, velocity within the auricle and at the orifice showed low values that could imply a relevant risk of blood stasis and thrombi formation. Also, vortex structures were localized only in proximity of the LAA orifice.

However, even though the velocities and the number of vortex structures were very small, the blood washout of the LAA5 was not strongly reduced. LAA5 limited extension could compensate the high tortuosity, allowing the blood flow to entirely cover its volume, thus providing a good washout.
The few CFD studies available on this topic [20,80–82] focused on the correlation between the four type of the LAA morphologies proposed by Di Biase [3] and the thrombogenicity. However, they did not analyze other characteristics of the auricles that might have a crucial role in pathological conditions.
With respect to the other works, we designed and developed a procedure which allowed to consider the same LA shape for each LAA. To perform this task, the SDF was employed. Most of previous segmentation approaches were based on local surface properties, such as curvature or geodesic distance, that often depend on the topology and on the pose of the object. SDF overcame these problems and provided a link between the surface mesh and the object's volume, thus allowing the extraction a specific part of the mesh. We chose this option because the variability of the left atrial chamber could affect the validity of the hemodynamics changes when different types of LAA were compared, since these variations could be caused also by the LA geometric features (dimensions, structure and pulmonary vein connections and morphology).
Obviously the clinical problem we are facing is very complex and we think there may be an interchangeable conditioning effect between the LA and the LAA shapes and both effects should be considered. However we also think the comprehension of each single effect may help in clarifying the interplay between them. In this study we focused on better understanding the influence of each specific LAA shape on blood hemodynamics and, to this aim, we were forced to eliminate the dependence from the LA shape and from other patient-specific factors. Our results, based on a simplification of the real phenomenon, showed that the complexity of the LAA shape alone does not correlate with clot formation and additional parameters should be considered for a clear comprehension of the link between LAA shape and the risk of stroke.
Our approach can be further improved because a limitation consists in the AF motion model simulation. The results of this study could benefit from the application of a patient-specific motion field of the LA in AF. Unfortunately, up to date, quantification of such a motion field is not possible using the standard 3D acquisition, MRI or CT. Since AF is described by a disorganized and reduced motion of the LA, in this study we applied a random displacement field with small amplitudes in order to avoid mesh degeneration during simulations. Once the patient-specific motion in AF has become available, our pipeline would strongly benefit from such information.

To conclude, the presented framework might represent a step towards the development of a better tool for the patient-specific cardioembolic risk assessment and preventive treatment in AF patients.

3.9 Simulation of the LAA occlusion and its haemodynamics implications on the LA

As reported in Section 3.1, to reduce the thromboembolic risk different strategies have been developed with respect only to the oral anticoagulation therapy, i.e. LAA percutaneous closure. The implant of the LAA occlusor device seems to better reduce the risk of thromboembolism compared to warfarin anticoagulation therapy [16]. Indeed, recent trials have shown that left atrial appendage occlusion (LAAO) is effective and not inferior to oral therapy in stroke prevention [83–85]. A large recent European registry reported a high rate of implantation success (98%), with an acceptable procedure-related complication rate of 4% at 30 days [86]. However, an adequately powered controlled trials are urgently needed to inform the best use of these devices, including LAA occluders in patients who are truly unsuitable for oral anticoagulants (OAC) or in patients who suffer a stroke on OAC, randomized comparisons of LAA occluders with new OACs (NOACs), and assessment of the minimal antiplatelet therapy acceptable after LAA occlusion.
The most used LAA occlusor devices used in the clinical practice and also studied in literature are two: the Amulet ^{TM}device (Abbott, North Chicago, Illinois) and the Watchman device ^{TM}(Boston Scientific, Maple Grove, MN.) In Figure 3.8 we show the design of these two devices.

Figure 3.8: LAA occlusion devices: in the left panel the Amulet^{TM}device, in the right panel the Watchman^{TM}device.

Since the device implant might be associated with major adverse events, so the utmost attention must be paid while balancing benefits and risks linked to this procedure [87]. Indeed, the implantation procedure can cause serious complications, with event rates reported in analyses from insurance databases and systematic reviews, possibly identifying a certain degree of reporting bias [88,89]. Indeed, altough the mortality rate is around 3 % considering a mean of all the studies presented in literature on this topic, other adverse events can occur. Pericardial effusion and also stroke or transient ischemic attack after the implantation procedure were observed. Early experience with the Watchman device revealed a total of 3.8% of serious pericardial effusions. The incidence of periprocedural pericardial effusions was only 1.9% with the Amulet device [6]. Moreover, bleeding around the device, device embolism and, most important, device motion and dislocation have been detected. Therefore, the LAA percutaneous closure is a not trivial procedure that requires a certain level of expertise and training in order to successfully complete the procedure without complications. This because the anatomical variability of the LAA plays a key role in the choice of the correct LAA occlusion device and in the correct positioning of it with respect to the LAA ostium during the implant. Therefore, biomedical images are acquired to have good anatomical knowledge of the cavity, before and during the intervention. In most clinical centers X-ray and transesophageal echocardiography (TEE) images are used to characterize the LAA morphology during the intervention to support decisions on device implantation. The LAA ostium dimensions and height/depth of the LAA cavity are critical LAA shape parameters to individualize the size of the implanted device and the landing zone (location where the device will be released). For this reason, LAA shape parameters are usually estimated from medical images with manual tools, being difficult to standardize criteria to objectively define them. Moreover, values of these parameters coming from different imaging modalities differ substantially due to their respective spatial resolution and limitations. Indeed, for example, the most imaging technique used in the clinical practice for performing an haemodynamics analysis is based on echocardiographic images, i.e. TEE. However TEE only report a single blood flow velocity value in one point in space (LAA ostium) and in time (end diastole), which constitutes an over-simplification of the complex hemodynamics in the LA and LAA. In this scenario, the CFD could have a key role in providing a helpful in silico simulations of the blood flow patterns within the LAA and the LA in a patient-specific approach in order to estimate in a non-invasive way physically significant hemodynamic parameters in a complex fluid dynamics system. As of today, few studies are focused on the hemodynamic changes in LA pre- and post-LAAO [90, 91]. Yet, the hemodynamic effects depending on the closure morphology at the

ostium have not been investigated. Moreover, in previous works, AF motion condition has been replaced with rigid LA walls, introducing a considerable simplification. The aim of this study was to simulate the fluid dynamics effects of the LAAO in AF patients to predict patient-specific hemodynamic changes caused by the LAAO, by applying the two most popular and used devices (Amulet^{TM}, Abbott; Watchman^{TM}, Boston Scientific). To this purpose, LAAO was reproduced on 3D LA anatomical models obtained from real clinical data of five AF patients. For each patient, CFD simulations in AF condition were performed on the entire atrium model and on the models with the two LAAO. Significant fluid dynamics indices were determined to evaluate the changes in the flow patterns after the occlusion in relation to the thrombogenic risk.

3.9.1 Methods

The initial dataset consisted of five 3D anatomical models of the LA, extracted from five AF patients CT images. In Figure 3.9 we show the five 3D LA anatomical model used in this work.
As a first step to generate models with LAAO, we removed LAA from the anatomical models. To this purpose, we applied the same procedure described in detail in Section 3.4. The shape diameter function (SDF) was employed. The iso-contours of the SDF map on the LA meshes allowed a threshold-based segmentation in anatomical regions with similar SDF values, identifying pulmonary veins (PVs), atrial chamber and LAA. Based on the anatomical position of the LAA, the algorithm was then able to detect the LAA and to remove it.
After removing the LAA, we simulated the occlusion by generating a surface at the orifice. The closing surfaces were created by using MeshLab [45]. The main geometric features of the devices as well as their fitting in the shape of the LAA ostium were considered (see Figure 3.8). The Amulet^{TM}nitinol disc sealing the LAA orifice was emulated with a flat planar closure. The screened Poisson surface reconstruction algorithm was instead used to reproduce the umbrella-shaped structure of the Watchman^{TM}device in order to model also the convexity structure of this particular LAA occlusion device.
For each patient, we obtained a final set of three LA anatomical models: (1) the original model with LAA; (2) the LAAO model with Amulet^{TM}; (3) the LAAO model with Watchman^{TM}. In Figure 3.10 we show as an example the result of the aforementioned procedure on the first two patients LA 3D anatomical models.
The CFD model used for the simulation of the haemodynamics of each

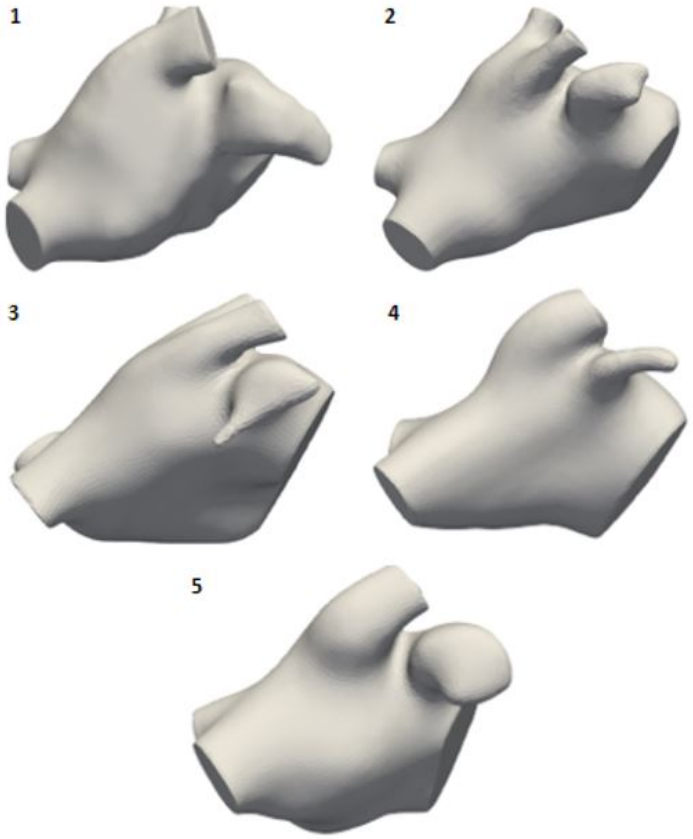

Figure 3.9: LA 3D anatomical models of the five patients enrolled in the study.

anatomical model was the one described in detail in Section 2.4. Regarding the imposition of the boundary conditions and the setup of the numerical simulation, we used the same approach described in Sections 3.6 and 3.6.1. To assess the blood haemodynamics in these different conditions, we evaluated the LA velocity field and the vortex structures, LAA orifice velocity and the residence time within the atrial chamber.

3.9.2 Results and Discussion

Figure 3.11 shows the computed velocity field inside the atrial chamber for the first patient models. We compared the CFD simulations of the two LAAOs with the complete LA with the LAA.
For the simulation of the LA with the LAA we saw in correspondence of the

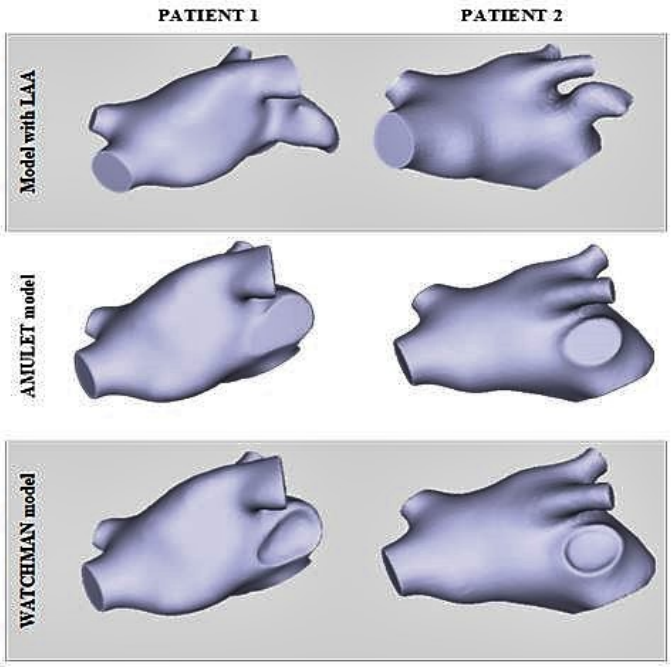

Figure 3.10: LA models with the LAA (upper panels) and after LAAO with Amulet^{TM}and Watchman^{TM}devices (mid and bottom panels).

ventricular diastole that the velocity at the MV reached the value of 60 cm/s. Also at the PVs velocities reached the values between 30 and 40 cm/s. Regarding the LAA, vectors showed low amplitude with the direction towards the LAA tip.
For the LAAO simulations, we noticed that velocities at the PVs were slightly lower with respect to the model with the LAA (around 20 cm/s). However, at the MV we observed higher values of the velocities with a peak of 69 cm/s for the Amulet occlusion and 72 cm/s for the Watchman occlusion with respect to the simulation with the LAA. Also, in these simulations the direction of all the vectors seemed to converge towards the MV and the distal parts of the atrial chamber were reached slowly. For this reason the gradient of the velocity between the MV and atrial chamber was higher in the LAAO simulations with respect to the model with the LAA. Yet, it seemed that in the LAAO simulation with the Watchman device, the blood flow was less organized with respect to the LAAO with the Amulet, probably due to its concave shape that causes variations in the fluid streamlines direction.

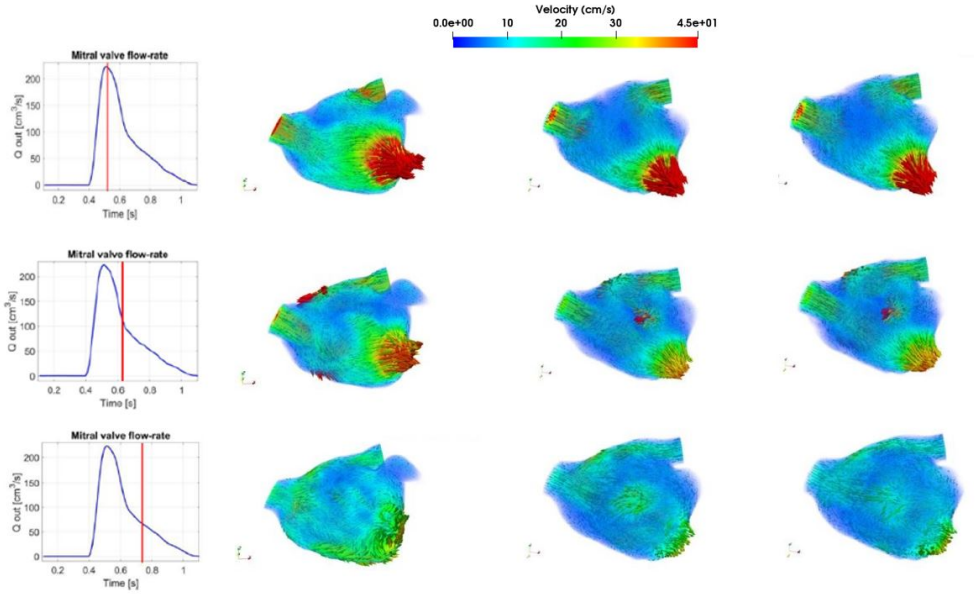

Figure 3.11: First patient LA blood flow velocity in the model with the LAA (first column) in the model with the LAAO Amulet device (second column) and in the model with the LAAO Watchman device (third column). First row referred to the beginning of ventricular diastole, second row to the late ventricular diastole and the third row to the atrial sistole.

During late diastole, in the simulation with the LAA velocity at the PVs and MV decreased and two peaks of the velocity of 55 cm/s were observed on the atrial roof and near to the atrial septum. For the LAAO simulations we observed that the peak of the velocity up to 64 cm/s was detected near to the LAA ostium with direction to the atrial septum. In this phase the blood flow that was coming from the PVs moved towards the LAA ostium and collided with the occlusion plane. Therefore, the blood flow was constrained to go to the opposite direction with high velocities. Also in the LAAO simulations we observed a peak of the velocity on the atrial roof with lower velocity (30-35 cm/s) with respect to the model with the LAA.
During the atrial systole, that was strongly reduced by the presence of AF, we observed a not organized blood flow pattern in correspondence of the MV in the simulation of the complete LA. Indeed, despite the values of the velocity (25-30 cm/s), directions of the vectors were discordant between each other and seemed to create a sort of spirals thus causing also a little backflow at the MV. Regarding the LAA, velocities remained very low (7-8 cm/s) and we did not observe velocity vectors that exited through the LAA ostium towards the atrial chamber probably due to the AF condition and the absence

of LAA motion. Therefore the risk of blood stagnation in the LAA could be considered high.
However, in the LAAO simulations we observed higher values of the velocity at the PVs and mainly in the center of the atrial chamber with values of 20-30 cm/s. This peak was completely absent in the model with the LAA and it was probably due to the collision of the blood flow with the LAA occlusion plane during the late ventricular diastole which caused an higher blood flow towards the atrial septum.
Comparing the Watchman and Amulet occlusions, the peak in the center of the atrial chamber was higher for the Amulet occlusion with respect to the other one, however the velocities within the LA were distributed with higher values in all its parts in the Watchman simulation with respect to the Amulet. Moreover in this phase, we observed a more ordered blood flow expecially at the MV where most of the vectors were oriented towards the MV with the same direction. In all these three phases of the cardiac cycle we concluded that the velocity at the LAA ostium was higher in the models with the occlusion with respect to the model with the LAA.
These findings were confirmed for all the patients enrolled for this study.
As an example we observed in Figure 3.12 the LA velocity of the second patient in all the three performed simulations. In patient 2 models, more similar blow flow patterns were identified in pre- and post-LAAO cases. In the entire atrium model, the LAA was poorly involved in the blood washout, as suggested by the near-zero speeds. As for the first patient, the removal of LAA produced a slight reduction in speed at PVs and at LA inferior-septal wall. Flow to the mitral valve reached comparable rates in the three models (50 cm/s in both LAAO models; 46 cm/s in model with LAA). During atrial systole, a difference in blood flow pattern was noticeable (see Figure 3.12). Indeed, in pre-occlusion LA, an isolated backward oriented peak of velocity (46 cm/s) was detected under the left PVs, while in the center of the atrial chamber velocities were much lower. On the contrary, in both LAAO models, a larger distributed peak is observed in the center of the atrial chamber, suggesting an improved washout.
Also in this patient we observed higher values of the velocities in the center of the atrial chamber with values of 20-30 cm/s for the LAAO simulations. This peak was completely absent in the model with the LAA and it was probably due to the collision of the blood flow with the LAA orifice during the late ventricular diastole which caused an higher blood flow towards the atrial septum.
Moreover, velocities in the LAA were very low throughout the cardiac cycle in the complete atrial model showing higher values in the LAAO simulations.
We also evaluted the vortex structures by computing the Q-criterion. Figures

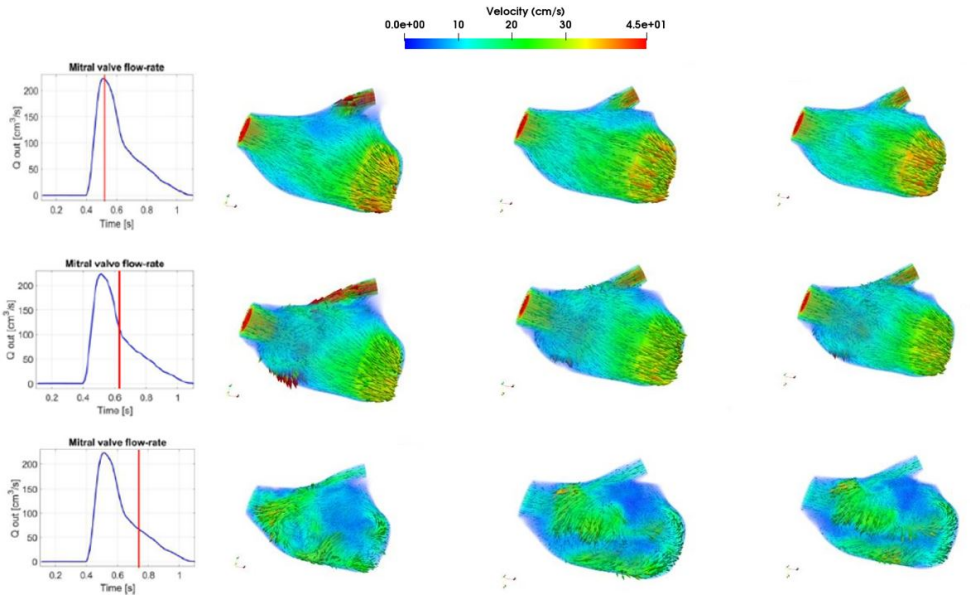

Figure 3.12: Second patient LA blood flow velocity in the model with the LAA (first column) in the model with the LAAO Amulet device (second column) and in the model with the LAAO Watchman device (third column). First row referred to the beginning of ventricular diastole, second row to the late ventricular diastole and the third row to the atrial sistole.

3.13 and 3.14 showed the result of the first and second patient, respectively. We observed that during the ventricular diastole the model with the LAA had a higher number of vortex structures with respect to the LAAO models with higher velocity mainly at the PVs and the MV.
In both patients, vortex structures were almost absent within the LAA and mostly in its apical part throughout the entire cardiac cycle, thus revealing an inadequate blood washout of the zone. For patient 1, after the closure, vortices were less numerous in LA, but bigger in size. Higher velocity vortices were located at MV. In the LAAO models, vortex structures were more localized in the centre of the chamber. The model with the Watchman showed a slightly higher number of vortices than the Amulet expecially during the atrial systole.
For the second patient (see Figure 3.14) after the LAAO, more vortices were found near the LAA ostium in both the two occlusion models during the late ventricular diastole and atrial systole with respect to the model with the LAA. The same behaviour was observed also in the patient 1 simulations. This could promote a better washout of the blood flow near to the LAA orifice after the occlusion; moreover also in the second patient the number

of vortex structures were higher in the model with the Watchman occlusion with respect to the Amulet occlusion.
Generally, vortex structures minimally decreased in number in the LA after the occlusion but they increased their size. Therefore, this characteristic could favor a better washout of a larger quantity of the blood flow with respect to the complete model of the atrium with the LAA. We noticed some differences in vortices localization and speed distribution, with lower velocity at PVs in ventricular diastole but higher velocity near the MV during atrial systole.
These findings were confirmed, as for the velocity field analysis, also for the other three patients enrolled in the study.
The most important haemodynamics parameter that was involved in this study was the LAA orifice velocity. To evaluate it, we isolated the LAA ostium surface and we computed the module of the average velocity for each patient for all the performed simulations. Results are shown in Figure 3.15 for all the five patients.
Studies in literature [79] have shown that speeds below 40 cm/s in LA are associated with a higher risk of stroke, while speeds below 20 cm/s are associated with the identification of thrombus. By analyzing the first patient, we observed that in the model with the LAA, velocity values at the ostium fluctuated between 8 cm/s and 19 cm/s throughout the cardiac cycle. For this reason, these values were below the threshold of 20 cm/s thus highlighting a potential thrombogenic spot. This behaviour was probably due to the lack of the LAA contraction due to the AF. Vice versa, in both LAAO models much increased average velocity was registered (13.0 cm/s model with LAA; 25.2 cm/s Amulet; 31.1 cm/s Watchman), with peaks over 50 cm/s, suggesting a reduced stroke risk.
The effects of LAAO in LAA ostium velocity were similar in patient 2. In the model with the LAA, values ranged from 6 cm/s to 15 cm/s. In LAAO models, average velocity doubled (10.2 cm/s model with LAA; 21.1 cm/s Amulet; 22.6 cm/s Watchman). In both patients, the Watchman model showed higher average speed. By looking at all patients data, we observed that the peak values seemed to be higher for all the patients in the model with Watchamn device LAAO thus implying a better washout near the LAA orifice with this type of occlusion. LAA orifice velocity showed much higher values for LAAO simulations with respect to the relative models with the LAA with a mean value LAA orifice velocity higher in the Watchman device simulation with respect to the Amulet device simulation. Moreover, in both LAAO simulations we observed the presence of two peaks of the velocity where the second one was higher with respect to the first one expecially in the model with the Watchman device, thus indicating a better washout of the LA part near to

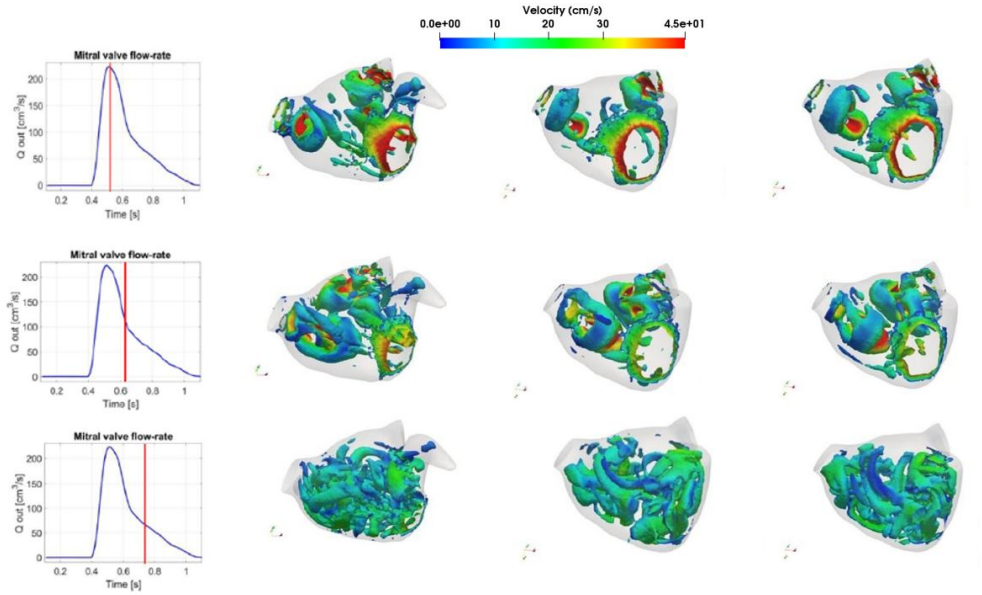

Figure 3.13: First patient LA vortex structures in the model with the LAA (first column) in the model with the LAAO Amulet device (second column) and in the model with the LAAO Watchman device (third column). First row referred to the beginning of ventricular diastole, second row to the late ventricular diastole and the third row to the atrial sistole.

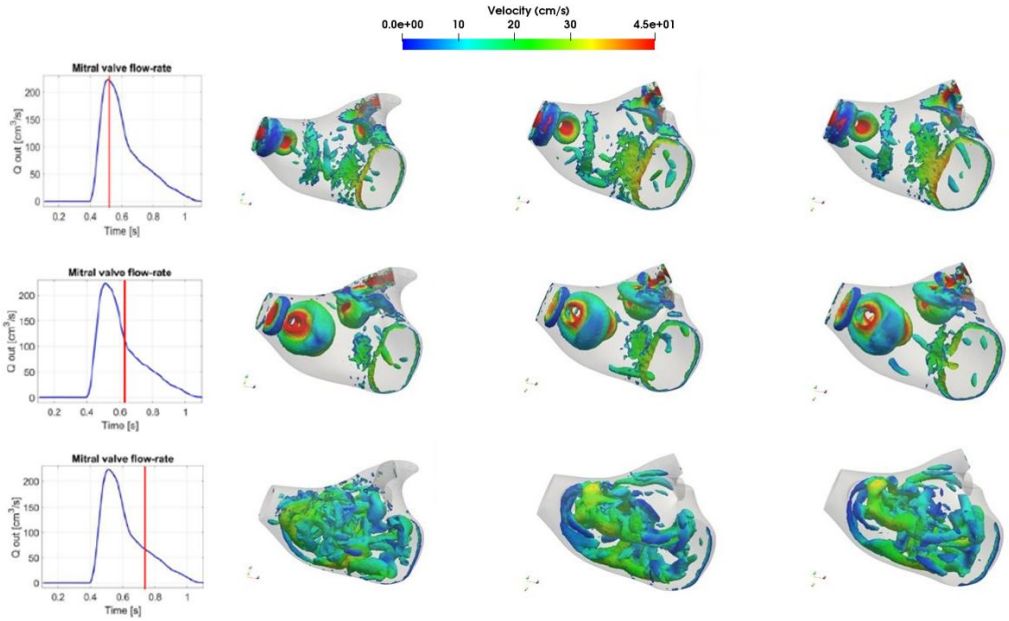

Figure 3.14: Second patient LA vortex structures in the model with the LAA (first column) in the model with the LAAO Amulet device (second column) and in the model with the LAAO Watchman device (third column). First row referred to the beginning of ventricular diastole, second row to the late ventricular diastole and the third row to the atrial sistole.

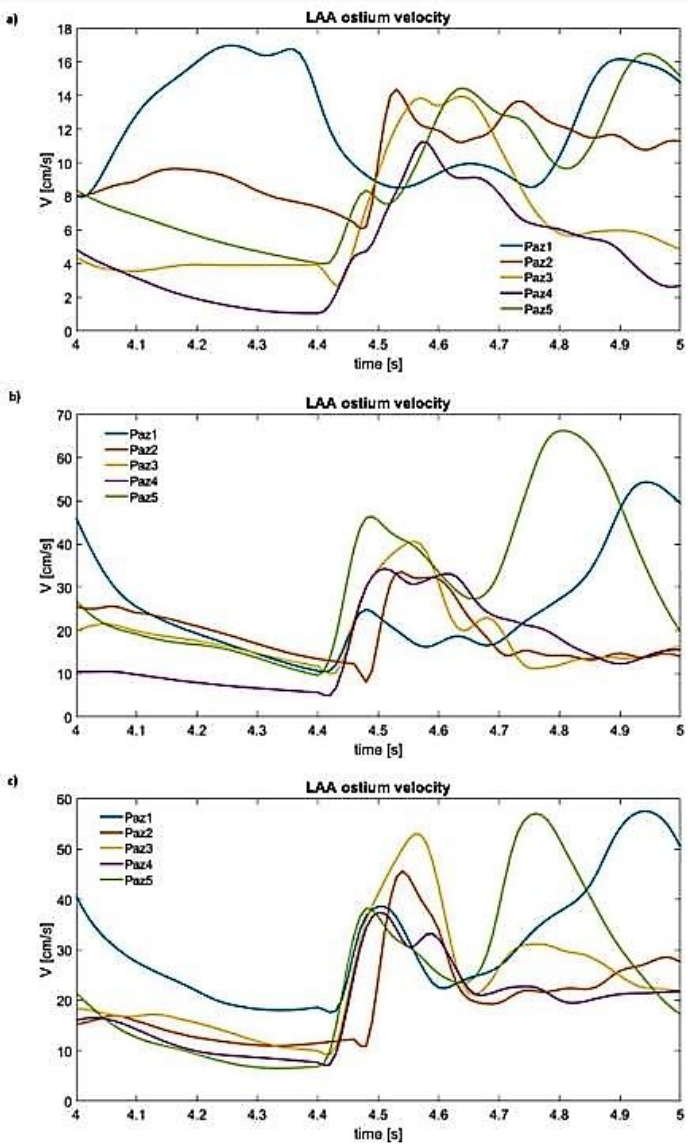

Figure 3.15: LAA orifice velocity for all the five patients. Panel a) refers to the LA model with the LAA, panel b) to the LAAO model with the Watchman device and panel c) to the LAAO model with the Amulet device.

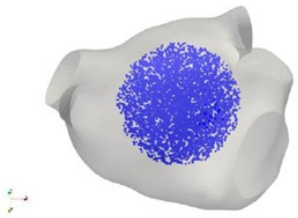

Figure 3.16: LA fluid particles distribution within the first patient atrial chamber (Amulet simulation) at the beginning of the simulation.

the orifice.
To have a better understanding of the blood washout within the atrial chamber we performed an additional study focused on the evaluation of the fluid particles in all the simulated cardiac cycles for each simulation. In particular, we populated the LA with 5000 particles at the beginning of the simulation. As an example, in Figure 3.16 the fluid particles distribution at the beginning of Amulet occlusion simulation for the first patient. Then, the number of particles which remained within the LA at the end of the fifth cardiac cycle was computed. The higher was the number of residual particles, the greater was the probability of blood stagnation. The analysis was performed for all the five patients enrolled in the study and results are reported in Table 3.4 for the complete atrial chamber simulations, in Table 3.5 for the Watchman LAAO simulations and in Table 3.6 for the Amulet LAAO simulations.

From the results reported in the Tables, we clearly observed that the simulations with the LAAO devices showed a better washout of the atrial chamber confirming the previous findings regarding the velocity field, vorticity and LAA orifice velocity. Indeed, in the LAAO simulations the blood flow resulted more ordered with higher velocities in all the atrial parts and this clearly explained why the number of particles within the LA after five cardiac cycles were lower in these simulations. In all patients, a more effective atrial washout in the Watchman configuration was confirmed because in this case the number of the remained fluid particles was the lowest with respect to the other simulations.

To conclude, in this study a workflow for simulating the fluid dynamics effects of LAAO in AF was tested. The study could contribute to understand the fluid dynamics conditions leading to thrombogenesis and to identify the most effective devices in reducing the stroke risk for patient-specific mor-

CC	P1	P2	P3	P4	P5
start 1 CC	5000	5000	5000	5000	5000
end 5 CC	285	205	157	214	243

Table 3.4: LA fluid particles computation after 5 cardiac cycles (CC) for the complete atrial chamber models of the 5 patients. P states for Patient.

CC	P1	P2	P3	P4	P5
start 1 CC	5000	5000	5000	5000	5000
end 5 CC	183	124	86	146	139

Table 3.5: LA fluid particles computation after 5 cardiac cycles (CC) for the LAAO Watchman simulations of the 5 patients. P states for Patient.

CC	P1	P2	P3	P4	P5
start 1 CC	5000	5000	5000	5000	5000
end 5 CC	205	134	97	154	164

Table 3.6: LA fluid particles computation after 5 cardiac cycles (CC) for the LAAO Amulet simulations of the 5 patients. P states for Patient.

phologies of LA. Our results suggested a more effective blood washout after LAAO and, consequently, a lower risk of blood clot formation. Also, a slightly improved washout effect is revealed when the Watchman device is implanted. These findings were also confirmed and in afford with the studies of [90, 91] where the LA fluid-dynamics pre and post LAA occlusion was studied. Indeed, they also found a higher LAA orifice velocity and a more organized blood flow within the LA expecially near to the MV after the LAA occlusion.
Obviously, a limitation of this study was the simulation of the LAA occlusion without having the specific 3D model of the device that could better clarify the impact of the occlusion in the atrial chamber.

Chapter 4

The FATA study

The purpose of this study was to test and validate the CFD model designed and developed in this Thesis on different clinical scenarios. To this aim, we computed the haemodynamics in patients with and without AF and in patients with different pathophysiological conditions in order to enhance the differences in the computed fluid-dynamics indexes. Moreover, we tried to find the most important parameters from the CFD model that potentially stratify the stroke risk on a patient-specific basis.
The study was performed in collaboration between the University of Bologna, BIOMIG laboratory and the department of Cardiology and Radiology of "AUSL della Romagna, Ospedale Santa Maria delle Croci, Ravenna". The "FATA" (**F**luid-dynamics in the left **A**trium in atrial fibrillation patients and in controls for **T**hrombogenic risk **A**nalysis) was approved by the C.E.ROM. Comitato Etico della Romagna (Prot. 1276/2019 I.5/6, Reg. Sperimentazioni n. 2323). The design and the follow-up of the study respected all the regulations and provisions of the Italian laws (in particular, Decreto Legislativo n.211, 2003). Moreover it operated in compliance with the Helsinki Declaration and with the norms of the Good Clinical Practice (GCP-ICP), ISO 14155.

4.1 Methods

The workflow of the study is depicted in Figure 4.1.

Our personalization pipeline involved using dynamic CT imaging to reconstruct the moving patient-specific 3D atrial anatomy over the cardiac cy-

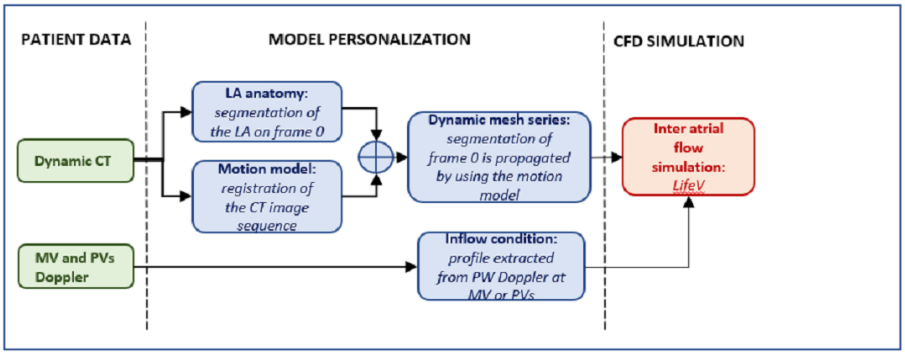

Figure 4.1: Flowchart of the FATA study: patient-specific data (light blue boxes) processed to derive the LA anatomical and deformation model (light blue boxes) are the inputs for the final personalized CFD model (red box).

cle. In particular, 10 frames per cardiac cycle for each patient were acquired. Clinical cases data were divided in three groups:

1. CT data patients not affected by AF and without heart diseases or pathologies. We defined these patients CT data as control group.

2. CT data patients affected by paroxysmal AF.

3. CT data patients affected by persistent AF.

The complete study involves the analysis of 25 patients from the first group (control) and other 25 patients from the second and third group (paroxysmal AF and persistent AF). In this thesis we show the results of 10 patients enrolled until now. These 10 patients belonged to the control group (3 patients), paroxysmal AF group (4 patients) and the persistent AF group (3 patients). CT data of these patients will be also acquired after one year for the follow up of the study, expecially for the AF patients in order to observe the evolution of the pathology.
All subjects gave written informed consent in accordance with the Declaration of Helsinki and the guidelines estabilished by the Ethics Commitee C.E. ROM. Each one of the subject can modify his/her will everytime. Obviously, each patient was anonymized and an internal code was generated in order to associate his/her clinical data (age, ECG pre-acquisition, pathological history, duration of AF episodes if present, geometrical measurements of the LA and LAA and pharmacological therapy if present) to each patient. This information is available only for Ravenna Hospital investigators. Following

the study protocol, Doppler data were acquired at the MV and PVs. Unfortunately, only in one patient that belonged to the control group, the MV Doppler was available; in the other 9 patients presented in this thesis Doppler data were not acquired.
Processed patient data was then provided as input to the CFD solver. If applicable, a patient-specific MV or PVs flowrates from intracardiac pulsed wave Doppler were used to set boundary conditions for the CFD simulations. For the definition of the patient-specific LA motion and anatomical model we applied the same methods and procedures described in detail in Sections 2.2 and 2.3. In this way we were able to reconstruct the patient-specific LA geometry and its deformation model throughout the cardiac cycle for control group and AF patients.
The CFD model developed in this thesis for the LA haemodynamics simulations for all the patients enrolled in the FATA study (see Section 2.4 for all the details about the definition of the model) was employed.

The only difference with respect to the study described in Chapter 2 was about the definition of the boundary conditions. The MV flowrate profile reported in Figure 2.11 was used for the paroxysmal and persistent AF patients simulations. However, this flowrate was not suitable for the patients that belonged to the control group because in this case the amplitude of the A wave (that corresponds to the atrial systole) was not compromised by the AF condition and shows a higher amplitude. For one patient analyzed from the control group, a MV Doppler velocity measurement was acquired and we were able to estimate the patient-specific MV flowrate by multiplying the MV Doppler velocity for the MV surface area. In Figure 4.2 we show the MV flowrate applied for this patient that belonged to the control group. We clearly observed that the amplitude of the A-wave was higher with respect to the MV flowrate used for the AF patients. Based on this data and a physiological flowrates of healthy patients in [66], we defined a representative MV flowrate for all the control group patients where the patient-specific MV or PVs Doppler measurements conditions were not available. Based on this additional information, in the model we modified the computation of the boundary conditions in case we have the patient-specific PVs flowrates available. Indeed, by writing the mass balance equation (see Equation 2.19), in this case the known terms are all the PVs flowrates. Therefore, the only term that needs to be easily computed from the mass balance equation is the Q^O. In this case, with respect to the Section 2.4.5, it is not needed to assign the flux Q^{pv}_{tot} through the four pulmonary veins with a criteria based on their sectional area.
This approach was not used for the patients enrolled until now, however it could be useful if patient-specific PVs flowrates are available. For each LA

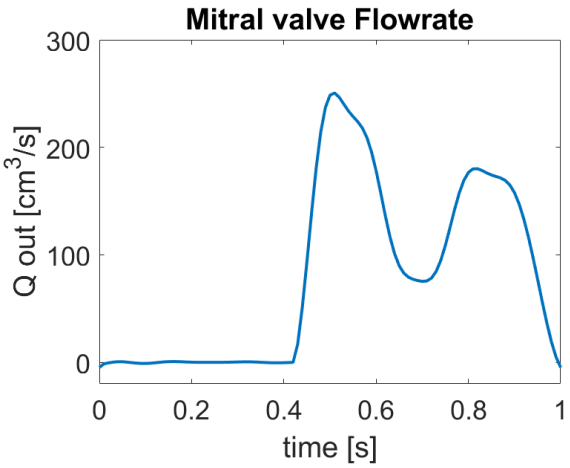

Figure 4.2: Patient-specific MV flowrate in one cardiac cycle for one patient who belonged to the control group.

anatomical model, we performed a simulation in SR condition. Simulations were run for five cardiac cycles to avoid the influence of the unphysiological initial condition on fluid velocity. We report the results of the fifth simulated cardiac cycle.
Regarding the parameters of the fluid dynamics model, the time step was set to 0.005 seconds, dynamic viscosity was 0.035 *poise* and the density was set to 1.06 g/cm^3.
The most significant parameters able to describe LA fluid dynamics including velocity and vortex structures, LAA orifice velocity and mainly the LAA residence time were computed. For the computation of the vortex structures the Q-criterion was employed. Through this quantity, we identified and visualized some connected regions where $Q > 0$ and the pressure was lower than the ambient value at the vortexes core. Lastly, we also computed the LA kinetic energy and we focused on the fluid dynamics of the LAA.
For the velocity and vorticity analysis we took as reference three patients, one for each group (control, paroxysmal AF and persistent AF) in order to perform the comparison between the three conditions. Regarding the patient from the control group, we chose the one with also the patient-specific MV flowrate, as explained in the previous paragraph.

4.2 Results and Discussion

4.2.1 General Overview

Simulations of each patient of the three groups were performed in sinus rhythm, considering the acquisition of the CT data during the cardiac cycle. We found higher values of the velocity inside the LA and in the LAA in the control group patients with respect to the AF patients. This is due to a stronger contraction-expansion of the LA throughout the cardiac cycle with respect to the AF patients, where the arrhythmia probably caused a reduction of the contractile activity of the LA cells. In the AF patients, we also detected a non-perfect synchronized contractile activity of the LA cells with a less organized blood flow pattern within the LA chamber compared to the control patients. Moreover, other parameters as kinetic energy and LAA orifice velocity showed much higher values in control group patients with respect to the AF patients, as expected.
Regarding the vortex structures, a higher number was observed in the control group patients with respect to the AF patients, thus favouring a better washout of the atrial chamber and the LAA (confirmed also by the fluid particle analysis). As discussed for the velocity, these findings were expected because the LA in a control patients group showed a higher variation of the volume during the cardiac cycle, thus implying a higher probability of the vortex structures formation and consequently a better washout of the atrial chamber with respect to the AF patients.

4.2.2 Detailed analysis

The simulated LA blood velocity in three patients, representative of the three groups, is displayed in Fig. 4.3. During the beginning of the ventricular systole, we noticed an increment of the velocity at the PVs for all the simulations. This increment was due to the atrial diastole: according to the principle of mass conservation, volume variation must be compensated by the entrance of blood flow from the PVs. The magnitude of the velocity field was still relatively small for the persistent AF patient, in particular we noticed the highest velocity close to PVs was $15 \div 20\ cm/s$. A potential reason for this effect is that the LA expansion was compromised by the persistence of AF that caused changes in the LA anatomical structure and reduction of the contractile activity of the LA cells. On the contrary, velocity at the PVs was higher for control and the paroxysmal AF patient with mean velocities around 30 cm/s and $35 \div 40 cm/s$, respectively. The mean PVs velocities

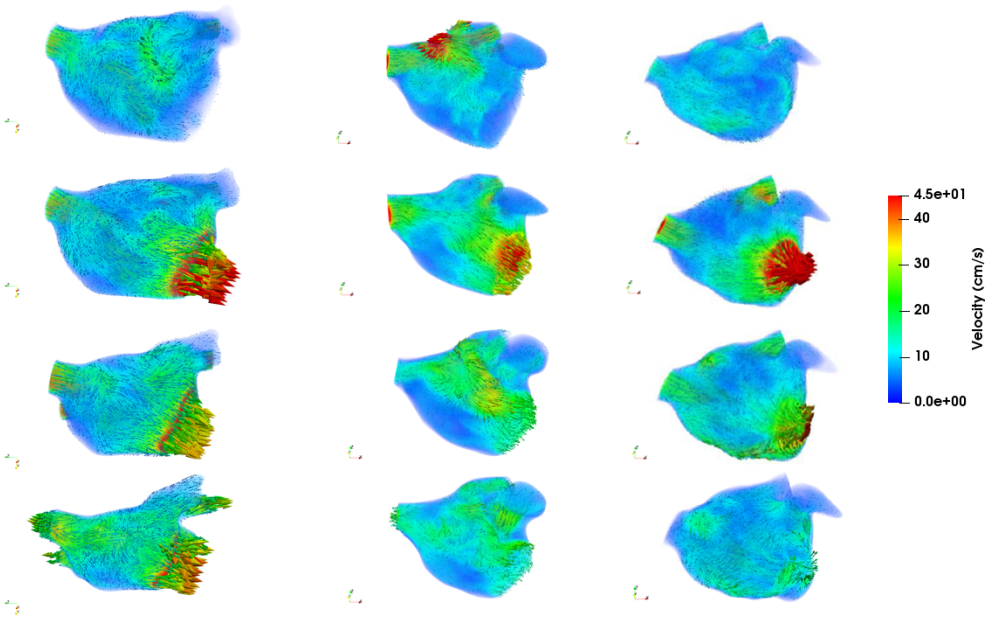

Figure 4.3: LA blood flow velocity in a control group patient (first column) in a paroxysmal AF patient (second column) and in a persistent AF patient (third column). First row referred to the beginning of the ventricular systole, second row referred to the beginning of ventricular diastole, the third row to the atrial sistole and the fourth row to the end of ventricular diastole

were higher in the paroxysmal AF patient with respect to the control group because of a higher velocity peak near to the LA roof due to a collision of the two flowrates coming from the RSPV and LSPV. This meant that the expansion of the LA in the paroxysmal AF condition was still good and not strongly compromised by the AF episodes as seen for the persistent AF patient. However, we noticed that in the other parts of the LA, velocities were higher in the control group patient with respect to the AF patients.
At the beginning of ventricular diastole (second row Figure 4.3), the control patient showed higher values of velocity in the center of the atrial chamber, at the PVs (mean value 55 cm/s) and mainly at the MV (mean value 95 cm/s) with respect to the paroxysmal (mean PVs value 40 cm/s, mean MV value 80 cm/s) and persistent AF patients (mean PVs value 30 cm/s, mean MV value 67 cm/s). Moreover, all the velocity vectors were all directed to the MV with respect to the persistent AF patient simulation where we cleary noticed that the blood flow was less organized and vectors toward the MV not always showed the same direction. The paroxysmal AF patient simulation showed an average behaviour between the control and persistent group because the blood flow was more ordered with respect to the persistent AF

but with lower values of the velocity, expecially at the MV, within the LA, than the control patient.
During the atrial contraction (third row Figure 4.3), the velocity at the MV was strongly higher in the control patient (mean value 50 cm/s) with respect to the AF patients (35 cm/s and 25 cm/s for paroxysmal and persistent AF simulation, respectively). This because of the atrial systole that helped the remaining blood flow within the LA to move through the MV to the left ventricle. Because the atrial contraction in the control group patient is regular and not affected by the AF, the velocity at the MV had a strong increase with respect to the AF patients where the reduction of the contractile activity of the left atrial cells has compromised the atrial contraction, thus implying a reduction of the velocity increase at the MV. However, we cleary noticed that for the paroxysmal AF patient the atrial contraction was stronger with respect to persistent AF patient with higher values overall the atrial chamber and mainly at the MV. Moreover, in the persistent AF patient velocity vectors were less organized with also discordant verse at the MV.
The atrial contraction caused also an increment of the blood flow velocity at the PVs higher in the control patient with respect to the AF conditions. The paroxysmal AF patients showed velocity values at the PVs and within the other parts of the atrial chamber between the control and persistent AF patient.
One of the most important differences between the three conditions was during the end diastole phase (fourth row Figure 4.3). Indeed, we saw a strong backflow at the PVs in the control group patient. This backflow at the PVs was completely normal and physiological in a healthy patient (A_r wave [92]), occurred after the atrial systole and confirmed the reliability of the CFD model to reproduce the LA physiological behaviour. Indeed, as reported in literature [66], this wave was absent in persistent AF patients and strongly reduced in the preliminary form of the arrhythmia like the paroxysmal AF. The CFD simulations confirmed these theoretical concepts: in the paroxysmal AF patient we observed a little backflow at the PVs with respect to the persistent AF patient where these PVs backflows were completely absent. However, backflows in the paroxysmal AF patient (mean value 10 cm/s) were much inferior to the control group patient (mean value 25 cm/s). The absence of this backflow in the persistent AF patients demonstrated the reduction of the contractile activity of the LA cells expecially during and after the atrial systole.
Based on the observations reported on the most important phases of the cardiac cycle we concluded that generally, as expected, the velocities within the LA showed higher values in the control group patients with respect to the paroxysmal and persistent AF patients. Moreover, the lowest values within

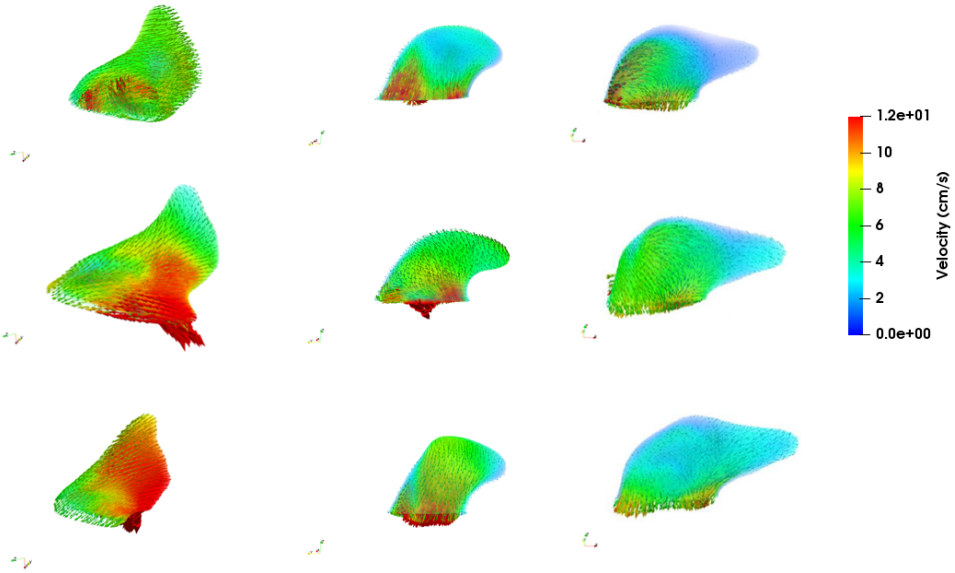

Figure 4.4: LAA blood flow velocity in a control group patient (first column) in a paroxysmal AF patient (second column) and in a persistent AF patient (third column). First row referred to the ventricular systole, second row referred to the beginning of ventricular diastole, the third row to the atrial sistole.

the LA were observed in the persistent AF group that could imply a higher probability of blood stasis and consequently an increase of the stroke risk. In the paroxysmal AF group we observed values that represented an average situation between the control and persistent AF group. Indeed, the contractility of the LA is not strongly reduced as for the persistent AF patients thus leading to higher values of the velocities and a stronger LA contraction/expansion with respect to the persistent AF. This could reduce the probability of clot formation.

We also focused on the velocity analysis on the LAA and results are reported in Figure 4.4. We observed higher values of the velocity at the LAA ostium and also towards the LAA tip in all the time instants of the cardiac cycle for the control patient with respect to the paroxysmal and persistent AF group patients that allowed a better LAA washout and reduction of the probability of blood stasis. In the persistent AF patient we found lower values of the velocity at the LAA ostium (mean value 12 cm/s) with respect to the paroxysmal AF patient (mean value 25 cm/s) mainly during the ventricular diastole (second row Figure 4.4). Yet, in the distal part of the LAA we found that the velocities in the LAA tip were the lowest in persistent AF patient

during all the phases of the cardiac cycle thus increasing the probability of blood stasis in this part of the LAA. Regarding the paroxysmal AF patient, velocity towards the LAA tip was higher with respect to the persistent AF patient expecially during the ventricular diastole and atrial systole (second and third row Figure 4.4) thus allowing a better washout of the LAA in this condition. Otherwise, these values remained much lower with respect to the control group patient, where the values of the LAA ostium velocity reached the highest values; up to 40 cm/s during ventricular diastole and also in correspondence of the LAA tip mainly during the atrial systole (third row Figure 4.4) where the velocity reached the value of 30 cm/s. This behaviour allowed the blood flow to ensure a correct washout of the LAA. From the LAA velocity analysis we clearly observed also the differences in the velocity vectors direction in the three conditions: in the control group and paroxysmal AF patients we observed the same directionality of the velocity vectors towards the LAA ostium during the ventricular diastole and the atrial systole with also high velocity values during the atrial systole for the paroxysmal AF patient. On the contrary, in the persistent AF patient the blood flow was more chaotic and less organized with respect to the other two groups. It seemed that the blood flow was constrained to remain inside the LAA and encountered difficulties to exit from it expecially during the atrial systole. To this purpose, the lack of contraction in this phase did not allow the blood to flow out of the LAA tip from the LAA ostium, despite we observed an increase of the velocity in the LAA distal part from the ventricular systole to the atrial systole. After a certain number of cardiac cycles, this could favour a formation of a clot that could increase the patient-specific stroke risk.
Therefore, it was clear that the blood flow entered during the ventricular systole in the LAA and exited from it during the ventricular diastole and strongly during the atrial systole with a more ordered pattern in the control patients with respect to the AF conditions where the blood flow seemed more chaotic and less synchronized mainly for the persistent AF condition.
To conclude the LAA velocity analysis, we observed from the Figure 4.4 that the contraction of the LAA was strong for the control group patients, expecially during the atrial systole, where we saw that the LAA volume has strongly been reduced in order to allow the blood flow to exit. In the paroxysmal AF condition, the LAA contraction was not strong as for the control patient but not scarce; this allowed to reduce the probability of the blood stasis with respect to the persistent AF LAA. Indeed in this last group, the LAA showed very small changes in its morphology and volume throughout the cardiac cycle caused by the continuity of arrhythmia, thus resulting in a scarce contractile activity, implying a higher risk of the probability of the blood clots mainly in its distal part.

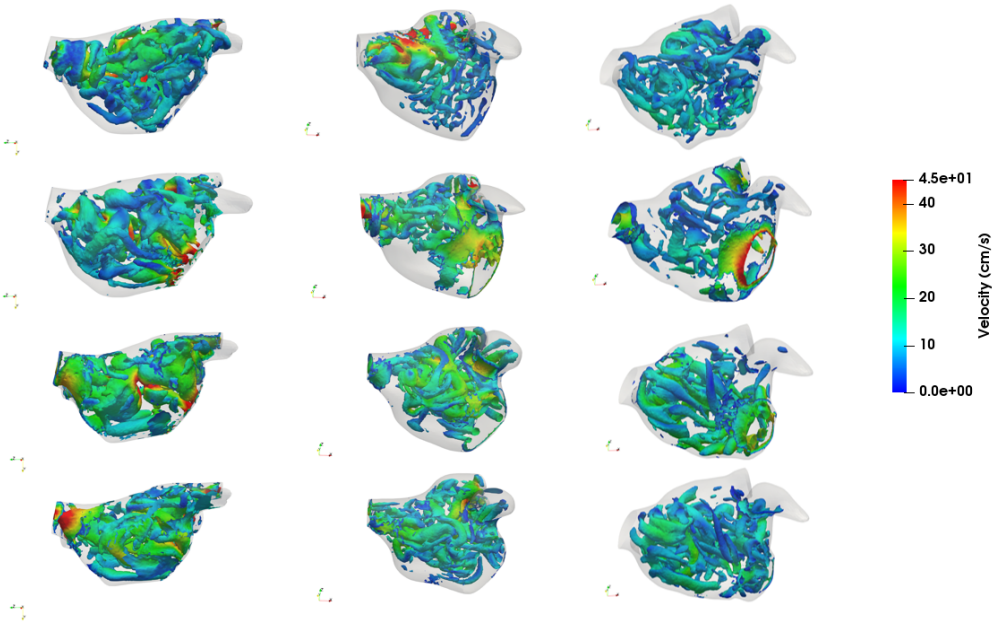

Figure 4.5: LA vortex structures in a control group patient (first column) in a paroxysmal AF patient (second column) and in a persistent AF patient (third column). First row referred to the beginning of the ventricular systole, second row referred to the beginning of ventricular diastole, the third row to the atrial sistole and the fourth row to the end of ventricular diastole

We computed the vortex structures within the LA and results are showed in Figure 4.5.

The number of the vortex structures and their dimension was much higher in the control group with respect to the AF patients in all the time instants of the cardiac cycle. Moreover, the vortex structures covered all the LA parts. This behaviour ensured a strong washout within the LA chamber, therefore the risk of blood statis could be considered as null. Regarding the AF simulations, we observed that the number and the dimension of the vortex structures was higher in the paroxysmal AF patient with respect to the persistent AF patient. These findings confirmed that the contractile activity of the LA in AF paroxysmal patient was not compromised as for the persistent AF case. The presence of higher number of vortex structures with respect to the persistent AF allowed a better washout within the LA and could reduce the probability of the blood stasis.
Moreover, during the E and A wave (second and third row Figure 4.5), most of the vortex structures converged to the MV with high velocities in the control group. This means that the blood flow was more ordered with respect to

the AF patients where we saw that the blood flow seemed more chaotic. To this purpose, a ring shape structure around the MV was observed in the AF patients during the ventricular diastole and atrial systole, bigger in the persistent AF patient. This vortex structure meant that the blood flow also rotated around the MV before passing to the LV, therefore implying a less ordered blood flow pattern in correspondence of E and A wave. From Figure 4.5 we also clearly observed that the LA volume variation (contraction/expansion of the LA chamber) throughout the cardiac cycle was higher in the control case with respect to the AF patients. Moreover, in the paroxysmal AF patient LA volume variation was higher than in the persistent AF patient, expecially the LA contraction during and after the atrial systole (third and fourth row Figure 4.5). Indeed, we noticed that the volume variation of the LA for the AF persistent case was strongly reduced and this could favor the risk of blood stasis. The presence of the LA motion throughout the cardiac cycle helped the vortex structures to leave the LA chamber and to guarantee the blood washout within the LA chamber.
Lastly, as described in the velocity field analysis, we observed at the end of ventricular diastole a presence in each PV of the vortex structures caused by the PV backflows expecially in the control group patient. Indeed, in the paroxysmal AF patient the dimensions of the vortex structures due to the backflow at the PVs were more reduced with respect to the control group patient because, as described in the velocity field analysis, the amplitude of the backflow at the PVs was much lower in the paroxysmal AF patient with respect to the control group patient. Moreover, these PV backflows were completely absent in the persistent AF patient and this result was also confirmed by the vortex structures (see fourth row Figure 4.5). Indeed, no vortex structures were observed near to the PVs in the persistent AF patient.
We also performed the computation of the vortex structures within the LAA and results are shown in Figure 4.6. During the ventricular systole (first row of Figure 4.6), the vortex structures were more numerous and bigger, as for the LA, in the control patient with respect to the AF patients. The blood flow entered in the LAA and we noticed that the vortex structures were moving to the LAA distal part. We observed that in the control group patient, vortex structures were nearer to the LAA tip with respect to the AF patients LAA, thus implying a better washout in this LAA part. Regarding the paroxysmal AF patient LAA, we observed a good presence of the vortex structures also in its middle part and also near to the LAA tip, despite in a lower number with respect to the control group patient. During all the cardiac cycle phases we noticed a good washout of the entire LAA in this patient. As an example, looking at the atrial systole phase (third row Figure 4.6), the dimension of the vortex structures was the highest in the paroxysmal

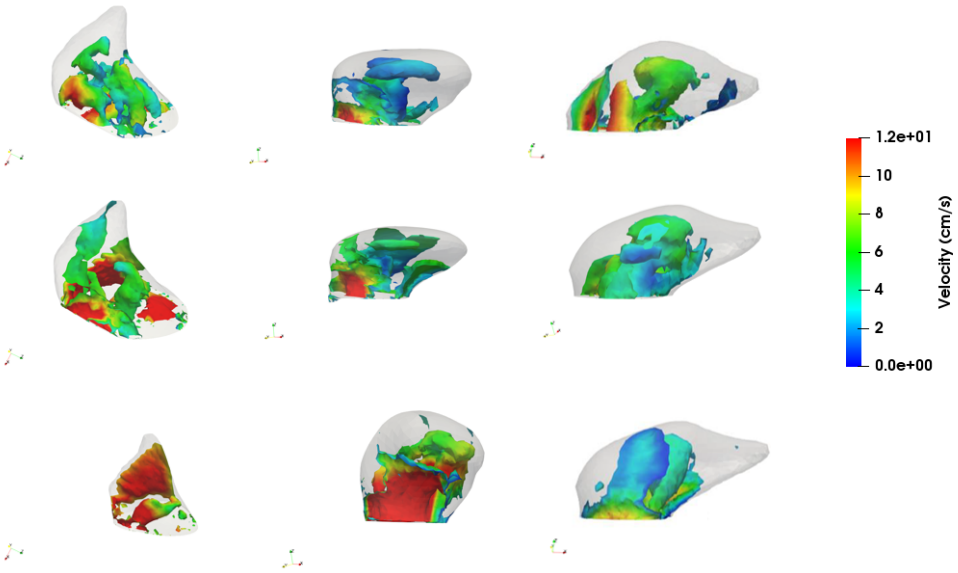

Figure 4.6: LAA vortex structures in a control group patient (first column) in a paroxysmal AF patient (second column) and in a persistent AF patient (third column). First row referred to the ventricular systole, second row referred to the beginning of ventricular diastole, the third row to the atrial sistole.

AF patient. However, in the control patient the vortex structures guaranteed a complete and better coverage of all the LAA parts despite the single dimension of the vortex structures was lower than in the AF paroxysmal case. In the persistent AF patient the number of the vortex structures were the lowest compared to the other two simulations. The dimension of the vortex structures was higher near to the LAA ostium but with lower velocities with respect to the paroxysmal AF and control patient. Moreover, we observed that the middle-distal part of the LAA in the persistent AF patient has not been fully reached. These findings confirmed that the probability of the blood stasis and consequently the stroke risk was the highest in the persistent AF patients with respect to the paroxysmal AF and control patient.
In Figure 4.6 we appreciate the motion of the LAA during the cardiac cycle: in the healthy patient we clearly observed a strong contraction-expansion cycle of the LAA. Altough more reduced with respect to the control patient, also the paroxysmal AF patient LAA showed a quite good motion throughout the cardiac cycle. In the persistent AF patient this motion was scarce and the LAA volume did not vary so much in the cardiac cycle. Therefore, the probability of the blood clot formation could be higher in the persistent AF case with respect to the other patients.

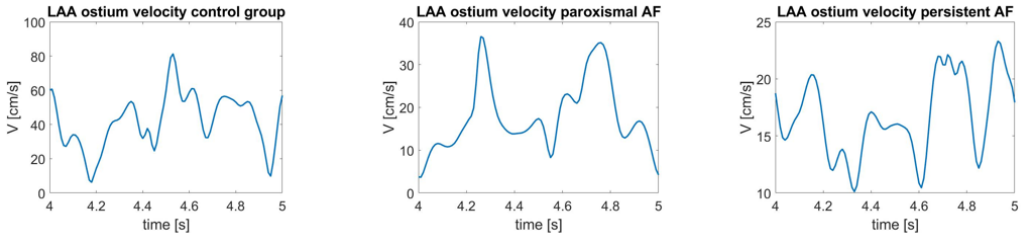

Figure 4.7: LAA orifice velocity during the fifth cardiac cycle in a control group patient (left panel), in a paroxysmal AF patient (middle panel) and in a persistent AF patient (right panel).

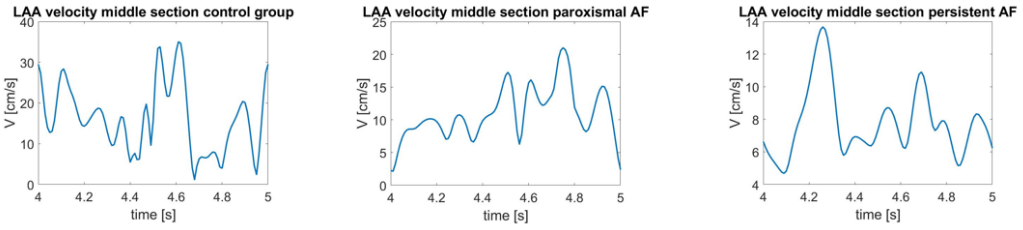

Figure 4.8: LAA middle section velocity during the fifth cardiac cycle in a control group patient (left panel), in a paroxysmal AF patient (middle panel) and in a persistent AF patient (right panel).

We computed also the LAA orifice velocity for each patient and results are reported in Figure 4.7. The control group patient showed the highest values of the average (50 cm/s) and peak velocity (82 cm/s); this meant a strong washout of this part of the LA. However, the situation was not the same for the AF patients. In both paroxysmal and persistent AF patients, a higher oscillatory pattern was observed, expecially in the persistent AF case, that could have been probably due to the lack of a synchronized contraction/expansion of the LA cells caused by the arrrythmia. The average and peak values of the velocity of the LAA ostium in the paroxysmal AF patient (26 cm/s and 37 cm/s, respectively) were higher with respect to the persistent AF patients (mean value 17 cm/s, peak value 27 cm/s). This implied that the contractile activity was more present, despite it was reduced with respect to a healthy patient, in the paroxysmal AF patient with respect to the persistent AF patient, where the continuity of the arrhythmia caused permanent structural changes in the LA cells and reduced the LAA washout. As reported in Section 3.7.4, studies in literature [79] have shown that speeds below 40 cm/s in corrispondence of the LAA ostium are associated with a higher risk of stroke, while speeds below 20 cm/s are associated with the

identification of thrombus. The persistent AF patient was the only one that showed an average velocity value below the threshold of 20 cm/s, thus highlighting a potential thrombogenic spot. Looking at the velocity in the LAA middle section for all groups patients (see Figure 4.8), also in this case the highest values of the velocity were in the control group patient. However, we noticed that the paroxysmal AF patient showed velocity values nearer to the control patient with respect to the persistent AF patient, where the values were very low throughout the cardiac cycle. This behaviour implied a not sufficient blood washout of the LAA moving from the LAA ostium to the LAA tip for the persistent AF case, thus highlighting the probability of stroke risk.

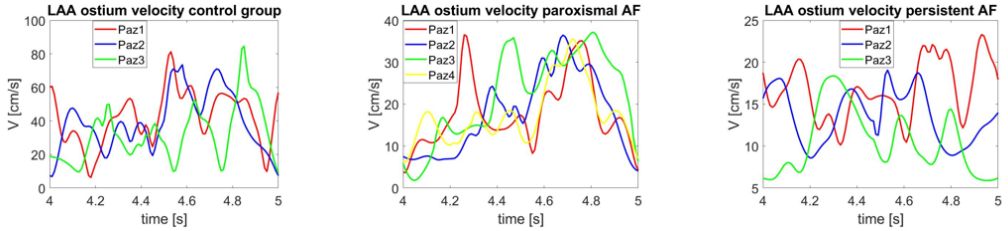

Figure 4.9: LAA ostium velocity during the fifth cardiac cycle in the three control group patients (left panel), in the four paroxysmal AF patients (middle panel) and in the three persistent AF patients (right panel).

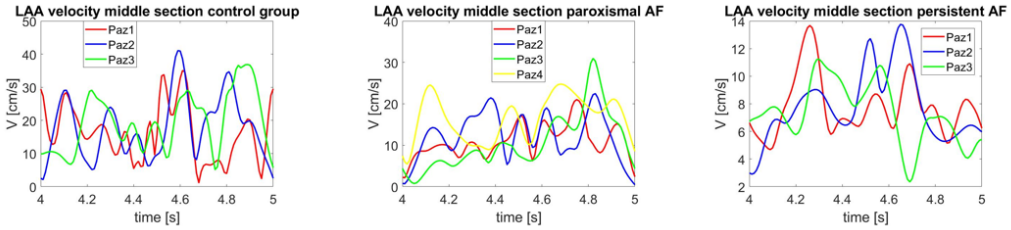

Figure 4.10: LAA middle section velocity during the fifth cardiac cycle in the three control group patients (left panel), in the four paroxysmal AF patients (middle panel) and in the three persistent AF patients (right panel).

The aformentioned findings were confirmed also for all the 10 patients involved in the study. In Figures 4.9 and 4.10, results in the LAA orifice and in the middle section of the LAA for all the patients analyzed in each group are depicted. We also took into account in the evaluation of the haemodyamics parameters the kinetic energy. In particular, we computed it in one patient for each group (the same used for the velocity and vorticity analysis). Results are shown in Figure 4.11. By looking at the control patient, we clearly

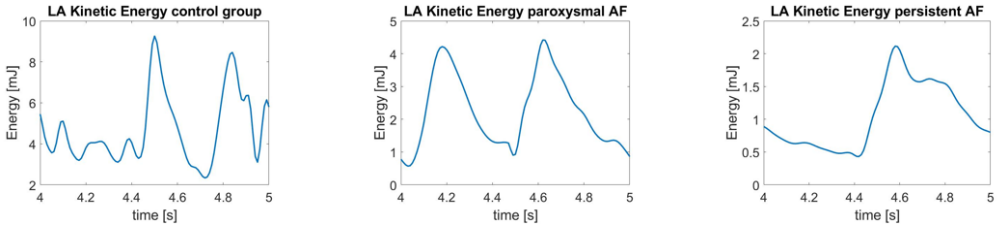

Figure 4.11: LA kinetic energy during the fifth cardiac cycle in a control group patient (left panel), in a paroxysmal AF patient (middle panel) and in a persistent AF patient (right panel).

observed that the kinetic energy peak values (8-9 mJ) occurred in correspondence of the E wave and the A wave of the MV flowrate. Moreover the values of the peaks were the highest with respect to the other two simulations. This meant that the contraction/expansion of the LA was regular, organized and synchronized because the highest values of energy were observed in the two phases where the highest release of the LA energy throughout the cardiac cycle was theoreticallly expected. In the paroxysmal AF patients the kinetic energy peak values were higher with respect to the persistent AF patients (peak value paroxysmal AF 4 mJ, peak value persistent AF 2 mJ). However, with respect to the control patient, the two peaks were localized before the E and A wave. We hypothesized that probably, the non-perfect synchronized contractile activity of the LA cells, influenced by the AF, implied a less organized blood flow pattern within the atrial chamber. Therefore, this probably explained why the highest release of energy in this patient was before the E and A wave and not in correspondence of them as for the healthy case. Moreover, as expected, the values of the kinetic energy in the AF patients were lower with respect to the control patient. In the persistent AF patient we found the lowest values of the kinetic energy compared to the other two simulations and we observed only one peak in correspondence of the E wave. The peak in correspondence of the A wave was missing and this was probably due to the lack of the contraction of the LA during the atrial systole. Therefore, these lower values of the kinetic energy could be correlated to the blood stagnation risk in the atrial chamber and mainly in the LAA.
Lastly, to complete the analysis of the haemodynamics comparison between the control and the two cases of AF, we performed the LAA residence time study previously described in Section 2.5.2. We populated the LAA with 500 fluid particles at the beginning of the simulation and we counted how many particles remained inside the LAA after five cardiac cycles. The fluid particles were distributed as a sphere around the center c, which represented

the midpoint of the LAA centerline. The analysis was performed for all the ten patients enrolled in the study and results are reported in Table 4.1 for the control group patients, in Table 4.2 for the paroxysmal AF group patients and in Table 4.3 for the persistent AF group patients.

CC	P1	P2	P3
start 1 CC	500	500	500
end 5 CC	6	2	5

Table 4.1: LAA fluid particles computation after 5 cardiac cycles (CC) for the three control group patients. P states for Patient.

CC	P1	P2	P3	P4
start 1 CC	500	500	500	500
end 5 CC	17	14	21	16

Table 4.2: LAA fluid particles computation after 5 cardiac cycles (CC) for the four paroxysmal AF group patients. P states for Patient.

CC	P1	P2	P3
start 1 CC	500	500	500
end 5 CC	45	38	33

Table 4.3: LAA fluid particles computation after 5 cardiac cycles (CC) for the three persistent AF group patients. P states for Patient.

The results of the LAA residence time confirmed the aforementioned findings. Indeed, the lowest number of particles that remained in the LAA was in all the control group patients. Therefore, we concluded that the risk of clot formation within the LAA in a healthy patient could be considered almost null. Comparing the two AF conditions, we observed that in the paroxysmal AF patients the number of remaining particles within the LAA after five cardiac cycles was lower compared to the persistent AF patients. These results confirmed our previous findings based on the evaluation of the other param-

eters. The reduction of the LAA blood washout of the persistent AF patient was due to the lack of the LAA contraction caused by the persistence of the arrytmia that implied anatomical and structural changes of the LA and the LAA. For this reason, the risk of the blood stasis and consequently the stroke risk was the highest in the persistent AF group patients, while in the paroxysmal AF patients we could define a medium stroke risk based on the obtained results. Indeed, it seemed that the paroxysmal AF group showed an average behaviour between the control and persistent AF group. This was probably due to the low frequency of the AF episodes and their spontaneous interruption that still did not caused permanent changes of the structure of the LA cells and consequently of their contractile activity altough the physiological behaviour was compromised by the arrhythmia. Therefore, the LAA blood washout was better with respect to the persistent AF condition.

Results demonstrated the capabilities of the CFD model to reproduce the real physiological behaviour of the blood flow dynamics inside the LA and the LAA. In fact, as expected, the velocities within the LA and LAA showed higher values in the control group patients with respect to the paroxysmal and persistent AF patients. Moreover, the lowest values within the LA and LAA were observed in the persistent AF group that could imply a higher probability of blood stasis and consequently an increase of the stroke risk. In the paroxysmal AF group we observed values that represented an average situation between the control and persistent AF group.
Moreover, the vortex structures, the LAA ostium velocity, the kinetic energy and the LAA residence time analysis confirmed what we qualitatively expected about the differences of the three groups.
Finally, we determined that the fluid-dynamics parameters enhanced in this research project could be used as new quantitative indexes to describe the different types of AF and open new scenarios for the patient-specific stroke risk stratification.

Conclusions and future perspectives

In this study we developed what, to the best of our knowledge, is the most advanced effort towards a fully personalized CFD model of atrial blood flow in AF. Hereto, dynamic real imaging data were used to extract patient specific detailed anatomy and motion model during SR. Moreover, realistic MV flowrate profiles or patient-specific Doppler measurements, if applicable, were used to set inflow and outflow boundary conditions.
In this research project, we tested the developed patient-specific CFD model in several applications in order to explore the different clinical scenarios and to have a better understanding of the haemodynamics implications in atrial fibrillation. Considering the overall results obtained in this project in the different studies, the developed tool might be used for enabling personalized stroke risk stratification and therapy planning.

Development of the patient-specific LA CFD model

Taking into account the obtained results from the Chapter 2, the designed workflow was tested in two different conditions, SR and AF in two different AF patients. Part of the work described in the Chapter 2 was published in [42]. In these preliminary testings, the model highlighted expected differences in velocity and vortex formation in the two conditions and confirmed that AF episodes resulted in a reduced washout of the LAA compared to the SR condition, which may lead to the formation of thrombi. Differently from the other works published in literature, in our CFD model we imposed a Dirichlet boundary condition for each PV considering also the PVs sections move and their area change over the cardiac cycle. The choice to scale the velocity according to PVs sectional area was made because we think it is the most appropriate and suitable for the future developments of the model on

a patient-specific basis. In view of a clinical application, the model could be easily improved including data from PW Doppler velocity measurements.
Regarding the MV, we employed a natural boundary condition with a weakly penalization term of the reverse flow, to avoid instability of the discrete formulation of the problem, eventually caused by the backflows at the MV.
One limitation of the developed approach consisted in the motion field used for AF simulation that was based on a random displacement function. New strategies for AF wall motion simulations could be more realistic than using a random displacement function as the one employed in this study.
To gain knowledge on this important topic, we developed different cardiac contraction models of the LA in AF, as described in Section 2.6. In particular, to simulate AF, three different motion models were employed for the CFD simulation: the random model, the discrete model and the sinusoidal model. The sinusoidal model was the one showing an adequate blood washout, despite less than SR condition, thus implying a lower thrombi formation risk and consequently stroke risk. In order to confirm the aforementioned findings, we performed a specific study to try to quantify the LAA blood stasis. Results confirmed our considerations based on the velocity and vorticity analysis. We found an expected reduced washout expecially for the AF random model and discrete AF model which in the long term might be indicative of the generation of blood clots. Therefore, the choice of the motion model used for simulating the AF condition showed an impact on the fluid-dynamics parameters and should be taken into account in the CFD studies of the LA and the LAA.
Despite the aforementioned results, another limitation of the study was that the motion field used for AF simulation was based on a modelling approach. New strategies for AF wall motion simulations may include a fluid structure interaction (FSI) model in which the control of the motion of the computational domain throughout the cardiac cycle could be more realistic. Moreover, once the patient-specific motion in AF has become available, for example by using 3D real time echocardiography data, our pipeline would strongly benefit from such information.

Analysis of the fluid-dynamics impact of the LAA in AF patients

In Chapter 3 we focused our attention to the LAA, given its role in the blood clot formation and consequently in the increase of the stroke risk. In fact, 90 % of the intracardiac thrombi in patients with cardioembolic stroke/TIA are

considered as originating in the LAA [14]. The aim of the study presented in this chapter was the design and development of a workflow to quantify the influence of LAA morphology alone on the LA hemodynamics. Part of the content of this chapter 3 is published in [68]. Simulations of the haemodynamics within the LA and LAA in AF conditions were performed. Our results on the velocity and vorticity within the LAA, LAA orifice velocity and on the residence time demonstrated and confirmed that not only complex LAA morphologies were characterized by low velocities, low vorticity and consequently a higher thrombogenic risk. Simple morphologies can have a thrombogenic risk equal, or even higher, than more complex auricles and their geometric features could play a key role in defining thromboembolic risk. Indeed, in our opinion, LAA geometric parameters should be considered, coupled with the morphological characteristics, for a comprehensive evaluation of the blood stasis and stroke risk. These geometric characteristics were not investigated in the previous works, neither correlated with hemodynamic parameters. Obviously the clinical problem we are facing is very complex and we think there may be an interchangeable conditioning effect between the LA and the LAA shapes and both effects should be considered. However we also think the comprehension of each single effect may help in clarifying the interplay between them. In this study we focused on better understanding the influence of each specific LAA shape on blood hemodynamics and, to this aim, we were forced to eliminate the dependence from the LA shape and from other patient-specific factors. Our results showed that the complexity of the LAA shape alone does not correlate with clot formation and additional parameters should be considered for a clear comprehension of the link between LAA shape and the risk of stroke.

Our approach can be further improved because a limitation consisted in the number of the available left atrial data-set. Future developments will be focused on considering a larger number of patient-specific LAAs in order to fully consider its wide anatomical variability. In addition, the results of this study could benefit from the application of a patient-specific motion field of the LA in AF. Unfortunately, up to date, quantification of such a motion field is not possible using the standard 3D acquisition, MRI or CT.

Related to this work, we also studied the effect of the LAA occlusion devices on the LA fluid-dynamics in AF patients through the use of the CFD simulations. To this purpose, LAAO was reproduced on 3D LA anatomical models obtained from real clinical data of five AF patients. For each patient, CFD simulations in AF condition were performed on the entire atrium model and on the models with the two LAAO. Significant fluid dynamics indices were determined to evaluate the changes in the flow patterns after the occlusion in relation to the thrombogenic risk. Our results suggested a

more effective blood washout after LAAO and, consequently, a lower risk of blood clot formation. Also, a slightly improved washout effect is revealed when the Watchman device is implanted. These findings were also confirmed and in accordance with the studies of [90, 91] where the LA fluid-dynamics pre and post LAA occlusion was studied. In these studies, they also found a higher LAA orifice velocity and a more organized blood flow within the LA expecially near to the MV after the LAA occlusion.
Obviously, a limitation of this study was the simulation of the LAA occlusion without having the specific 3D model of the device that could better clarify the impact of the occlusion in the atrial chamber.

Haemodynamics differences between healthy and AF patients: the FATA study

Lastly, in chapter 4 we computed the haemodynamics in patients with and without AF and in patients with different pathophysiological conditions in order to enhance the differences in the fluid-dynamics indexes evaluated from the simulations. Moreover, we computed the most important parameters from the CFD model that potentially stratify the stroke risk on a patient-specific basis. Results demonstrated the capabilities of the CFD model to reproduce the real physiological behaviour of the blood flow dynamics inside the LA and the LAA. In fact, as expected, the velocities within the LA and LAA showed higher values in the control group patients with respect to the paroxysmal and persistent AF patients. Moreover, the lowest values within the LA and LAA were observed in the persistent AF group that could imply a higher probability of blood stasis and consequently an increase of the stroke risk. In the paroxysmal AF group we observed values that represented an average situation between the control and persistent AF group. Indeed, the contractility of the LA was not strongly reduced as for the persistent AF patients thus leading to higher values of the velocities and a stronger LA contraction/expansion with respect to the persistent AF. This could reduce the probability of clot formation. The aforementioned findings were also confirmed by the analysis of the vortex structures and of the LAA residence time. We also demonstrated that the expansion/contraction cycle of the LA was regular, organized and synchronized in the control group patients and strongly reduced and not ordered in the persistent AF patients.
In the paroxysmal AF condition we also saw a non-perfect synchronized contractile activity of the LA cells with a less organized blood flow pattern within the LA chamber compared to the control patients. However, the LA

and LAA motion and also the atrial contraction was clearly observed in this group, thus meaning that the contractile activity was not compromised as for the persistent AF patients. In fact, the LAA washout was not scarce as for the persistent AF patients even if it was lower compared to the control group patients, where the LAA blood washout was effective and the risk of blood clot formation could be considered null. Future developments of the study will consist in confirming the obtained results in all the patients enrolled for the FATA study. Finally, a further future development would be to move towards a two-chamber model able to take the atrio-ventricular hemodynamic interactions into account [93]. This would help, for instance, to explain the connection between AF, valvular diseases and ventricular diseases such as heart failure [94].

To conclude, we believe that the proposed computational framework is feasible and able to successfully compute realistic LA blood flow dynamics in AF. Indeed, after a comprehensive validation, it could represent a significant advancement towards an optimized stroke risk stratification and therapy delivery on a patient-specific basis.

Appendix A

A fully automated left atrium segmentation approach from late gadolinium enhanced magnetic resonance imaging based on a convolutional neural network

A.1 Introduction

As reported in the first Chapter of the Thesis, Atrial fibrillation is the most common arrythmia in the western world with an incidence of about 0.4% in men and 0.6% in women. Radio frequency ablation (RFA) of the left atrium (LA) represents the clinical therapy for AF patients in which anti-arrhythmic drugs and direct current cardio-version do not provide improvements for the patient health. To this purpose, Haissaguerre and colleagues identified the pulmonary veins (PVs) as the most common sites for AF triggers [25]; for this reason PV isolation has become the milestone of AF RFA. However, despite strong improvements for the targeting and the delivery of AF RFA, the long-term restoration of sinus rhythm is achieved only in a limited percentage

of AF patients: AF-free rates after a single ablation vary between 30 and 50% at 5 years follow-up [95, 96]. These results suggest there is room for improvements in RFA treatment and underline a lack of understanding of mechanisms sustaining AF.

Magnetic resonance imaging (MRI) is capable of differentiating between scarred and nonscarred atrial wall by using late gadolinium enhancement (LGE) imaging. Several clinical studies suggested that LA fibrosis is associated with AF and with AF recurrence after ablation . LGE MRI allows the detection of the fibrotic tissue to identify native and post-ablation atrial scarring leading to an improvement of the success rate of the RFA [97–99]. Unfortunately, in clinical practice, LGE MRI is rarely available since a standard acquisition protocol is not available [100]. As a surrogate index of fibrosis, during RFA, electroanatomical voltage maps are used considering that regions of low voltage correspond to fibrotic tissue areas [97]. In adddition, even if studies on atrial structure segmentation applied to LGE MRI have shown promising results, most of them were based on a time-consuming procedure of manual tracing of LA wall and PVs [98, 101–103]. Results are affected by high variability among experts and different research institutions and low reproducibility in multicenter studies. Different approaches for LA segmentation are based on different MRI data. Valinoti et al. [104] proposed a 3D LA patient-specific model from MRI angiography which could be easily integrated with fibrosis information from LGE MRI by simply registering the two datasets and using grey-level intensities from LGE MRI as a texture of the 3D anatomical model. Similarly Yang et al. [105] proposed a combined pipeline involving a multi-atlas based whole heart segmentation to determine cardiac anatomy from a balanced steady state free precession sequence which is then mapped to LGE MRI. Mortazi et al. [106] developed a 2-D convolutional neural network (CNN) approach for the LA and PVs segmentation from cine MRI steady state free precession sequences and CT data (STACOM 2013 Cardiac Segmentation Challenge [107]). Only very few studies were recently proposed to segment LA chamber from LGE MRI. Tao et al. [108] developed a fully automatic method for LA and PVs segmentation, with comparable performance to a human observer. Unfortunately their approach requires substantial computation time due to the extensive computation of the multi-atlas-based registration.

Therefore, the availability of a fast and fully automatic LA segmentation algorithm applied to LGE MRI is highly desirable. The aim of this study was the design and development of an automatic algorithm for the LA cavity segmentation from LGE MRI data. Our approach relies on a deep learning pipeline based on the successful architecture U-Net [109]. The neural network was trained end-to-end from scratch in 2-D (2-D pipeline) and 3-D (3-D

pipeline) using data available from the STACOM 2018 Atrial Segmentation Challenge.

A.2 Methods

A.2.1 Dataset

The method was applied to the STACOM 2018 Atrial Segmentation Challenge dataset, which includes 100 LGE MRI 3-D cardiac images with the related 3-D ground truth segmentations (0 for background and 1 for LA). In the following, the tuple composed by a 3-D cardiac image and the related ground truth segmentation is named as cardiac data.The data resolution is $0.625 \times 0.625 \times 0.625\ mm^3$ and the 3-D cardiac data was composed by 88 axial slices with in-plane size of 576×576 or 640×640 pixels. To train the neural network in the two proposed approaches, the dataset was split into a training set (80%, 80 cardiac data) and a test set (20%, 20 cardiac data). The training set was further split into the real training set and a validation set (10%, 8 cardiac data).

A.2.2 Rough segmentation and pre-processing

LGE MRI images are acquired in the axial plane using a standard protocol in which the LA chamber is located in the center of the images. This information can be exploited in order to reduce the number of pixels or voxels from which the CNN extracts information, and therefore the computational cost of the neural network training process. The subject specific LA position was assessed using a rough LA segmentation based on Otsu's algorithm applied to the central axial slice of each dataset (figure A.1). In particular, once the binary image resulting from Otsu's segmentation was obtained, the centroid of the region located in the center of the image was extracted (yellow point in figure A.1(b)). From this point, the limits of the region of interest in the x direction were automatically computed (green points in figure A.1(b)) as well as the midpoint between them (red point in figure A.1(b)). A 3-D crop of fixed size $88 \times 320 \times 384$ centered in the computed midpoint was extracted (red boxed region in figure A.1(b)) from the original cardiac data. Data were then subsampled to $88 \times 192 \times 240$ for the 2-D pipeline and to $80 \times 192 \times 240$ for the 3-D pipeline. The resizing of the images along the third dimension allowed a match between the dimensions of the tensors in the

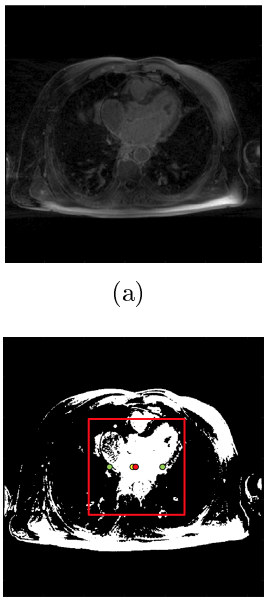

(a)

(b)

Figure A.1: Example of representative middle axial slice of an input image (a) and its rough segmentation using Otsu's segmentation algorithm with the computation of the crop x-y limits (b). Binary image resulting from the segmentation algorithm. The centroid of the central region of the image was extracted (yellow point) and then the x-limits of the region of interest were computed (green points). From these points, the midpoint of the crop was computed (red point). Finally, the crop containing the LA was extracted (red box).

concatenation layers of the neural network in the 3-D approach. Only these subsampled crops containing the LA chamber were used for the training, and all the tissues outside this crop were classified as background. The neural network was trained with these 3-D data (subsampled 3-D crops and the corresponding 3-D ground truth) in the 3-D pipeline and with 2-D axial slices (subsampled 2-D axial crops and 2-D ground truth) extracted from the 3-D data in the 2-D pipeline. This 3-D to 2-D axial slices transformation was required in order to train the neural network with a stack of 2-D data and it was applied separately to the training, test and validation set. In the 3-D pipeline the number of training, test and validation examples was 72, 20, 8, respectively, while in the 2-D pipeline the number of training, test and validation examples was 6336, 1760, 704, respectively.

A.2.3 Fine segmentation with CNN

In the following the architecture of the neural network, the training process, the inference and post-processing steps, and the evaluation metric are described.

CNN architecture

The deep learning approach proposed for the 2-D and 3-D pipelines was based on the U-Net architecture (figure A.2). The main hyper-parameters were chosen following the original U-Net architecture [109], while the number of convolutional filters and the learning rate were chosen empirically during an early evaluation stage. In the convolutional layers, kernel size of $3 \times 3 \times 3$ (3-D approach) or 3×3 (2-D approach), stride size of $1 \times 1 \times 1$ or 1×1 and Rectified Linear Units (ReLUs) activation functions in the hidden layers or sigmoidal activation function in the output layer were used. In the max pooling layers, a pooling size of $2 \times 2 \times 2$ or 2×2 and stride size of $2 \times 2 \times 2$ or 2×2, halving the shape of hidden activations, were employed. Lastly, in the transposed convolutional layers, kernel size of $2 \times 2 \times 2$ or 2×2 and stride size of $2 \times 2 \times 2$ or 2×2 were applied. For both convolutional and transposed convolutional layers, padding size was such that the output shape of the layer was the same of the input shape. Furthermore, biases and weights were randomly initialized from a truncated normal distribution and using the initialization scheme proposed by He et al. [110] for ReLUs, respectively. In addition to the original version of the U-Net [109], after each convolutional layer and before the activation function, a batch normalization layer [111] was included. This was an adaptive reparametrization technique introduced to reduce the covariance shift and to speed up the training process making models less sensitive to the parameters initialization. Furthermore, it introduced a regularization effect and, sometimes, reduced the need of computational heavy regularizers, such as Dropout [112].

The overall number of parameters for the 2-D approach was 1,946,705 (1,943,761 trainable parameters and 2,944 not-trainable parameters), while for the 3-D approach it was 5,650,801 (5,647,857 trainable parameters and 2,944 not-trainable parameters)

Training process

The neural network training was driven by a soft-dice loss function [113] proposed to introduce a balancing between foreground and background voxels (or pixels in the 2-D approach).

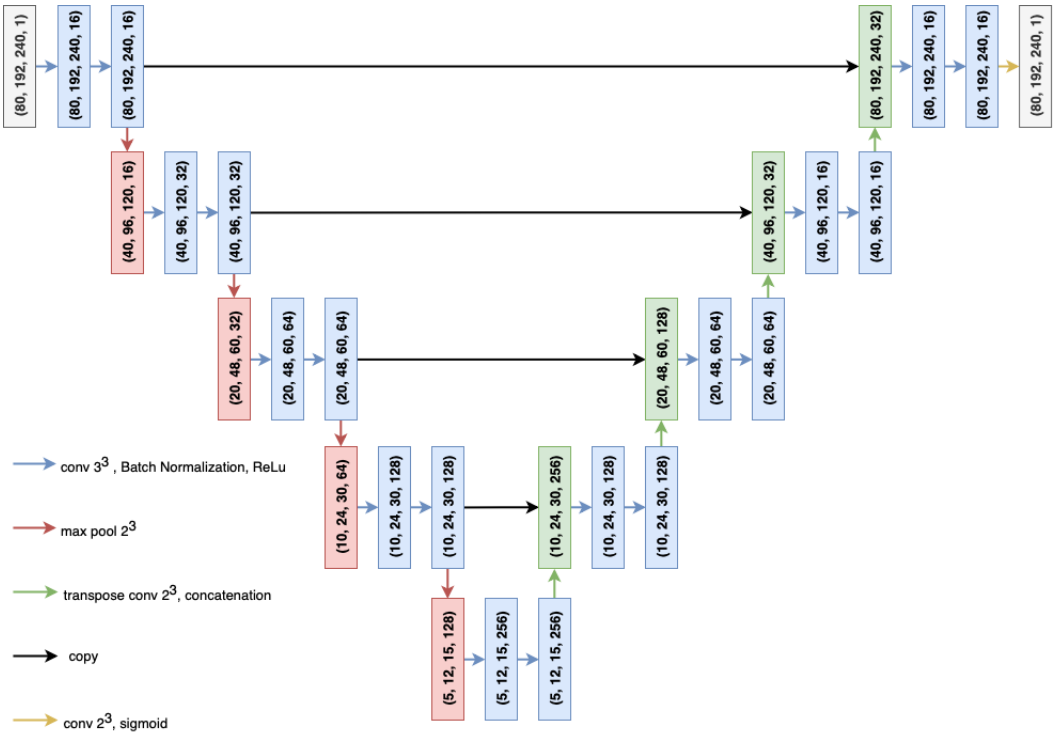

Figure A.2: The proposed CNN architecture for the 3-D approach. The 2-D architecture shared the same hyper-parameters and was easily obtainable from the 3-D architecture. Each item specified the tensor shape for each of the represented layers of the neural network and the arrow colors encoded different operators as explained in the figure legend. The two gray boxes represented the input and output tensors, the blue boxes the outputs of the convolutional layers, the red boxes the max pooled activations and the green boxes the concatenation between the activations of the transposed convolutional layers and the correspective activations in the encoder module.

The Soft-Dice coefficient SD [114] is an extension of the Dice coefficient that relies on the concept of disagreement between pairs of probabilistic classifications. Given the segmentation S and the ground truth G, the classes S_i and G_i of the i-th voxel can be defined as random variables on the label space $\{0, 1\}$. The probabistic segmentations can be represented as label probability maps: $p = \{p_i := P(S_i = 1)\}$ and $g = \{g_i := P(G_i = 1)\}$. In our case, the ground truth probability map g is such that $g_i \in \{0, 1\}, \forall i$ and the associated Soft-Dice coefficient can be written as (equation A.1):

$$SD(p, g) = \frac{2\sum_i^N p_i g_i}{\sum_i^N (p_i + g_i)} \tag{A.1}$$

where the sums run over the N voxels (or pixels) of the predicted probability 3-D (or 2-D) map p and the ground truth probability map g.

When dealing with medical images it is common that the anatomy to be segmented occupies small regions of the image (foreground regions$\ll$background region). This can cause a strong bias towards the background during the neural network training and thus the foreground regions in the resulting predicted segmentations are often under-represented or missing. To solve this strong class unbalancing, a viable solution consists in a weighted loss function in which a sample re-weighting is included, giving more importance to the foreground regions with respect to the background regions during the training of the neural network [113].
Another solution proposed by Milletari et al. [113] and used in this work consisted in the optimization of the Soft-Dice loss function based on a different formulation of the Soft-Dice coefficient. This solution removed the need to assign weights to samples to get the right class balance, leading to better experimental results than the ones obtained with the sample re-weighting approach. Thus, the Soft-Dice coefficient formulation can be modified as (equation A.2) [113]:

$$SD(p, g) = \frac{2\sum_i^N p_i g_i}{\sum_i^N (p_i^2 + g_i^2)} \tag{A.2}$$

where the sums run over the N voxels (or pixels) of the predicted probability 3-D (or 2-D) map p and the ground truth probability map g.

Then, the Soft-Dice loss function was computed as (equation A.3):

$$SD\ loss(p, g) = 1 - SD(p, g). \tag{A.3}$$

To solve the optimization problem, the Adam adaptive learning rate optimization algorithm [115] was employed. Exponential decay rates β_1 and β_2 were 0.9 and 0.999 respectively, while the learning rate ϵ was 1e-3. Lastly, a batch size of 32 (2-D approach) and 2 (3-D approach) was used.

The training process could be subdivided into 2 runs, as proposed in [116]. In the first run the neural network was trained until the validation loss (SD loss computed on 704 samples in 2-D and on 8 samples in 3-D) reaches its minimum (with a maximum number of epochs of 220). The training loss recorded at this minimum was the target threshold loss to be reached during the second run. This first run followed the early stopping technique and improved the generalization power of the neural network [117]. In the second run the training continued to include the validation set in the training set (i.e. full training set of 80 samples in 3-D and of 7040 samples in 2-D) until the validation set loss matched the threshold loss recorded during the first run (with a maximum number of epochs of 100).

The limitation of this approach in a such subdivision of the training process is that the second run could potentially never satisfy the mentioned stop criteria and the network could continue the training indefinitely. Nevertheless, in both our pipelines the validation loss reached the desired threshold within the maximum number of epochs set. The first run takes up to 320 s/epoch in the 3-D pipeline and up to 115 s/epoch in the 2-D pipeline, while the second run took a few more seconds due to the increase of the number of training samples.

A.2.4 Inference and post-processing

Once the 2-stages training was completed, the CNN was fed with unseen inputs belonging to the test set. In the 2-D approach, the neural network provided 2-D segmentations, and the output data were stacked together in order to get the 3-D predicted segmentations for each of the 20 test cardiac data (2-D to 3-D transformation). In the 3-D approach, the outputs of the neural network were the 3-D predicted segmentations for each of the 20 test cardiac data.

The 3-D segmentations obtained are then post-processed by applying a removal procedure based on the evaluation of the detected connected regions. In particular, since each predicted segmentation might contain not only the LA but also various little spurious elements, only the biggest region associated with the LA is kept.

The neural network training in both pipelines was performed thanks to

the freely available resources of the Google Colaboratory project. The deep learning framework used was Keras [118] with TensorFlow backend [119].

To compare the results to the ground truth data, the chosen evaluation metric was the Dice coefficient, an overlap-based metric. The Dice coefficient between two binary data can be written as (equation A.4)

$$D(S,G) = \frac{2\sum_i^N s_i g_i}{\sum_i^N (s_i + g_i)} \tag{A.4}$$

where the sums run over the N voxels (or pixels) of the predicted segmentation volume (or image in 2-D) S ($s_i \in S$) and the corresponding ground truth G ($g_i \in G$).

A.3 Results

In the following, the main results of the 2-D vs. 3-D comparison (evaluation metric, contours and meshes comparison) are reported.

On average, in the 2-D approach the test Dice coefficient is 0.894 and **0.896**, respectively before and after the post-processing step, while in the 3-D approach the test Dice coefficient is 0.914 and **0.914**, respectively before and after the post-processing step. The spurious regions removal step was necessary for the 90% and 80% of the test set data in the 2-D and 3-D pipelines, respectively.

In figure A.3 and A.4 the 3-D segmentations contours of the best ($D = 0.939$) and worst ($D = 0.888$) predictions at three axial levels obtained in the 3-D pipeline were reported. In addition, the 3-D segmentations contours of the best ($D = 0.932$) and worst ($D = 0.855$) predictions at three axial levels obtained in the 2-D pipeline are reported in figure A.5 and A.6. In figure A.7 and A.8 the best and worst 3-D predicted segmentations obtained in the 3-D and 2-D pipelines are reported.

A.4 Discussion

The proposed method produced a joint segmentation of the LA and PVs in AF patients exploiting a deep neural network trained end-to-end from scratch in 2-D and 3-D. Despite the high variability of the LA anatomy, the model

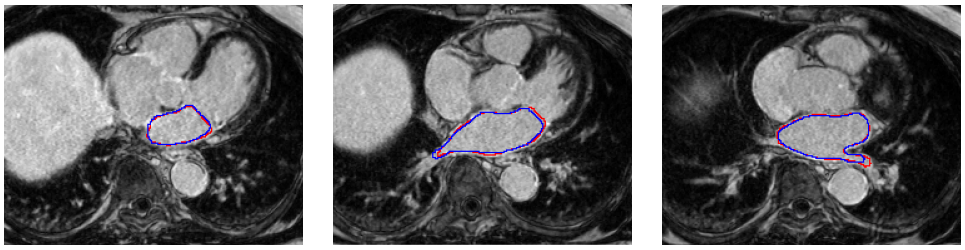

(a) (b) (c)

Figure A.3: Contours extracted from the 3-D segmentation obtained in the 3-D pipeline (red) and the ground truth (blue) of the best prediction ($D = 0.939$). These contours are extracted at 20 (a), 40 (b) and 60 (c) % of the LA extension along the longitudinal axis.

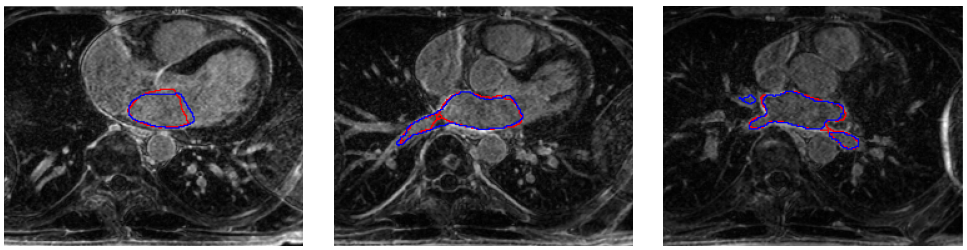

(a) (b) (c)

Figure A.4: Contours extracted from the 3-D segmentation obtained in the 3-D pipeline (red) and the ground truth (blue) of the worst prediction ($D = 0.888$). These contours are extracted at 20 (a), 40 (b) and 60 (c) % of the LA extension along the longitudinal axis.

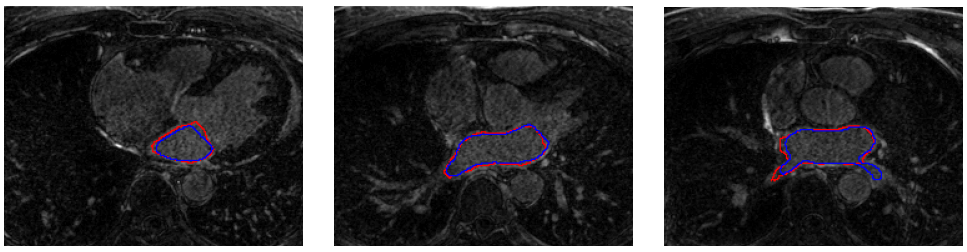

(a) (b) (c)

Figure A.5: Contours extracted from the 3-D segmentation obtained in the 2-D pipeline (red) and the ground truth (blue) of the best prediction ($D = 0.932$). These contours are extracted at 20 (a), 40 (b) and 60 (c) % of the LA extension along the longitudinal axis.

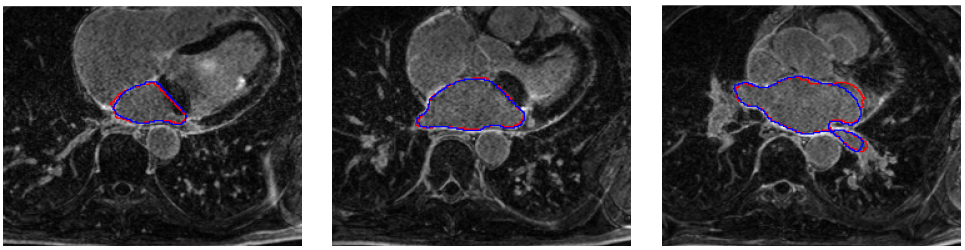

(a) (b) (c)

Figure A.6: Contours extracted from the 3-D segmentation obtained in the 2-D pipeline (red) and the ground truth (blue) of the worst prediction ($D = 0.855$). These contours are extracted at 20 (a), 40 (b) and 60 (c) % of the LA extension along the longitudinal axis.

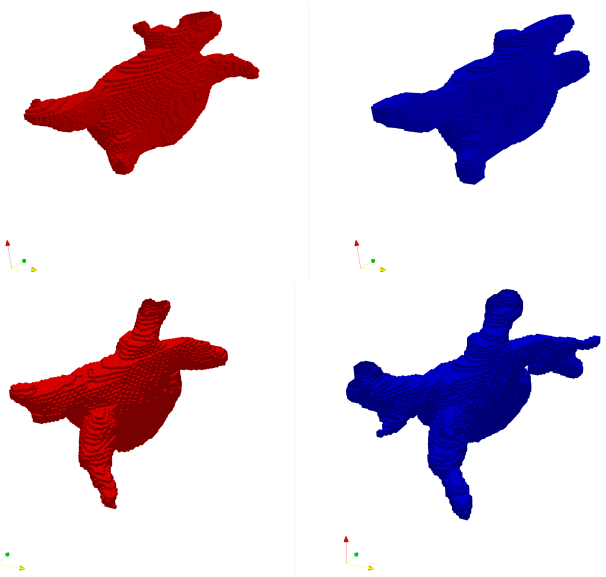

Figure A.7: 3-D meshes obtained in the 3-D pipeline with the proposed CNN (red) and the ground truth (blue) of the best prediction (up) and worst prediction (down).

provided an accurate prediction that could be useful for ablation therapy planning in both the deepened pipelines. Thanks to the fast inference time of this method, the LA surface model was obtained in few seconds (1.01 s for the 3-D pipeline and 0.02 s for the 2-D pipeline, considering only the forward propagation time of a sample through the deep neural network). Differently from other approaches in which a registration step was required [104, 108], a simple mapping of the gray level intensities would make directly available a 3-D model of a target fibrotic tissue distribution on LA surface model obtained

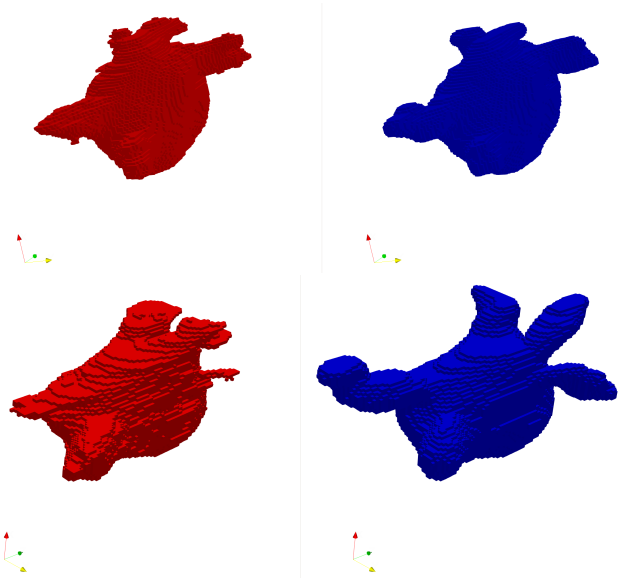

Figure A.8: 3-D meshes obtained in the 2-D pipeline with the proposed CNN (red) and the ground truth (blue) of the best prediction (top panels) and worst prediction (bottom panels).

from LGE MRI.

The high values of the Dice coefficients of the two methods designed and implemented in this work showed a good and reliable accuracy in the LA segmentation, expecially for the 3-D approach, where we obtained Dice coefficients up to 0.939. In Tao et al. [108], the best results were obtained comparing the LA chamber model obtained from LGE MRI combined with MRI angiographic data versus the models from manual tracing and authors reported a mean Dice overlap index equal to 0.86 ± 0.05 in 46 patients. Differently from the study by Tao [108] in which the performance were evaluated considering LA models with or without PVs, data used in this study were associated with ground truth segmentations in which PVs were not always included as foreground (see figure A.3(c), A.4(c), A.5(c)). This unconsistent training data labeling represented a strong bias during the training process; in addition, the performance of the proposed approach was affected by this inconsistency since final segmentations provided by the neural network may include or not PVs as foreground (see figure A.4(c), A.5(c)) differently from the corresponding ground truth. This represented an additional source of error that affected the evaluation metric. Nevertheless our results overcame the performance reported in [108]. Our results were also comparable with the ranking of the STACOM 2018 Atrial Segmentation Challenge `http://atriaseg2018.cardiacatlas.org/`) reporting an average Dice co-

efficient of 0.932 for the team in 1st place. Fourteen out of the eighteen submissions to this challenge were based on CNNs, testifying the current trend of deep learning-based medical image segmentation.

The 3-D pipeline showed better performance with respect to the 2-D pipeline, with a $D_{3-D} - D_{2-D} = 0.0186$ on average on the test set. This could be due to the 3-D convolutional layers that operated in all the dimensions exploiting the totality of the information contained in the cardiac data. Furthermore, the number of steps to obtain the final 3-D segmentation was higher in the 2-D based method pipeline due to the initial 3-D to 2-D transformation of the input images and the final 2-D to 3-D transformation of the 2-D predictions obtained. Lastly, using the 3-D convolution, the predicted test 3-D segmentations were less prone to contain spurious regions and the need of the post-processing step was reduced in the 3-D approach (from 90% to 80% of the total test set). The drawback in such a 3-D pipeline was a higher computational cost during the training process: the number of trainable parameters to be optimized was increased by 2.91 times (during the first training stage the optimization takes up to 320 s/epoch).

From the final 3-D predicted segmentations (meshes in figure A.7, A.8), it was possible to notice the difference between the two predictions: in the 2-D approach, due to the nature of the convolutional operator introduced in such architecture, the neural network outputs 2-D masks needed to be stacked together in order to obtain the 3-D segmentation. In the 3-D approach, the 3-D mask was directly computed by the model and thanks to the 3-D operator, the 3-D surface was smoother and more regular. This difference was particularly clear looking to the worst segmentations in both the pipelines (figure A.7, A.8 - down).

A.5 Conclusion

In conclusion, we have presented a complete workflow to fully automatically segment the LA cavity from LGE MRI based on a deep CNN. Trained and tested on the MICCAI STACOM 2018 Atrial Segmentation Challenge dataset, the proposed method showed highly accurate LA chamber segmentations compared to the time-consuming manual annotations. Future developments include the study and the introduction of a new custom loss function and the separation of the PVs structures from the joint segmentation of LA and PVs, evaluating the performance metric solely of the LA chamber without the PVs.

Bibliography

[1] J. Heeringa, D. A. van der Kuip, A. Hofman, J. A. Kors, G. van Herpen, B. H. C. Stricker, T. Stijnen, G. Y. Lip, and J. C. Witteman, "Prevalence, incidence and lifetime risk of atrial fibrillation: the rotterdam study," *European heart journal*, vol. 27, no. 8, pp. 949–953, 2006.

[2] S. Y. Ho, D. Sanchez-Quintana, J. A. Cabrera, and R. H. Anderson, "Anatomy of the left atrium: implications for radiofrequency ablation of atrial fibrillation.," *Journal of cardiovascular electrophysiology*, vol. 10, no. 11, pp. 1525–1533, 1999.

[3] L. Di Biase, P. Santangeli, M. Anselmino, P. Mohanty, I. Salvetti, S. Gili, R. Horton, J. E. Sanchez, R. Bai, S. Mohanty, *et al.*, "Does the left atrial appendage morphology correlate with the risk of stroke in patients with atrial fibrillation?: results from a multicenter study," *Journal of the American College of Cardiology*, vol. 60, no. 6, pp. 531–538, 2012.

[4] G. K. Moe, "On the multiple wavelet hypothesis of atrial fibrillation," *Arch Int Pharmacodyn Ther*, vol. 140, p. 183, 1962.

[5] S. S. Chugh, J. L. Blackshear, W.-K. Shen, S. C. Hammill, and B. J. Gersh, "Epidemiology and natural history of atrial fibrillation: clinical implications," *Journal of the American College of Cardiology*, vol. 37, no. 2, pp. 371–378, 2001.

[6] P. Kirchhof, S. Benussi, D. Kotecha, A. Ahlsson, D. Atar, B. Casadei, M. Castella, H.-C. Diener, H. Heidbuchel, J. Hendriks, *et al.*, "2016 esc guidelines for the management of atrial fibrillation developed in collaboration with eacts," *European journal of cardio-thoracic surgery*, vol. 50, no. 5, pp. e1–e88, 2016.

[7] A. J. Camm, P. Kirchhof, G. Y. Lip, U. Schotten, I. Savelieva, S. Ernst, I. C. Van Gelder, N. Al-Attar, G. Hindricks, B. Prendergast, *et al.*,

"Guidelines for the management of atrial fibrillation," *European Heart Journal*, p. 278, 2010.

[8] S. Colilla, A. Crow, W. Petkun, D. E. Singer, T. Simon, and X. Liu, "Estimates of current and future incidence and prevalence of atrial fibrillation in the us adult population," *The American journal of cardiology*, vol. 112, no. 8, pp. 1142–1147, 2013.

[9] M. Zoni-Berisso, F. Lercari, T. Carazza, and S. Domenicucci, "Epidemiology of atrial fibrillation: European perspective," *Clinical epidemiology*, vol. 6, p. 213, 2014.

[10] P. A. Wolf, R. D. Abbott, and W. B. Kannel, "Atrial fibrillation: a major contributor to stroke in the elderly: the framingham study," *Archives of Internal Medicine*, vol. 147, no. 9, pp. 1561–1564, 1987.

[11] P. A. Wolf, R. D. Abbott, and W. B. Kannel, "Atrial fibrillation as an independent risk factor for stroke: the framingham study.," *Stroke*, vol. 22, no. 8, pp. 983–988, 1991.

[12] J. U. Fluckiger, J. J. Goldberger, D. C. Lee, J. Ng, R. Lee, A. Goyal, and M. Markl, "Left atrial flow velocity distribution and flow coherence using four-dimensional flow mri: A pilot study investigating the impact of age and pre-and postintervention atrial fibrillation on atrial hemodynamics," *Journal of Magnetic Resonance Imaging*, vol. 38, no. 3, pp. 580–587, 2013.

[13] D. K. Gupta, A. M. Shah, R. P. Giugliano, C. T. Ruff, E. M. Antman, L. T. Grip, N. Deenadayalu, E. Hoffman, I. Patel, M. Shi, *et al.*, "Left atrial structure and function in atrial fibrillation: Engage af-timi 48," *European heart journal*, vol. 35, no. 22, pp. 1457–1465, 2014.

[14] S. Yaghi, C. Song, W. A. Gray, K. L. Furie, M. S. Elkind, and H. Kamel, "Left atrial appendage function and stroke risk," *Stroke*, vol. 46, no. 12, pp. 3554–3559, 2015.

[15] G. J. Hankey and J. W. Eikelboom, "Dabigatran etexilate: a new oral thrombin inhibitor," *Circulation*, vol. 123, no. 13, pp. 1436–1450, 2011.

[16] V. Y. Reddy, S. Möbius-Winkler, M. A. Miller, P. Neuzil, G. Schuler, J. Wiebe, P. Sick, and H. Sievert, "Left atrial appendage closure with the watchman device in patients with a contraindication for oral anticoagulation: the asap study (asa plavix feasibility study with watchman

left atrial appendage closure technology)," *Journal of the American College of Cardiology*, vol. 61, no. 25, pp. 2551–2556, 2013.

[17] C. Chnafa, S. Mendez, and F. Nicoud, "Image-based large-eddy simulation in a realistic left heart," *Computers & Fluids*, vol. 94, pp. 173–187, 2014.

[18] A. Tagliabue, L. Dedè, and A. Quarteroni, "Fluid dynamics of an idealized left ventricle: the extended nitsche's method for the treatment of heart valves as mixed time varying boundary conditions," *International Journal for Numerical Methods in Fluids*, vol. 85, no. 3, pp. 135–164, 2017.

[19] L. T. Zhang and M. Gay, "Characterizing left atrial appendage functions in sinus rhythm and atrial fibrillation using computational models," *Journal of Biomechanics*, vol. 41, no. 11, pp. 2515–2523, 2008.

[20] R. Koizumi, K. Funamoto, T. Hayase, Y. Kanke, M. Shibata, Y. Shiraishi, and T. Yambe, "Numerical analysis of hemodynamic changes in the left atrium due to atrial fibrillation," *Journal of Biomechanics*, vol. 48, no. 3, pp. 472–478, 2015.

[21] G. García-Isla, A. L. Olivares, E. Silva, M. Nuñez-Garcia, C. Butakoff, D. Sanchez-Quintana, H. G. Morales, X. Freixa, J. Noailly, T. De Potter, *et al.*, "Sensitivity analysis of geometrical parameters to study haemodynamics and thrombus formation in the left atrial appendage," *International Journal for Numerical Methods in Biomedical Engineering*, p. e3100, 2018.

[22] T. Otani, A. Al-Issa, A. Pourmorteza, E. R. McVeigh, S. Wada, and H. Ashikaga, "A computational framework for personalized blood flow analysis in the human left atrium," *Annals of Biomedical Engineering*, vol. 44, no. 11, pp. 3284–3294, 2016.

[23] W. K. Jeong, J.-H. Choi, J. P. Son, S. Lee, M. J. Lee, Y. H. Choe, and O. Y. Bang, "Volume and morphology of left atrial appendage as determinants of stroke subtype in patients with atrial fibrillation," *Heart Rhythm*, vol. 13, no. 4, pp. 820–827, 2016.

[24] S. Y. Ho, J. A. Cabrera, and D. Sanchez-Quintana, "Left atrial anatomy revisited," *Circulation: Arrhythmia and Electrophysiology*, vol. 5, no. 1, pp. 220–228, 2012.

[25] M. Haissaguerre, P. Jaïs, D. C. Shah, A. Takahashi, M. Hocini, G. Quiniou, S. Garrigue, A. Le Mouroux, P. Le Métayer, and J. Clémenty, "Spontaneous initiation of atrial fibrillation by ectopic beats originating in the pulmonary veins," *New England Journal of Medicine*, vol. 339, no. 10, pp. 659–666, 1998.

[26] E. K. Kerut, "Anatomy of the left atrial appendage," *Echocardiography*, vol. 25, no. 6, pp. 669–673, 2008.

[27] M. H. Kim, S. S. Johnston, B.-C. Chu, M. R. Dalal, and K. L. Schulman, "Estimation of total incremental health care costs in patients with atrial fibrillation in the united states," *Circulation: Cardiovascular Quality and Outcomes*, vol. 4, no. 3, pp. 313–320, 2011.

[28] N. Wiener and A. Rosenblueth, "The mathematical formulation of the problem of conduction of impulses in a network of connected excitable elements, specifically in cardiac muscle.," *Archivos del instituto de Cardiología de México*, vol. 16, no. 3, pp. 205–265, 1946.

[29] C. A. M. G. J. Klain, D. L. Jones, *et al.*, "Chronic rapld atrial pacing-structural, functional, and electrophysiological characteristics of a new mondel of sustained atrial fibrillation," *Circulation*, vol. 91, no. 5, pp. 1588–1595, 1995.

[30] K. Kamalvand, K. Tan, G. Lloyd, J. Gill, C. Bucknall, and N. Sulke, "Alterations in atrial electrophysiology associated with chronic atrial fibrillation in man," *European Heart Journal*, vol. 20, no. 12, pp. 888–895, 1999.

[31] G. Boriani, M. Biffi, R. Zannoli, A. Branzi, and B. Magnani, "Evaluation of atrial refractoriness and atrial fibrillation inducibility immediately after internal cardioversion in patients with chronic persistent atrial fibrillation," *Cardiovascular Drugs and Therapy*, vol. 13, no. 6, pp. 507–511, 1999.

[32] J. Shirani and J. Alaeddini, "Structural remodeling of the left atrial appendage in patients with chronic non-valvular atrial fibrillation: implications for thrombus formation, systemic embolism, and assessment by transesophageal echocardiography," *Cardiovascular Pathology*, vol. 9, no. 2, pp. 95–101, 2000.

[33] K. Konings, C. Kirchhof, J. Smeets, H. Wellens, O. C. Penn, and M. A. Allessie, "High-density mapping of electrically induced atrial fibrillation in humans.," *Circulation*, vol. 89, no. 4, pp. 1665–1680, 1994.

[34] M. M. Gallagher and J. Camm, "Classification of atrial fibrillation," *The American Journal of Cardiology*, vol. 82, no. 7, pp. 18N–28N, 1998.

[35] P. G. Platonov, V. Ivanov, S. Y. Ho, and L. Mitrofanova, "Left atrial posterior wall thickness in patients with and without atrial fibrillation: data from 298 consecutive autopsies," *Journal of Cardiovascular Electrophysiology*, vol. 19, no. 7, pp. 689–692, 2008.

[36] M. I. Chimowitz, M. A. DeGeorgia, R. M. Poole, A. Hepner, and W. M. Armstrong, "Left atrial spontaneous echo contrast is highly associated with previous stroke in patients with atrial fibrillation or mitral stenosis.," *Stroke*, vol. 24, no. 7, pp. 1015–1019, 1993.

[37] G. Kochiadakis, E. Skalidis, M. Kalebubas, N. Igoumenidis, S. Chrysostomakis, E. Kanoupakis, E. Simantirakis, and P. Vardas, "Effect of acute atrial fibrillation on phasic coronary blood flow pattern and flow reserve in humans," *European Heart Journal*, vol. 23, no. 9, pp. 734–741, 2002.

[38] M. Boechler, "For predicting stroke," *JAMA*, vol. 285, no. 22, 2001.

[39] J. Abecasis, R. Dourado, A. Ferreira, C. Saraiva, D. Cavaco, K. R. Santos, F. B. Morgado, P. Adragão, and A. Silva, "Left atrial volume calculated by multi-detector computed tomography may predict successful pulmonary vein isolation in catheter ablation of atrial fibrillation," *Europace*, p. eup198, 2009.

[40] A. Quarteroni, T. Lassila, S. Rossi, and R. Ruiz-Baier, "Integrated heart—coupling multiscale and multiphysics models for the simulation of the cardiac function," *Computer Methods in Applied Mechanics and Engineering*, vol. 314, pp. 345–407, 2017.

[41] C. Malossi and S. Deparis, "Lifev development guidelines," *The LifeV Project*, 2009.

[42] A. Masci, M. Alessandrini, D. Forti, F. Menghini, L. Dedé, C. Tomasi, A. Quarteroni, and C. Corsi, "A proof of concept for computational fluid dynamic analysis of the left atrium in atrial fibrillation on a patient-specific basis," *Journal of Biomechanical Engineering*, vol. 142, no. 1, 2020.

[43] M. U. Guide, "The mathworks," *Inc., Natick, MA*, vol. 5, p. 333, 1998.

[44] S. Osher and J. A. Sethian, "Fronts propagating with curvature-dependent speed: algorithms based on hamilton-jacobi formulations," *Journal of Computational Physics*, vol. 79, no. 1, pp. 12–49, 1988.

[45] P. Cignoni, M. Callieri, M. Corsini, M. Dellepiane, F. Ganovelli, and G. Ranzuglia, "Meshlab: an open-source mesh processing tool.," in *Eurographics Italian Chapter Conference*, vol. 2008, pp. 129–136, 2008.

[46] L. Antiga and D. A. Steinman, "VMTK: vascular modeling toolkit," 2012.

[47] M. Unser, "Splines: A perfect fit for signal and image processing," *IEEE Signal Processing Magazine*, vol. 16, no. 6, pp. 22–38, 1999.

[48] S. Sanatkhani and P. G. Menon, "Relating atrial appendage flow stasis risk from computational fluid dynamics to imaging based appearance paradigms for cardioembolic risk," in *Imaging for Patient-Customized Simulations and Systems for Point-of-Care Ultrasound*, pp. 86–93, Springer, 2017.

[49] C. Fletcher, *Computational techniques for fluid dynamics 2: Specific techniques for different flow categories*. Springer Science & Business Media, 2012.

[50] J. Donea, A. Huerta, J.-P. Ponthot, and A. Rodriguez-Ferran, "Encyclopedia of computational mechanics vol. 1: Fundamentals., chapter 14: Arbitrary lagrangian-eulerian methods," 2004.

[51] W. Noh, "Cel: A time-dependent, two-space-dimensional, coupled eulerian-lagrange code," tech. rep., Lawrence Radiation Lab., Univ. of California, Livermore, 1963.

[52] D. A. Wells, *Lagrangian dynamics*. McGraw-Hill Book Company, 1967.

[53] C. Hirt, A. A. Amsden, and J. Cook, "An arbitrary lagrangian-eulerian computing method for all flow speeds," *Journal of Computational Physics*, vol. 14, no. 3, pp. 227–253, 1974.

[54] P. Reymond, P. Crosetto, S. Deparis, A. Quarteroni, and N. Stergiopulos, "Physiological simulation of blood flow in the aorta: comparison of hemodynamic indices as predicted by 3-d fsi, 3-d rigid wall and 1-d models," *Medical Engineering & Physics*, vol. 35, no. 6, pp. 784–791, 2013.

[55] R. A. Khurram and A. Masud, "A multiscale/stabilized formulation of the incompressible navier–stokes equations for moving boundary flows and fluid–structure interaction," *Computational Mechanics*, vol. 38, no. 4-5, pp. 403–416, 2006.

[56] F. Nobile, "Numerical approximation of fluid-structure interaction problems with application to haemodynamics," *PhD Thesis, EPFL*, 2001.

[57] P. Le Tallec and J. Mouro, "Fluid structure interaction with large structural displacements," *Computer Methods in Applied Mechanics and Engineering*, vol. 190, no. 24, pp. 3039–3067, 2001.

[58] A. Quarteroni, *Numerical models for differential problems*, vol. 2. Springer Science & Business Media, 2010.

[59] F. E. Cellier and E. Kofman, *Continuous system simulation*. Springer Science & Business Media, 2006.

[60] D. Forti and L. Dedè, "Semi-implicit bdf time discretization of the navier–stokes equations with vms-les modeling in a high performance computing framework," *Computers & Fluids*, vol. 117, pp. 168–182, 2015.

[61] G. Scovazzi, "A discourse on galilean invariance, supg stabilization, and the variational multiscale framework," *Computer Methods in Applied Mechanics and Engineering*, vol. 196, no. 4, pp. 1108–1132, 2007.

[62] T. J. Hughes and A. Brooks, "A multidimensional upwind scheme with no crosswind diffusion," *Finite Element Methods for Convection Dominated Flows*, vol. 34, pp. 19–35, 1979.

[63] A. Stalder, M. Russe, A. Frydrychowicz, J. Bock, J. Hennig, and M. Markl, "Quantitative 2d and 3d phase contrast mri: optimized analysis of blood flow and vessel wall parameters," *Magnetic Resonance in Medicine*, vol. 60, no. 5, pp. 1218–1231, 2008.

[64] Y. Bazilevs, J. Gohean, T. Hughes, R. Moser, and Y. Zhang, "Patient-specific isogeometric fluid–structure interaction analysis of thoracic aortic blood flow due to implantation of the jarvik 2000 left ventricular assist device," *Computer Methods in Applied Mechanics and Engineering*, vol. 198, no. 45, pp. 3534–3550, 2009.

[65] L. Dedè, F. Menghini, and A. Quarteroni, "Computational fluid dynamics of blood flow in an idealized left human heart," *International journal for numerical methods in biomedical engineering*, p. e3287, 2019.

[66] J. Roelandt and M. Pozzoli, "On-invasive assessment of left ventricular diastolic (dys) function and filling pressure," *Heart Views*, vol. 2, no. 3, pp. 6–6, 2001.

[67] P. Langley, J. Bourke, and A. Murray, "Frequency analysis of atrial fibrillation," in *Computers in Cardiology 2000. Vol. 27 (Cat. 00CH37163)*, pp. 65–68, IEEE, 2000.

[68] A. Masci, L. Barone, L. Dedè, M. Fedele, C. Tomasi, A. Quarteroni, and C. Corsi, "The impact of left atrium appendage morphology on stroke risk assessment in atrial fibrillation: a computational fluid dynamics study," *Frontiers in Physiology*, vol. 9, p. 1938, 2019.

[69] V. Y. Reddy, H. Sievert, J. Halperin, S. K. Doshi, M. Buchbinder, P. Neuzil, K. Huber, B. Whisenant, S. Kar, V. Swarup, *et al.*, "Percutaneous left atrial appendage closure vs warfarin for atrial fibrillation: a randomized clinical trial," *Jama*, vol. 312, no. 19, pp. 1988–1998, 2014.

[70] M. Markl, D. C. Lee, J. Ng, M. Carr, J. Carr, and J. J. Goldberger, "Left atrial 4d flow mri: Stasis and velocity mapping in patients with atrial fibrillation," *Investigative Radiology*, vol. 51, no. 3, p. 147, 2016.

[71] A. Masci, M. Alessandrini, D. Forti, F. Menghini, L. Dedé, C. Tommasi, A. Quarteroni, and C. Corsi, "A patient-specific computational fluid dynamics model of the left atrium in atrial fibrillation: Development and initial evaluation," in *International Conference on Functional Imaging and Modeling of the Heart*, pp. 392–400, Springer, 2017.

[72] M. Valinoti, C. Fabbri, D. Turco, R. Mantovan, A. Pasini, and C. Corsi, "3d patient-specific models for left atrium characterization to support ablation in atrial fibrillation patients," *Magnetic Resonance Imaging*, vol. 45, pp. 51–57, 2018.

[73] Q. Fang and D. Boas, "iso2mesh: a 3d surface and volumetric mesh generator for matlab/octave," 2010.

[74] L. Shapira, A. Shamir, and D. Cohen-Or, "Consistent mesh partitioning and skeletonisation using the shape diameter function," *The Visual Computer*, vol. 24, no. 4, p. 249, 2008.

[75] A. Fabri and M. Teillaud, "Cgal-the computational geometry algorithms library," in *10e Colloque National en Calcul des Structures*, p. 6, 2011.

[76] P. J. Besl and N. D. McKay, "Method for registration of 3-d shapes," in *Sensor Fusion IV: Control Paradigms and Data Structures*, vol. 1611, pp. 586–607, International Society for Optics and Photonics, 1992.

[77] M. Piccinelli, A. Veneziani, D. A. Steinman, A. Remuzzi, and L. Antiga, "A framework for geometric analysis of vascular structures: application to cerebral aneurysms," *IEEE Transactions on Medical Imaging*, vol. 28, no. 8, pp. 1141–1155, 2009.

[78] S. Gautam and R. M. John, "Interatrial electrical dissociation after catheter-based ablation for atrial fibrillation and flutter," *Circulation: Arrhythmia and Electrophysiology*, vol. 4, no. 4, pp. e26–e28, 2011.

[79] R. Beigel, N. C. Wunderlich, S. Y. Ho, R. Arsanjani, and R. J. Siegel, "The left atrial appendage: anatomy, function, and noninvasive evaluation," *JACC: Cardiovascular Imaging*, vol. 7, no. 12, pp. 1251–1265, 2014.

[80] A. L. Olivares, E. Silva, M. Nuñez-Garcia, C. Butakoff, D. Sánchez-Quintana, X. Freixa, J. Noailly, T. de Potter, and O. Camara, "In silico analysis of haemodynamics in patient-specific left atria with different appendage morphologies," in *International Conference on Functional Imaging and Modeling of the Heart*, pp. 412–420, Springer, 2017.

[81] T. Otani, A. Al-Issa, A. Pourmorteza, E. R. McVeigh, S. Wada, and H. Ashikaga, "A computational framework for personalized blood flow analysis in the human left atrium," *Annals of Biomedical Engineering*, vol. 44, no. 11, pp. 3284–3294, 2016.

[82] G. M. Bosi, A. Cook, R. Rai, L. J. Menezes, S. Schievano, R. Torii, and G. B. Burriesci, "Computational fluid dynamic analysis of the left atrial appendage to predict thrombosis risk," *Frontiers in Cardiovascular Medicine*, vol. 5, p. 34, 2018.

[83] P. Osmancik, P. Tousek, D. Herman, P. Neuzil, P. Hala, J. Stasek, L. Haman, P. Kala, M. Poloczek, M. Branny, *et al.*, "Interventional left atrial appendage closure vs novel anticoagulation agents in patients with atrial fibrillation indicated for long-term anticoagulation (prague-17 study)," *American Heart Journal*, vol. 183, pp. 108–114, 2017.

[84] D. R. Holmes, S. Kar, M. J. Price, B. Whisenant, H. Sievert, S. K. Doshi, K. Huber, and V. Y. Reddy, "Prospective randomized evaluation of the watchman left atrial appendage closure device in patients with atrial fibrillation versus long-term warfarin therapy: the prevail trial," *Journal of the American College of Cardiology*, vol. 64, no. 1, pp. 1–12, 2014.

[85] R. B. Fountain, D. Holmes, K. Chandrasekaran, D. L. Packer, S. J. Asirvatham, R. Van Tassel, and Z. Turi, "The protect af (watchman left atrial appendage system for embolic protection in patients with atrial fibrillation) trial," *American Heart Journal*, vol. 151, no. 5, pp. 956–961, 2006.

[86] L. V. Boersma, B. Schmidt, T. R. Betts, H. Sievert, C. Tamburino, E. Teiger, E. Pokushalov, S. Kische, T. Schmitz, K. M. Stein, *et al.*, "Implant success and safety of left atrial appendage closure with the watchman device: peri-procedural outcomes from the ewolution registry," *European Heart Journal*, vol. 37, no. 31, pp. 2465–2474, 2016.

[87] A. Aryana and A. d'Avila, "Incomplete closure of the left atrial appendage: implication and management," *Current Cardiology Reports*, vol. 18, no. 9, p. 82, 2016.

[88] N. S. Bajaj, A. Parashar, S. Agarwal, N. Sodhi, K. L. Poddar, A. Garg, E. M. Tuzcu, and S. R. Kapadia, "Percutaneous left atrial appendage occlusion for stroke prophylaxis in nonvalvular atrial fibrillation: a systematic review and analysis of observational studies," *JACC: Cardiovascular Interventions*, vol. 7, no. 3, pp. 296–304, 2014.

[89] A. O. Badheka, A. Chothani, K. Mehta, N. J. Patel, A. Deshmukh, M. Hoosien, N. Shah, V. Singh, P. Grover, G. T. Savani, *et al.*, "Utilization and adverse outcomes of percutaneous left atrial appendage closure for stroke prevention in atrial fibrillation in the united states: influence of hospital volume," *Circulation: Arrhythmia and Electrophysiology*, vol. 8, no. 1, pp. 42–48, 2015.

[90] A. M. Aguado, A. L. Olivares, C. Yagüe, E. Silva, M. Nuñez-García, Á. Fernandez-Quilez, J. Mill, I. Genua, D. Arzamendi, T. De Potter, *et al.*, "In silico optimization of left atrial appendage occluder implantation using interactive and modeling tools," *Frontiers in Physiology*, vol. 10, p. 237, 2019.

[91] D. Jia, B. Jeon, H.-B. Park, H.-J. Chang, and L. T. Zhang, "Image-based flow simulations of pre-and post-left atrial appendage closure in the left atrium," *Cardiovascular Engineering and Technology*, vol. 10, no. 2, pp. 225–241, 2019.

[92] C. P. Appleton, "Hemodynamic determinants of doppler pulmonary venous flow velocity components: new insights from studies in lightly sedated normal dogs," *Journal of the American College of Cardiology*, vol. 30, no. 6, pp. 1562–1574, 1997.

[93] A. Tagliabue, L. Dede, and A. Quarteroni, "Fluid dynamics of an idealized left ventricle: the extended nitsche's method for the treatment of heart valves as mixed time varying boundary conditions," *Mathicse Report*, vol. 31, 2015.

[94] E. Anter, M. Jessup, and D. J. Callans, "Atrial fibrillation and heart failure," *Circulation*, vol. 119, no. 18, pp. 2516–2525, 2009.

[95] F. Ouyang, R. Tilz, J. Chun, B. Schmidt, E. Wissner, T. Zerm, K. Neven, B. Köktürk, M. Konstantinidou, A. Metzner, *et al.*, "Long-term results of catheter ablation in paroxysmal atrial fibrillationclinical perspective: Lessons from a 5-year follow-up," *Circulation*, vol. 122, no. 23, pp. 2368–2377, 2010.

[96] R. Weerasooriya, P. Khairy, J. Litalien, L. Macle, M. Hocini, F. Sacher, N. Lellouche, S. Knecht, M. Wright, I. Nault, *et al.*, "Catheter ablation for atrial fibrillation: are results maintained at 5 years of follow-up?," *Journal of the American College of Cardiology*, vol. 57, no. 2, pp. 160–166, 2011.

[97] L. Malcolme-Lawes, C. Juli, R. Karim, W. Bai, R. Quest, P. Lim, S. Jamil-Copley, P. Kojodjojo, B. Ariff, D. Davies, *et al.*, "Automated analysis of atrial late gadolinium enhancement imaging that correlates with endocardial voltage and clinical outcomes: a 2-center study," *Heart Rhythm*, vol. 10, no. 8, pp. 1184–1191, 2013.

[98] N. F. Marrouche, D. Wilber, G. Hindricks, P. Jais, N. Akoum, F. Marchlinski, E. Kholmovski, N. Burgon, N. Hu, L. Mont, *et al.*, "Association of atrial tissue fibrosis identified by delayed enhancement mri and atrial fibrillation catheter ablation: the decaaf study," *Journal of the American Medical Association*, vol. 311, no. 5, pp. 498–506, 2014.

[99] T. Zghaib and S. Nazarian, "New insights into the use of cardiac magnetic resonance imaging to guide decision-making in af management," *Canadian Journal of Cardiology*, 2018.

[100] A. Giannakidis, E. Nyktari, J. Keegan, I. Pierce, I. S. Horduna, S. Haldar, D. J. Pennell, R. Mohiaddin, T. Wong, and D. N. Firmin, "Rapid automatic segmentation of abnormal tissue in late gadolinium enhancement cardiovascular magnetic resonance images for improved management of long-standing persistent atrial fibrillation," *Biomedical Engineering Online*, vol. 14, no. 1, p. 88, 2015.

[101] D. D. Spragg, I. Khurram, S. L. Zimmerman, H. Yarmohammadi, B. Barcelon, M. Needleman, D. Edwards, J. E. Marine, H. Calkins, and S. Nazarian, "Initial experience with magnetic resonance imaging of atrial scar and co-registration with electroanatomic voltage mapping during atrial fibrillation: success and limitations," *Heart Rhythm*, vol. 9, no. 12, pp. 2003–2009, 2012.

[102] C. Sohns, R. Karim, J. Harrison, A. Arujuna, N. Linton, R. Sennett, H. Lambert, G. Leo, S. Williams, R. Razavi, *et al.*, "Quantitative magnetic resonance imaging analysis of the relationship between contact force and left atrial scar formation after catheter ablation of atrial fibrillation," *Journal of Cardiovascular Electrophysiology*, vol. 25, no. 2, pp. 138–145, 2014.

[103] R. Karim, R. J. Housden, M. Balasubramaniam, Z. Chen, D. Perry, A. Uddin, Y. Al-Beyatti, E. Palkhi, P. Acheampong, S. Obom, *et al.*, "Evaluation of current algorithms for segmentation of scar tissue from late gadolinium enhancement cardiovascular magnetic resonance of the left atrium: an open-access grand challenge," *Journal of Cardiovascular Magnetic Resonance*, vol. 15, no. 1, p. 105, 2013.

[104] M. Valinoti, C. Fabbri, D. Turco, R. Mantovan, A. Pasini, and C. Corsi, "3d patient-specific models for left atrium characterization to support ablation in atrial fibrillation patients," *Magnetic Resonance Imaging*, vol. 45, pp. 51–57, 2018.

[105] G. Yang, X. Zhuang, H. Khan, S. Haldar, E. Nyktari, L. Li, R. Wage, X. Ye, G. Slabaugh, R. Mohiaddin, *et al.*, "Fully automatic segmentation and objective assessment of atrial scars for long-standing persistent atrial fibrillation patients using late gadolinium-enhanced mri," *Medical physics*, vol. 45, no. 4, pp. 1562–1576, 2018.

[106] A. Mortazi, R. Karim, K. S. Rhode, J. Burt, and U. Bagci, "Cardiacnet: Segmentation of left atrium and proximal pulmonary veins from MRI using multi-view CNN," *CoRR*, vol. abs/1705.06333, 2017.

[107] C. Tobon-Gomez, A. J. Geers, J. Peters, J. Weese, K. Pinto, R. Karim, M. Ammar, A. Daoudi, J. Margeta, Z. Sandoval, B. Stender, Y. Zheng, M. A. Zuluaga, J. Betancur, N. Ayache, M. A. Chikh, J. L. Dillenseger, B. M. Kelm, S. Mahmoudi, S. Ourselin, A. Schlaefer, T. Schaeffter, R. Razavi, and K. S. Rhode, "Benchmark for algorithms segmenting the left atrium from 3d ct and mri datasets," *IEEE Transactions on Medical Imaging*, vol. 34, pp. 1460–1473, July 2015.

[108] Q. Tao, E. G. Ipek, R. Shahzad, F. F. Berendsen, S. Nazarian, and R. J. van der Geest, "Fully automatic segmentation of left atrium and pulmonary veins in late gadolinium-enhanced mri: Towards objective atrial scar assessment," *Journal of Magnetic Resonance Imaging*, vol. 44, no. 2, pp. 346–354, 2016.

[109] O. Ronneberger, P. Fischer, and T. Brox, "U-net: Convolutional networks for biomedical image segmentation," *CoRR*, vol. abs/1505.04597, 2015.

[110] K. He, X. Zhang, S. Ren, and J. Sun, "Delving deep into rectifiers: Surpassing human-level performance on imagenet classification," *CoRR*, vol. abs/1502.01852, 2015.

[111] S. Ioffe and C. Szegedy, "Batch normalization: Accelerating deep network training by reducing internal covariate shift," *CoRR*, vol. abs/1502.03167, 2015.

[112] N. Srivastava, G. Hinton, A. Krizhevsky, I. Sutskever, and R. Salakhutdinov, "Dropout: A simple way to prevent neural networks from overfitting," *Journal of Machine Learning Research*, vol. 15, pp. 1929–1958, Jan. 2014.

[113] F. Milletari, N. Navab, and S. Ahmadi, "V-net: Fully convolutional neural networks for volumetric medical image segmentation," in *2016 Fourth International Conference on 3D Vision (3DV)*, pp. 565–571, Oct 2016.

[114] L. Fidon, W. Li, L. C. García-Peraza-Herrera, J. Ekanayake, N. Kitchen, S. Ourselin, and T. Vercauteren, "Generalised wasserstein dice score for imbalanced multi-class segmentation using holistic convolutional networks," in *Brainlesion: Glioma, Multiple Sclerosis, Stroke*

and Traumatic Brain Injuries - Third International Workshop, BrainLes 2017, Held in Conjunction with MICCAI 2017, Quebec City, QC, Canada, September 14, 2017, Revised Selected Papers, pp. 64–76, 2017.

[115] D. P. Kingma and J. Ba, "Adam: A method for stochastic optimization," *CoRR*, vol. abs/1412.6980, 2014.

[116] G. E. Hinton, N. Srivastava, A. Krizhevsky, I. Sutskever, and R. Salakhutdinov, "Improving neural networks by preventing co-adaptation of feature detectors," *CoRR*, vol. abs/1207.0580, 2012.

[117] I. Goodfellow, Y. Bengio, and A. Courville, *Deep Learning*. MIT Press, 2016. `http://www.deeplearningbook.org`.

[118] F. Chollet *et al.*, "Keras." `https://github.com/keras-team/keras`, 2015.

[119] M. Abadi, A. Agarwal, *et al.*, "TensorFlow: Large-scale machine learning on heterogeneous systems," 2015. Software available from tensorflow.org.

Acknowledgements

Per concludere questo lavoro di Tesi, ringrazio tanto la Prof.ssa Corsi per avermi dato la possibilità di sviluppare questo progetto di Dottorato e per avermi supportato e soprattutto sopportato con tanta pazienza, incoraggiandomi anche nei momenti di maggiore difficoltà con i Suoi preziosi consigli.
Inoltre, desidero ringraziare il Prof. Severi per i Suoi consigli e suggerimenti.
Ringrazio il Dott. Tomasi per avere partecipato attivamente al progetto di Dottorato e in particolare per il progetto FATA.
Ringrazio fortemente i miei genitori; è grazie ai loro insegnamenti e la loro saggezza se sono riuscito ad arrivare a questo importante traguardo della mia vita. Il loro grande sostegno e affetto è stato fondamentale nel superare ogni ostacolo, per raggiungere gli obiettivi prefissati. Ringrazio Francesco per essermi sempre stato vicino durante questi tre anni.
Uno speciale ringraziamento va ad Alessia che mi ha sempre accompagnato durante questo percorso di studio, incoraggiandomi e spronandomi soprattutto nei periodi difficili.
Un ringraziamento va ai miei amici Nicola, Luca, Paolo, Gianluca, Simone, Tiziano e Michael per i momenti di divertimento passati insieme e per la loro vicinanza durante i periodi più stressanti e meno felici. Ci tengo a ringraziare anche i miei colleghi dell'azienda dove lavoro per avermi sempre supportato.
Un ulteriore ringraziamento va anche a tutti i parenti e amici che hanno condiviso con me ogni momento di questo percorso.
Infine, ringrazio anche me stesso per avere dimostrato forza e capacità di non mollare mai, nonostante le difficoltà rilevanti, nel portare a termine questo percorso importante della mia vita.